6-9-2016

Top-down Cross-Section Controlled III-Nitride Nanowire Lasers

Changyi Li

Changyi Li

Candidate

Optical Science and Engineering - ECE

Department

This dissertation is approved, and it is acceptable in quality and form for publication:

Approved by the Dissertation Committee:

Steven R. J. Brueck , Chairperson

George T. Wang

Daniel F. Feezell

Ganesh Balakrishnan

Ralph L. Dawson

TOP-DOWN CROSS-SECTION CONTROLLED III-NITRIDE NANOWIRE LASERS

by

CHANGYI LI

B.S., Optical Information Science and Technology, 2008
M.E., Optoelectronics Information Engineering, 2011
M.S. Optical Science and Engineering, 2013

DISSERTATION

Submitted in Partial Fulfillment of the
Requirements for the Degree of

Doctor of Philosophy
Optical Science and Engineering

The University of New Mexico
Albuquerque, New Mexico

May, 2016

Dedication

This work is dedicated to my lovely wife, Jielin Pan, and my naughty son, Albert Li. It is also dedicated to my parents: Qingxi Li, Guiying Liu, Xiuling Pan, and Ying Tang. I also dedicate this dissertation to Susan Stinnett, Regan Stinnett, Priscilla Duncan, and James Duncan.

ACKNOWLEDGEMENTS

My deepest gratitude is to my advisors: Dr. Steven R. J. Brueck, and Dr. George T. Wang. Dr. Brueck always gave me answers or advice whenever I had theoretical or technical questions. Dr. Wang guided me to the right direction during my research. More importantly, they are examples of extraordinary researchers. They are not only advisors but also a friend and an older brother to me. I deeply appreciate their encouragement and help in my study and my life.

Furthermore, I would like to thank Dr. Feezell, Dr. Balakrishnan, and Dr. Dawson for serving on my committee. Their fruitful discussions and advice are of great help for my Ph.D. research.

Moreover, I would like to thank my group members and collaborators: Dr. Sheng Liu, Dr. Jeremy Wright, Dr. Huiwen Xu, Dr. Benjamin Leung, Dr. Miao-Cian Tsai, Dr. Tzu-Ming Lu, and Mr. Jeffery Figiel for their fruitful discussion and help on my research.

I would also like to thank my friends: Dr. Xiang He and Yang Deng for their friendship and support.

Last but not least, I would like to thank my family: Jielin Pan, Albert Li, Qingxi Li, Guiying Liu, Xiuling Pan, and Ying Tang for supporting and encouraging me through the ups and downs. I would like to thank my American parents: Susan Stinnett, Dr. Regan Stinnett, Priscilla Duncan, and James Duncan. They gave me the parental love and care in the United States.

Top-down Cross-Section Controlled III-Nitride Nanowire Lasers

By

Changyi Li

B.S., Optical information Science and Technology, Huazhong University of Science and Technology, China, 2008

M.E., Optoelectronics Information Engineering, Huazhong University of Science and Technology, China, 2011

M.S., Optical Science and Engineering, University of New Mexico, USA, 2013

Ph.D., Optical Science and Engineering, University of New Mexico, USA, 2016

Abstract

III-nitride nanowire lasers have drawn significant attention as potential compact coherent light sources for a wide range of applications such as on-chip communication, optical sensing, and solid-state lighting. For practical applications, control over the lasing properties is needed. For example, a single mode lasing is beneficial for reducing the pulse broadening and the signal errors during the optical communications. An annular-

shaped beam could be potentially used for the atom trapping or the stimulated emission depletion spectroscopy. The polarization-sensitive on-chip optical components also require linear polarization. However, due to the compact size of nanowire lasers and the cross-sectional symmetry of the traditional nanowire lasers, controlling the lasing properties still remains challenging.

A top-down two-step etch process developed for vertical GaN nanowires offers the ability to precisely control the cross-section of the nanowire lasers. Consequently, the lasing properties can potentially be tailored by controlling the cross-section. In this dissertation, annular-shaped emission was demonstrated from GaN nanotube lasers with optical pumping at room temperature, consistent with finite-difference time-domain simulation results.

Linearly polarized lasing emission was also realized from rectangular cross-sectioned GaN nanowire lasers. When the shorter y-dimension is ~120 nm, the rectangular cross-section creates a large contrast of the effective index of refraction, resulting in higher transverse confinement factors for the y-polarized modes than for the x-polarized modes.

In order to pursue electrically injected single III-nitride nanowire lasers, non-polar InGaN/GaN multi-quantum-wells core-shell nanowires were fabricated by a combination of the top-down two-step etch process and a regrowth process. Lasing was observed from the core-shell nanowires by optical pumping at room temperature. A Hakki-Paoli measurement shows high modal gains of the non-polar core-shell nanowire lasers and the non-uniform gains resulting from the inhomogeneous regrowth.

As a step towards electrical pumping, a Ti “ohmic like” contact to the n-GaN core was fabricated. However, because of the lack of the ohmic contact to the p-GaN shell, the injection efficiency was extremely limited. As a result, instead of electrically-driven lasing, only weak spontaneous emission was observed in the electroluminescence measurement.

Contents

List of Figures

List of Tables

Chapter 1

Introduction

1.1 GaN-based III-nitride semiconductor materials

1.1.1 Introduction of GaN and III-nitride semiconductors

Group III-nitride semiconductors are InN, GaN, AlN and their binary and ternary alloys. Since the first single-crystalline GaN film was grown in 1969 by Maruska and Tietjen using vapor-phase growth technique[1], tremendous research has been focused on GaN and III-nitride semiconductors[2]–[5]. In 2014, the Nobel Prize in physics was awarded to Dr. Akasaki, Dr. Amano, and Dr. Nakamura for their breakthrough contributions in GaN-based III-nitride blue light emitting diode.

GaN is a wide bandgap binary semiconductor[6]. The most common structure of single-crystalline GaN is the wurtzite structure shown in Figure 1.1(a). The *c*-plane [0001] is composed of hexagonally arranged atoms. Alternating layers of Ga and N atoms are arranged along the *c*-direction [0001]. Since the bonds between Ga and N atoms are partially ionic[7], the electron cloud locates closer to the N atoms, leading to negatively charged N atoms and positively charged Ga atoms. This phenomenon results in a spontaneous polarization electric field along the *c*-direction[8]. The *c*-direction is under the largest spontaneous polarization electric field and is referred to as the "polar" orientation. The crystallographic orientations perpendicular to the c-orientation lack the spontaneous polarization electric field. Thus, these orientations are referred as "non-

polar" orientations. The crystallographic orientations in between the polar and non-polar orientations are referred to as the semi-polar orientations. The spontaneous polarization electric field plays a significant role for III-nitride light-emitting devices with quantum wells. For quantum wells grown on the polar *c*-plane, the built-in electric field tilts the band structure of the quantum wells, leading to the separation of the electron and hole wavefunctions, therefore reducing the overlap of the electrons and holes. This effect is known as the quantum confined Stark effect (QCSE) [9], [10]. It has been demonstrated that QCSE reduces the internal quantum efficiency of a light-emitting diode and causes a blue-shift of the emission wavelength as the injected current increases[11].

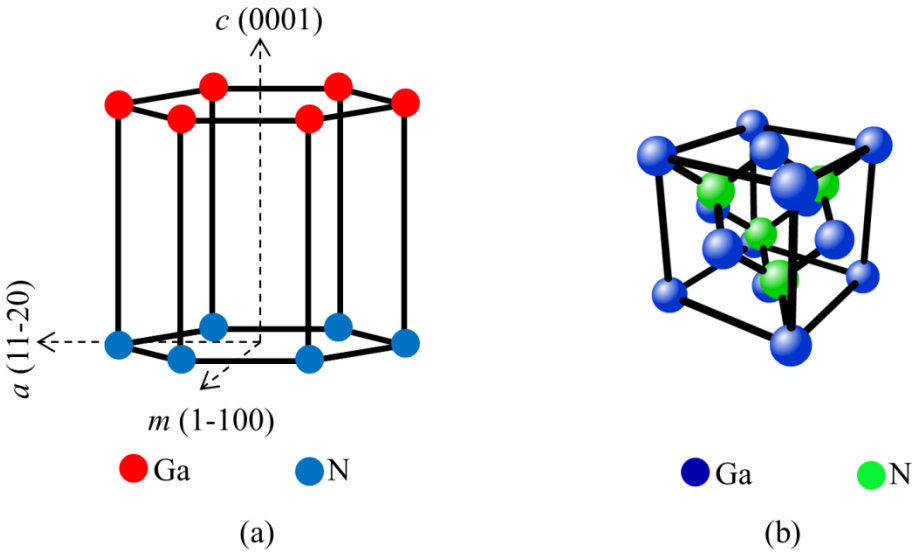

Figure 1.1 The crystal structure of (a) wurtzite GaN and (b) cubic GaN. The dashed arrows in (a) indicate the polar c-direction and the nonpolar m-direction and a-direction.

Besides wurtzite GaN, the cubic-phase GaN with a zinc-blende structure (Figure 1.1(b)) has also been demonstrated by many groups[12]–[16]. Because the cubic crystals have

higher crystallographic symmetry than the wurtzite structure, the cubic GaN is expected to have lower phonon scattering and different bandgap and impurity, compared to the wurtzite GaN. However, since the cubic-phase GaN is not the lowest energy phase, the thermodynamic instability of cubic-phase GaN is one of the bottlenecks of growing high quality cubic-phase GaN.

1.1.2 Advantages of GaN and III-nitride semiconductors

The III-nitride semiconductors have many advantageous properties. III-nitride semiconductors are direct bandgap materials, and their bandgaps can in theory be continuously tuned from the deep ultraviolet (6.2eV (~200 nm) for AlN) to near infrared (0.65eV (~1.9 μm) for InN) wavelengths. The wide spectral coverage makes III-nitride promising materials for applications such as visible-blind UV photodetectors[17], solar cells[18], [19], and water purification[20], [21]. More importantly, because of the direct bandgap, III-nitride materials have been widely utilized to fabricate UV to green light-emitting diodes and lasers[5], [6], [9].

Despite the higher dislocation density (on the order of $10^8 \sim 10^{10}\ cm^{-3}$) of III-nitride based LEDs compared to III-arsenide and III-phosphide based LEDs, III-nitride LEDs are still able to achieve high quantum efficiency[22]. To explain the phenomenon, Chichibu et al. observed In-rich regions with a 3 nm size from the cross-sectional transmission electron microscopy (TEM) images[23]. The In-rich regions result from the In composition fluctuation during the growth process and provide "quantum dot like" localized potential minima. The electroluminescence (EL) peak emission energy was measured to be 100~570 meV lower than the free exciton energy of GaN, also

confirming that the spontaneous recombination comes from the localized potential minima. It is believed that the injected carriers are captured by the localized potential minima before capture by defect-related non-radiative recombination centers, leading to a low non-radiative recombination rate.

In contrast to the lower energy gap GaAs-based or InP-based quantum structures, higher exciton bonding energies of InGaN/AlGaN quantum wells (~30 meV)[24], quantum wires (~10-37 meV), and quantum dots (~20-80 meV) were calculated theoretically[25], due to the wide bandgap. The higher exciton bonding energy results in a smaller exciton radius and a higher exciton density. As a result, the exciton transitions dominate over the free electron-hole transitions. The dominant exciton transitions further give rise to higher optical gain. Thus, low threshold current densities of 88 A/cm^2 and 623 A/cm^2 were calculated, corresponding to a 50Å×50Å×50Å defect-free quantum dot and a 50Å×50Å×50Å quantum dot with a dislocation density of $1 \times 10^{10}\ cm^{-2}$, respectively.

High oscillator strength of InGaN quantum well excitons was measured as $2 \times 10^{13}\ cm^{-2}$ per quantum well, which is 1 order of magnitude higher than the reported oscillator strength of GaAs quantum wells[26]. The high oscillator strength offers a strong exciton-photon coupling. Therefore, Bose-Einstein condensation (BEC) of polaritons can potentially be achieved at room temperature in GaN microcavities, opening the route of demonstrating ultralow threshold lasing or thresholdless lasing in GaN microcavities and nanocavities.

GaN also has a high chemical and thermal stability[27]. Therefore, GaN devices can be used in harsh environments. The high thermal conductivity[28] and the high breakdown field also make GaN a promising material for high-power electronics devices.

Since the first InGaN-based multi-quantum-well laser diode was demonstrated in 1996[29], the performance of III-nitride laser diodes has been improved significantly. Because of the short wavelength and long lifetime, III-nitride violet laser diodes (405 nm) have been commercialized for high-density optical data storage (blue-ray). The state-of-the-art III-nitride violet laser diodes have achieved an output power of 500 mW[30] and 8 W[31] for single and multiple transverse mode devices, respectively. Besides, III-nitride blue (440–460 nm) and green (515–535 nm) laser diodes are considered as candidates for solid-state lighting [32], large televisions, high-power projectors and portable projectors, because of their lack of efficiency droop in the "green gap", high directional high power output, potentially higher wall-plug efficiency and longer lifetime. The output power of blue *c*-plane laser diodes has reached 120 mW for single-mode lasing and 1.17 W for multi-mode lasing[33]. An output power of 50 mW was also demonstrated for green laser diodes[34].

1.2 Advantages of III-nitride nanowires and nanowire lasers

Nanowires are quasi-one-dimensional nanomaterials. The diameters of nanowires typically are from tens of nanometers to hundreds of nanometers, and typical lengths are from a few microns to hundreds of microns. Compared to the traditional III-V materials system, there is a large variation of the lattice constant of III-nitride materials. Therefore, the performance of conventional planar III-nitride devices is largely limited due to the

high defect density and the strain at the interface of the hetero-structures, or between the epi-layer and the substrate, resulting from the large lattice mismatch. In contrast, nanowires grown perpendicularly from the substrate have small cross-sections, and thus, an efficient lateral strain relaxation. The efficient strain relaxation allows not only for growing near dislocation-free homogenous nanowires[35], but also growing thicker heterojunctions with larger lattice mismatch on nanowires[36]. Because of the freedom of designing and fabricating nanowires free from strain and thermal expansion, nanowires are considered as the promising candidate for a number of applications including electronics[37], solid-state lighting[38], photovoltaics[19], and bio-sensing[39].

Among the above applications, nanowire lasers have drawn increasing attention in the past decade[40], [41]. Due to their small dimensions, nanowire lasers can potentially be used as compact-size coherent light sources compatible with the photonic vary large scale integration (VLSI) circuits[42]. The reduced size of nanowire lasers also offers potentially low power requirement, low lasing threshold, and high modulation speed.

1.3 Challenges of III-nitride nanowire lasers

Although III-nitride nanowire lasers have shown potential as the coherence light source for the future nanoscale on-chip applications or solid-state lighting, the lack of controlling the following lasing properties limits the utilization of III-nitride nanowire lasers for practical applications.

High beam quality and spectral purity is required for many applications such as optical communication, optical storage, and optical sensing. First of all, because of the group

velocity dispersion in an on-chip optical waveguide, multi-wavelength lasing leads to temporal pulse broadening and false signaling. Second, some on-chip optical components are wavelength sensitive. The output of a Mach-Zehnder interferometer is a function of the wavelength. Therefore, the extinction ratio and the signal-noise ratio would be significantly reduced if a multi-wavelength lasing is sent to the interferometer. Third, the coupling efficiency between a nanowire laser and a waveguide depends largely on the transverse mode profile of the laser source. As a result, a single transverse mode nanowire laser would simplify the design of the laser-waveguide coupling.

In addition, the ability to control and tune the lasing wavelength would enable the use of nanowire lasers in many wavelength-sensitive applications, such as saturated spectroscopy, environmental monitoring, and optical communication.

Polarization control is also beneficial for the polarization-sensitive applications, such as optical communication, nonlinear optics, and compact laser-based displays.

Besides, a shape-controlled lasing beam of III-nitride nanowire lasers could potentially be used for applications such as atom trapping or stimulated emission depletion spectroscopy.

However, due to the compact size and the symmetric geometry of nanowire lasers, achieving single-mode lasing from single nanowire lasers has been challenging. In order to solve this problem, a novel cross-section control technique is explored in this dissertation to achieve an intrinsic control of the beam shape and the polarization.

Another challenge of the III-nitride nanowire lasers is the electrically injected single nanowire laser. Despite the fact that electrically driven single CdS nanowire lasers and AlGaN nanowire array lasers have been demonstrated, the electrically injected single III-nitride nanowire laser has not been realized, because of the difficulty of fabricating ohmic contact to p-GaN and the propagation loss from the metal contact. In this dissertation, optically pumped non-polar InGaN/GaN multi-quantum-well core-shell nanowire lasers are demonstrated, showing a significantly improved optical gain. The electroluminescence (EL) and the effect of the metal contact on the lasing threshold of single InGaN/GaN core-shell nanowires were also studied, opening the route to the electrically driven single III-nitride nanowire lasers.

The state of the field is outlined in Section 1.4 and 1.5 for a comprehensive understanding.

1.4 A review of various types of III-nitride nanowire lasers

1.4.1 III nitride nanowire Fabry-Perot laser

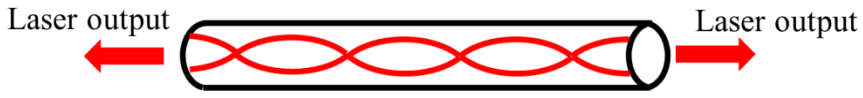

Figure 1.2 Scheme of a Fabry-Perot nanowire laser. A standing wave is formed in the nanowire cavity along the nanowire axis. The end-facets of the nanowire serve as the optical output couplers.

Most typical nanowire lasers are Fabry-Perot cavity nanowire lasers. In this case, the nanowire acts as a fiberlike waveguide. The cleaved end-facets of the nanowire serve as the output coupler, providing the optical cavity and forming a standing wave along the nanowire axis (Figure 1.2). A cavity mode of a Fabry-Perot cavity is composed of a transverse mode and a longitudinal mode. A transverse mode is a particular electromagnetic field pattern measured in a plane perpendicular to the propagation direction of the beam. A transverse mode depends on the cross-section of the nanowire waveguide. Figure 1.3 shows the profiles of the first six transverse modes supported by an InGaN/GaN multi-quantum-wells core-shell nanowire laser with a side length of 209 nm.

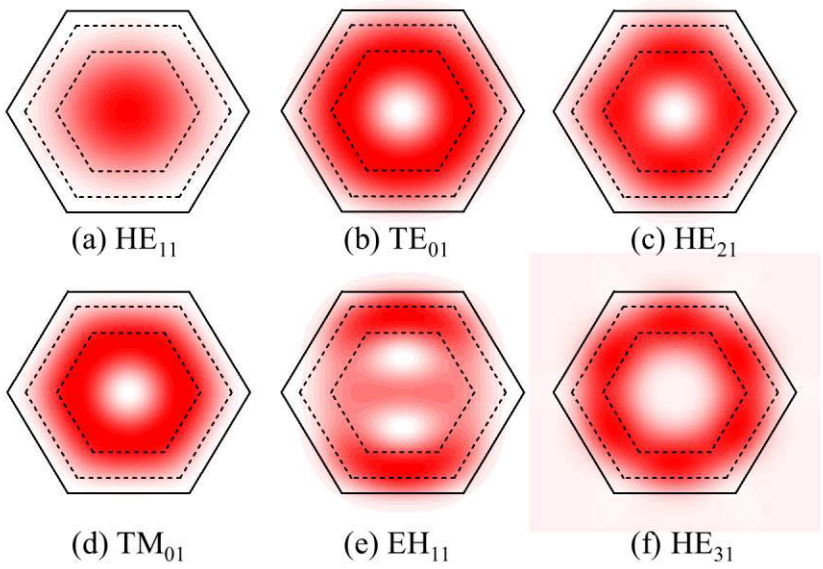

Figure 1.3 The profile of the electric fields of the first six order transverse modes supported by an InGaN/GaN core-shell nanowire with a side length of 209 nm.

When a transverse mode propagates along the nanowire waveguide, it will be reflected back by the end-facets of the nanowire. The transverse mode is constructively interfered when the round-trip phase shift equals $m \times 2\pi$, where m is an integer. In this case, the transverse mode forms a standing wave pattern in the propagation direction. The standing wave pattern is known as the longitudinal mode. According to the requirement of the constructive interference, the longitudinal mode spacing of a Fabry-Perot mode is given by:

$$\Delta\lambda = \frac{\lambda^2}{2L}\left(n(\lambda) - \lambda\frac{dn(\lambda)}{d\lambda}\right)^{-1} \tag{1.1}$$

Where L represents the length of the nanowire Fabry-Perot cavity, λ is the wavelength of the longitudinal mode, $n(\lambda)$ is the index of refraction at wavelength λ, and $n(\lambda) - \lambda\frac{dn(\lambda)}{d\lambda}$ represents the group index of refraction.

When a certain number of photons propagate along a nanowire waveguide, the number of photons might be changed by the combination of a stimulated emission process and a stimulated absorption process. The former process increases the number of photons, whereas the latter process reduces the number of photons. The change of the number of photons per unit propagation length is represented by a parameter known as material gain g.

$$I = I_0 e^{gL} \tag{1.2}$$

Where I_0 and I are the initial intensity and the final intensity of the propagating light, respectively, and L is the propagation length. Apparently, a positive material gain results

in a net amplification of the propagating light, whereas a negative material gain (loss) leads to a net reduction of the propagating light. Since only the portion of a propagating transverse mode located inside of the active region of a nanowire laser obtains optical gain, the modal gain $\langle g \rangle$ of the transverse mode can be written as:

$$\langle g \rangle = \Gamma g \tag{1.3}$$

Γ in equation (1.3) is the confinement factor, which is the ratio of the optical power of the transverse mode inside the active region to the total optical power of the transverse mode. Γ of nanowire lasers can be different from planar semiconductor lasers. Maslov et al. simulated the confinement factors for a *c*-oriented anisotropic wurtzite nanowire[43]. In the simulation, the confinement factor for a transverse mode is divided into the confinement factors for the electric fields parallel ($E_{\parallel}$ and $\Gamma_{\parallel}$) and perpendicular ($E_{\perp}$ and $\Gamma_{\perp}$) to the nanowire axis (Figure 1.4). $\Gamma_{\perp}$ increases monotonically as the diameter of the nanowire becomes larger. However, $\Gamma_{\parallel}$ reaches its maxima at a certain diameter and decreases for larger diameters. This is because that the larger diameter decreases the z-component of the electromagnetic field, resulting in a reduced $\Gamma_{\parallel}$. More importantly, nanowire lasers have much higher $\Gamma_{\parallel}$ than conventional edge emitting laser diodes. Due to the large contrast of index of refraction between a nanowire and the surrounding air, the critical angle of the total internal reflection for a transverse mode can be small. As a result, the actual propagation path of the transverse mode inside the nanowire can be much longer than the projection of the path along the z-direction. Since only the projection of the path on the z-direction is used to calculate the modal gain, the confinement factor, $\Gamma_{\parallel}$ can exceed unity.

As discussed above, a transverse mode experiences a reflective loss whenever it encounters the end-facet. In addition, the intensity of the transverse mode can also be reduced by the internal absorption (the energy of transfer from photons eventually to phonons) and scattering (the photons are scattered out of the lasing mode). Thus, the total modal cavity loss $\langle\alpha\rangle$ of a Fabry-Perot nanowire laser can be written as:

$$\langle\alpha\rangle = \alpha_m + \alpha_i = \frac{1}{L}\ln\left(\frac{1}{r_1 r_2}\right) + \alpha_i \tag{1.4}$$

Where L is the cavity length, r_1 and r_2 are the amplitude reflectivities of the two end-facets for the transverse mode, α_i is the internal loss from the internal absorption, and $\alpha_{m=}\frac{1}{L}\ln\left(\frac{1}{r_1 r_2}\right)$ is the mirror loss from the end-facet reflection.

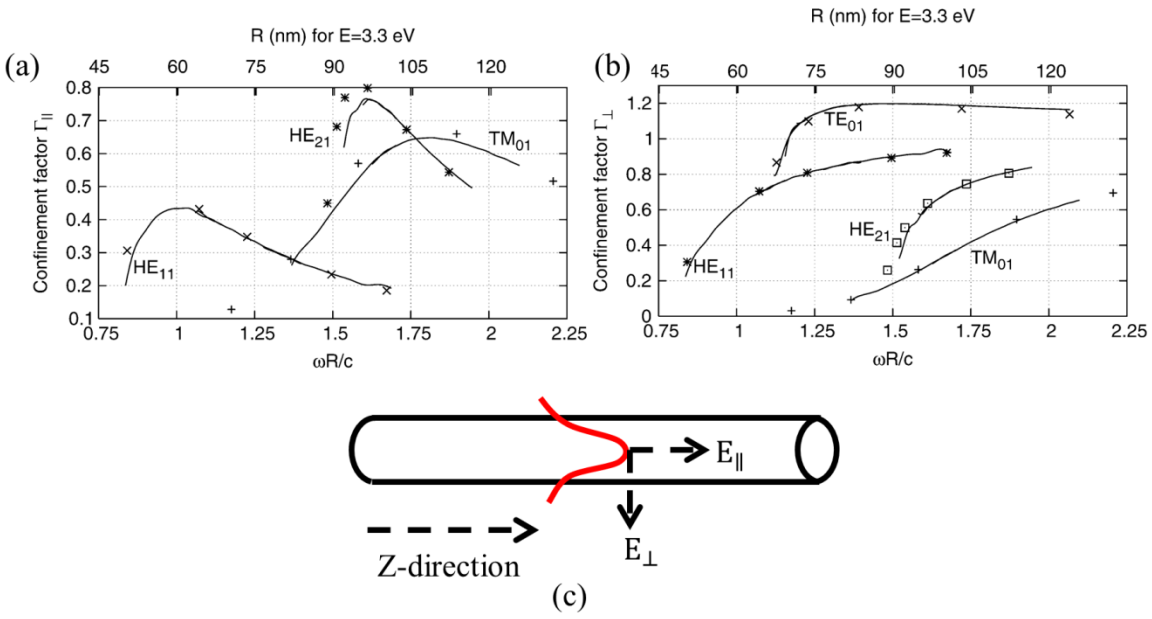

Figure 1.4 Simulated confinement factors for the electric fields (a) parallel and (b) perpendicular to the nanowire axis. (c) The scheme of the nanowire and electric field. Figure 1.4 (a) and (b) are taken from reference [43].

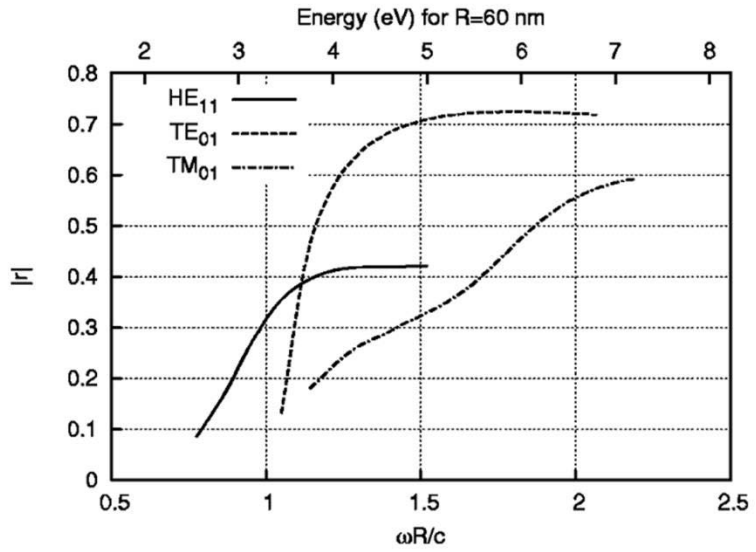

Figure 1.5 The simulated amplitude reflectivities of three transverse modes for a nanowire with an index of refraction of 2.45 and a radius of 60 nm. Figure taken from reference[44].

Unlike an edge emitting laser, the area of the end-facets of a nanowire laser is usually comparable to or smaller than the lasing wavelength. Therefore, the Fresnel equation is not applicable for calculating the reflectivity from an end-facet of a nanowire laser[44]. Figure 1.5 shows the amplitude reflectivities of the nanowire-air end-facet for the HE_{11}, TE_{01}, and TM_{01} modes as a function of the ratio of the lasing frequency to the radius of a nanowire. According to the plot, all the reflectivities for the three transverse modes increase monotonically as the radius of the nanowire increases or the lasing wavelength decreases, because of better mode confinement. However, as the mode confinement increases, only the amplitude reflectivity for HE_{11} mode approaches to the amplitude reflectivity for an infinite end-facet ($|r| = 0.42$ for $n = 2.45$). Furthermore, the mode confinement affects the amplitude reflectivity for the 3 transverse modes differently. As a

result, the dominant transverse modes can be engineered by varying the diameter or the lasing wavelength of a nanowire laser[45].

The change of the round-trip amplitude caused by the above reasons defines another important parameter of a nanowire laser – the lasing threshold. When a nanowire laser is pumped at a lower pump level, the round-trip optical gain is not sufficient to compensate the loss from both end-facets and the internal absorption. As a result, the transverse mode experiences a net round-trip loss and disappears eventually. On the other hand, when the nanowire laser is pumped at a level such that the round-trip optical gain equals the round-trip loss, the intensity of the transverse mode will remain constant. This pump level is called the lasing threshold. This round-trip optical gain is called the threshold modal gain $\langle g_{th} \rangle$.

$$\langle g_{th} \rangle = \Gamma g_{th} = \frac{1}{L} \ln\left(\frac{1}{r_1 r_2}\right) + \alpha_i \tag{1.5}$$

According to equation (1.1), the longitudinal mode spacing is inversely proportional to the cavity length. Therefore, a single longitudinal mode lasing can be achieved by reducing the length of a nanowire laser. However, reducing the length of a nanowire laser gives rise to a higher round-trip loss, and thus, a higher lasing threshold.

The first single GaN nanowire laser was demonstrated by Johnson et al. from Peidong Yang's group[46] in 2002. The GaN nanowire laser was grown by vapor-liquid-solid (VLS) epitaxy using Ni dots on a sapphire substrate as the catalyst. The diameters and lengths of GaN nanowire lasers were 30~150 nm and hundreds of microns, respectively. Pumped with a 300nm wavelength pulsed laser beam at room temperature, the GaN

nanowire laser reached its lasing threshold at ~3500-7000 kW /cm^2. The mode spacing of the amplified spontaneous emission from a 30 μm nanowire laser was calculated as ~ 1 nm, consistent with multi-longitudinal modes. Near-field scanning optical microscopy (NSOM) was also carried out to measure the spatial profile of the emission from the nanowire lasers. The NSOM result showed that the intensity of the emission was stronger at the tip of the GaN nanowire lasers than in the middle, implying strongly guided Fabry-Perot modes.

Following this pioneering research, Choi et al. from the same group fabricated a 11 nm diameter GaN quantum wire surrounded by a thick AlGaN cladding layer[47]. Since the thin GaN quantum wire could not provide efficient optical confinement by itself, the AlGaN cladding sheath was utilized to increase the diameter of the nanowire while maintaining a reasonable contrast of the index of refraction between the nanowire and the air. Lasing from the GaN exciton with a lasing threshold of 2-3 μJ/cm^2 was observed with optical pumping.

Although optically pumped lasing was demonstrated in two nanowire structures, their relatively high lasing thresholds limit their potential applications. In 2005, Gradečak et al. from Harvard University fabricated GaN nanowire lasers oriented in the non-polar *a*-direction [11-20][35] grown by metal-catalyzed (VLS) metal organic chemical vapor deposition (MOCVD). A low lasing threshold of 22kW/cm^2 was measured under optical pumping at room temperature. The low lasing threshold was considered to be a result of three factors: the triangular cross-sections, the Si doping, and the good surface morphology. It was also believed that the Si doping reduces the deep-level emission. The

dislocation-free nanowire lasers exhibit a good morphology, which reduces the scattering loss.

Fabry-Perot lasing was also demonstrated in other III-nitride nanowire lasers. In 2007, Hu et al. grew InN nanobelts with rectangular cross-sections on a SiN_x/Si substrate by MOCVD, using Au as the catalyst[48]. Multi-longitudinal mode lasing emission from multiple nanobelts was observed under optical pumping at 20 K. The lasing threshold was measured as 70 kW/cm^2. Assuming a group index of refraction of $n = 2.9$ and a longitudinal mode spacing of $\Delta\lambda = 7\,nm$, the required cavity length for such mode spacing was calculated as ~ 60 μm, which is consistent with the length of the nanobelts. A consistently larger longitudinal mode spacing ($\Delta\lambda = 11\,nm$) from a shorter nanobelt (~ 41 μm) was also measured, confirming that the lasing modes were Fabry-Perot modes.

In order to engineer the lasing wavelength and realize the electrically injected III-nitride nanowire laser, heterostructures and quantum wells are needed to be implemented on III-nitride nanowire lasers. In 2008, Qian et al. demonstrated the first single InGaN/GaN multi-quantum-well core-shell nanowire lasers under optical pumping at room temperature[49]. The core-shell nanowires were grown on an *r*-plane sapphire substrate by MOCVD using Ni clusters as the catalyst. The nanowires are along the non-polar *a*-orientation with triangular cross-sections. The sizes of the GaN cores are ~ 100-200 nm. Three types of nanowires with 3, 13, and 26 InGaN/GaN quantum wells surrounding the GaN cores were grown. Because of the triangular cross-section, the multi-quantum-wells were grown on the semi-polar [1-101] plane and the polar *c*-plane. The convergent-beam electron beam diffraction suggested that the *c*-plane is an N-polar [000-1] face. Because

of the slow growth rate on the N-polar *c*-plane[50], a significant difference in the growth rates was observed between the multi-quantum-wells on (1-101) plane and *c*-plane. For a nanowire with 26 quantum wells, the thicknesses of the multi-quantum-well regions are ~60 nm on the two (1-101) planes, and ~10 nm on the *c*-plane. By varying the In composition of the multi-quantum-wells from 5% to 23%, the lasing wavelength was tuned from 383 nm to 478 nm. Multi-longitudinal mode lasing with mode spacings of 0.72-0.82 nm was observed under optical pumping at room temperature. A 3-dimensional FDTD simulation was also carried out to simulate the transverse confinement factors and the Q-factors of the nanowire lasers. The simulation result showed that the nanowire with 26 quantum wells have a higher confinement factor ($\Gamma = 0.240$) and a higher Q-factor ($Q = 2485$) than the nanowire with 13 quantum wells ($\Gamma = 0.122$ and $Q = 656$). As a result, the lasing thresholds of the nanowire lasers with 26 multi-quantum-wells were 4-10 times lower across the 400-500 nm wavelength regime than the ones of the nanowire lasers with 13 multi-quantum-wells.

1.4.2 III-nitride surface-plasmon nanowire lasers

One major motivation for nanowire lasers is the miniaturization of the footprint of lasers. Although lasing has been demonstrated from basic dielectric nanowire cavities with diameters comparable to the lasing wavelength, the volume of the dielectric nanowire cavity is limited with the diffraction limit, which is $\sim(\lambda/2n)^3$, where λ and n are the wavelength and the index of refraction, respectively. In general, the mode confinement of the dielectric nanowire waveguide becomes poor as the diameter reduces to the medium's half-wavelength range. As a result, the lasing threshold increases dramatically as the

nanowire lasers are pushed to the smaller diameter regime, making the realization of skinnier nanowire lasers more difficult. In contrast to the traditional transverse modes of a dielectric waveguide, the surface plasmon polariton is highly confined at the interface between a metal and a dielectric layer, leading to an ultra-small mode volume. Therefore, surface plasmon nanolasers are considered as the promising devices that lead the nanolasers to the deep subwavelength regime.

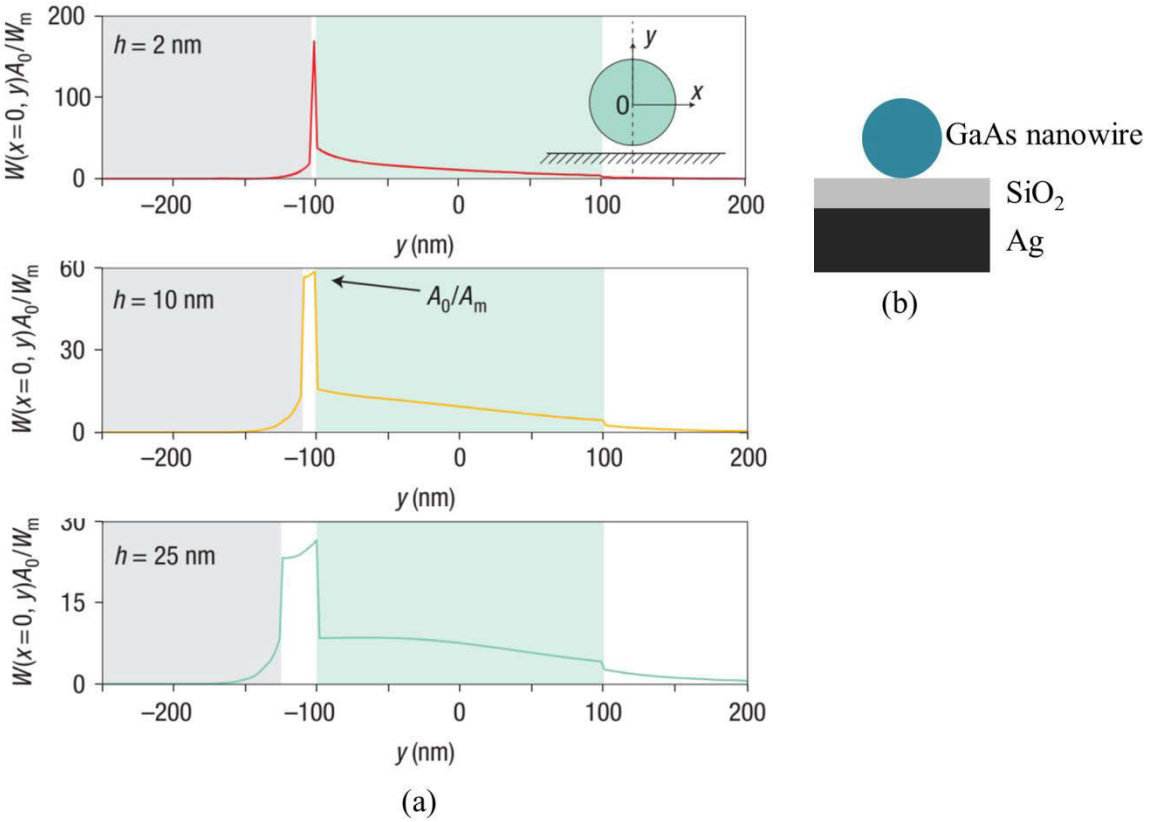

Figure 1.6 (a) Normalized energy densities of the hybrid surface plasmon mode for various SiO_2 thickness. (b) Scheme of the hybrid waveguide. Figure 1.6(a) is taken from reference [51]

It has been widely studied that one major difficulty for the surface plasmon nanolaser is the propagation loss from the metal substrate. In 2008, Oulton et al. from University of California, Berkeley proposed a hybrid plasmonic waveguide composing of a spacer layer with a low index of refraction between the semiconductor nanowire and the metal layer (Figure 1.6) [51]. Oulton et al. showed that the spacer layer is critical for both efficiently confining the mode in a small mode volume and reducing the propagation loss. Utilizing the hybrid plasmonic waveguide, the propagation length of the surface plasmon polariton can exceed more than 20 times of the wavelength. Based on this result, in 2011, Wu et al. demonstrated a plasmonics-coupled green nanolaser with a similar structure shown in Figure 1.6(b) using an InGaN/GaN axial heterostructure nanowire bundle. The nanowires are 680 nm in length and ~30 nm in diameter. The lengths of the InGaN and GaN sections are 300 nm and 380 nm, respectively. A 5 nm spin-on-glass (SOG) spacer layer was deposited between the nanowire bundle and a 50 nm thick colloidal Au nanoparticle plate for generating the surface plasmon plariton. A lasing peak centered at 533 nm was observed under optical pumping at 7 K, showing a threshold of ~300 kW/cm^2. Using a FDTD simulation, the mode volume was calculated as $\sim 0.14(\lambda/2n)^3$, which is below the diffraction limit.

In order to further reduce the propagation loss, Lu et al. from the same group showed that an epitaxially grown Ag film reduced the surface roughness, leading to a low scattering loss. The nanowire used for the surface plasmon nanolaser is a 480 nm long quasi InGaN/GaN core-shell nanowire. The nanowire is composed of a 170 nm long InGaN/GaN core-shell section and a 210 nm long GaN section. Using the epitaxially grown Ag film, a 5 nm thick SiO2 spacer layer, and a single nanowire, low lasing

thresholds of 2.1 kW/cm^2 and 3.7 kW/cm^2 were measured at 8 K and 78 K under optical pumping, respectively.

1.4.3 III-nitride nanowire polariton lasers

As discussed above, due to the large exciton bonding energy, GaN is a promising material for polariton lasing at room temperature. In 2011, Das et al. from University of Michigan demonstrated the first room temperature GaN nanowire polariton laser[52]. The GaN nanowire was ~60 nm in diameter and ~750 nm in length, placed in a SiO_2 λ-cavity sandwiched by two distributed Bragg reflectors (DBR). The DBRs are composed of 7 pairs of SiO_2/TiO_2 layers. Under optical pumping, a lasing threshold of 92.5 nJ/cm^2 for the polariton lasing was observed at room temperature. A typical polariton dispersion was also measured by angle-resolved photoluminescence. As the pump power continued increasing, a second lasing threshold of ~ 10^5 nJ/cm^2 was observed corresponding to a conventional photon lasing.

1.4.4 III-nitride nanowire ring lasers

Due to the small diameter and the large diameter/length ratio of nanowires, there has been significant interest in fabricating nanowire ring lasers. In this case, nanowires can be cut and folded to form ring resonators with controlled diameters. Compared to the traditional Fabry-Perot nanowire lasers, whispering-gallery-mode-based nanowire ring lasers could potentially achieve high Q-factors, and thus, low lasing thresholds. Furthermore, the cavity resonance of the ring laser can be tuned relatively easily by changing the diameter of the ring. Therefore, nanowire ring lasers offer the possibility for

realizing dynamic wavelength tunable lasers in future on-chip photonic integrated circuits.

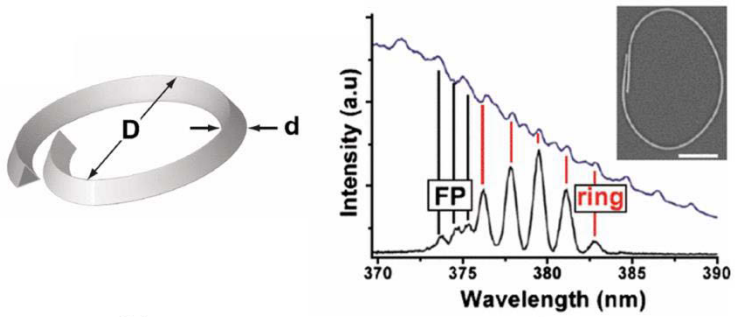

Figure 1.7 (a) Scheme of a nanowire ring resonator. (b) The photoluminescence spectrum of a nanowire ring resonator shown in the inset. Figures are taken from reference [53]

Pauzauskie et al. reported the first semiconductor nanowire ring laser in 2006[53]. The [1-10] oriented GaN nanowires were grown using chemical vapor transport process. The nanowires were cut to the desired length and folded into ring structures using a micro-positioning system (Figure 1.7). Under a low pump level, fringes corresponding to the whispering gallery modes (WGM) were observed on the spectrum after the nanowire is folded into a ring resonator. The mode spacing of 1.2 nm is consistent with the well-known equation of the mode spacing for WGMs:

$$\Delta\lambda = \frac{\lambda^2}{2\pi R\left(n - \lambda\frac{dn}{d\lambda}\right)} \tag{1.6}$$

Where n is the index of the refraction of the nanowire, R is the radius of the ring, and λ is the lasing wavelength.

Since the WGMs of the ring laser couple at the joint point through the evanescent wave, the coupling efficiency determines the loss of the WGMs. The evanescent wave outside the nanowire waveguide decays exponentially. The penetration depth of the evanescent fields given by:

$$d_p = \frac{\lambda}{4\pi n_w(\lambda)\left[\sin^2(\theta) - \left(\frac{1}{n_w(\lambda)}\right)^2\right]^{1/2}} \tag{1.7}$$

Using a Sellmeier dispersion relation for $n_w(\lambda)$, the penetration depths for wavelengths of 370 nm and 380 nm were calculated as 66 nm and 108 nm respectively. The result indicates that WGMs with longer wavelengths have better coupling efficiency than the ones with shorter wavelengths, implying that the WGMs are stronger at longer wavelengths. Consistently, the WGM fringes were only observed at the longer wavelength side of the spontaneous emission spectrum. Consequently, the center wavelengths of the nanowire ring lasers were redshifted by ~10 nm, compared to the linear structure counterpart. In addition, the lasing peaks shifted to longer wavelengths as the diameter of the ring laser is reduced, indicating higher required coupling efficiency for ring lasers with smaller diameters. A 1.5 times higher lasing threshold was measured for the ring lasers than the threshold of linear nanowire structure (~75 μJ/cm^2).

1.4.5 III-nitride nanowire photonic crystal lasers

Photonic crystals are periodic optical nanostructures. Similar to semiconductor crystals, the periodic index of refraction in photonic crystals mimics the periodic potentials for electrons. Therefore, the propagation of the electro-magnetic waves is affected by a photonic crystal, resulting in photonic band structures that are similar to the band

structures of semiconductor crystals. Photons with certain energies in the photonic bandgap are forbidden in a photonic crystal. Therefore, a photonic crystal can be used as an efficient reflector. If photonic crystals are placed surrounding an open area, photons with energies in the photonic bandgap are confined inside the open area, leading to an optical cavity formed by the photonic crystals. The photonic crystal cavity can also be converted into a photonic crystal laser when a gain medium is placed inside the cavity (Figure 1.8(a)). Since photonic crystals generally provide better optical confinement than the dielectric waveguides, higher Q-factors and smaller mode volumes can be achieved using a photonic crystal laser. Furthermore, photonic crystal lasers offer more degrees of freedom than single nanowire lasers for controlling the mode properties by varying the structure of the photonic crystal, such as the filling factor, the pitch, the index of refraction, the shape of the unit cell, and the pattern of the lattice.

Heo et al. demonstrated a photonic crystal laser using monolithic a single GaN nanowire as the gain medium[54]. The wurtzite GaN nanowires along the *c*-direction were grown on a Si (111) substrate by plasma-assisted molecular beam epitaxy (PA-MBE). The grown GaN nanowires have a length of ~600 nm and diameters of 20-50 nm. After the growth, a 380 nm thick SOG was spin-coated on the Si substrate followed by a 120 nm thick TiO_2 layer deposited by electron beam deposition. The contrast of index of refraction between the SOG and TiO_2 layers (1.4 vs. 2.5) provides the confinement in the vertical direction. After the deposition, a 2D photonic crystal with a hexagonal lattice of air holes was patterned on the TiO_2 layer using an electron beam lithography and an inductively coupled plasma etching (Figure 1.8(a)). The period and the hole diameter are 120-130 nm and 70-80 nm, respectively. A single nanowire was centered at the H2 defect

of the photonic crystal. A FDTD simulation showed a Q-factor of 570, a mode volume of $\sim 0.92(\lambda/n)^3$, and a confinement factor of 0.04 according to the fabricated photonic crystal structure. As a result, lasing was observed under optical pumping at room temperature with a threshold of 120 kW/cm^2.

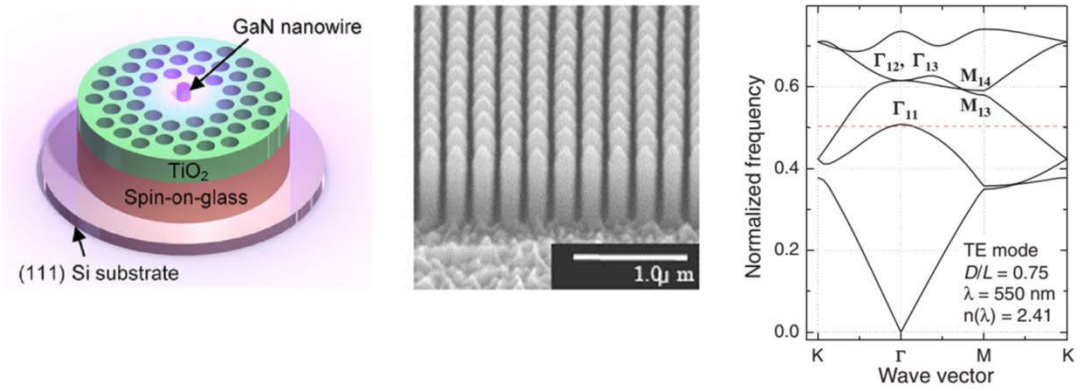

(a) (b) (c)

Figure 1.8 (a) Scheme of a GaN nanowire placed into a TiO_2 photonic crystal cavity, forming a photonic crystal laser[54]. *(b) The SEM image of a hexagonal lattice InGaN/GaN nanowire photonic crystal laser without a defect*[55]. *(c) The simulated band structure of a hexagonal lattice photonic crystal. A low group velocity is achieved at Γ_{11} point*[56].

Since the dispersion curve of a mode (a "band" in the band diagram) of a photonic crystal is normally flat at the Γ-point of a photonic crystal, the group velocity of the mode becomes nearly zero at the bandedge (Figure 1.8(c)) [56]. The near-zero group velocity provides lateral mode confinement for a photonic crystal laser. Therefore, a photonic crystal laser can be realized without a defect in the photonic crystal. Based on this principle, Kouno et al. fabricated InGaN/GaN multi-quantum-well nanowire photonic

crystal lasers[55]. The nanowires were along the c-direction with hexagonal cross-sections, grown by rf-plasma-assisted molecular beam epitaxy (rf-MBE). The selective-area growth technique offered precise control over the structure of the nanowire photonic crystal lasers. As a result, rectangular lattice photonic crystals were fabricated with periods of 216-249 nm and hexagon side lengths of 88-95nm (Figure 1.8(b)). The lasing threshold was 730 kW/cm^2 under optical pumping at room temperature. According to the FDTD simulation, lasing wavelengths for the TE modes were determined as:

$$\lambda = 3.56 \times S + 0.565 \times L \tag{1.8}$$

Where S and L are the hexagon side length and the period of the photonic crystal. Consistently, various lasing wavelengths were observed from photonic crystal lasers with two different hexagon side lengths and periods, showing the capability of engineering the lasing wavelength using a photonic crystal laser.

1.4.6 III-nitride nanowire random lasers

In contrast to the well-defined periodic structure of photonic crystal lasers, some vertically aligned nanowire assemblies grown by bottom-up techniques show randomly disordered or quasi-crystalline patterns (Figure 1.9). Unlike the regular scattering in a photonic crystal, the photons are randomly scattered by the nanowires. Although there is no designed optical cavity, the scattering may prevent the photons from leaking out of the nanowire assembly, resulting in a long photon life-time. Since the photon life-time basically represents the cavity loss, lasing could occur in a randomly grown nanowire assembly when the gain of the assembly overcomes the cavity loss (Figure 1.9(c)).

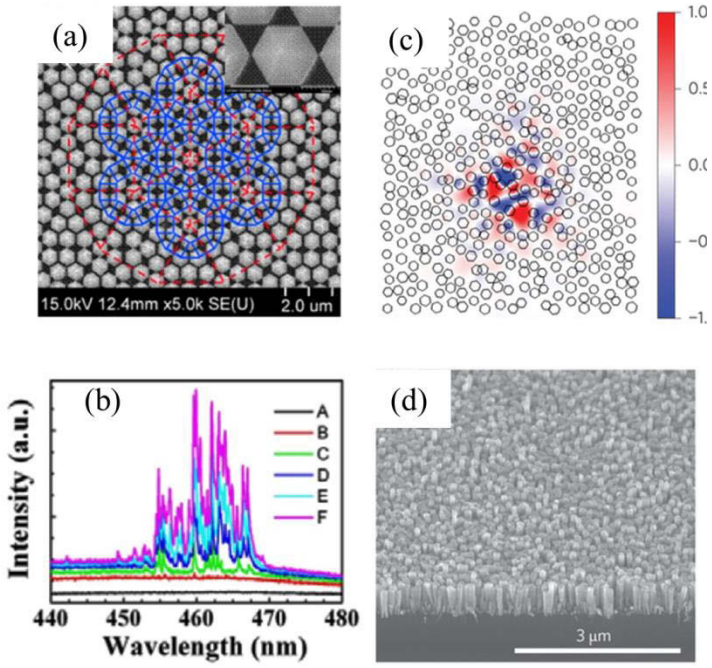

Figure 1.9 (a) The SEM image and (b) lasing spectra of a 12 fold symmetric GaN quasicrystal nanorod random laser [57]. *(c) The simulated confined mode and (d) the SEM image of a AlGaN nanowire random cavity*[58].

Chang et al. from National Chiao Tung University, Taiwan, observed the lasing action in GaN nanowire arrays under optical pumping[57]. The fabrication process starts with a 3 µm thick *c*-plane GaN epitaxial film grown on a *c*-plane sapphire substrate. Using an electron beam lithography, a 12-fold quasi-crystalline pattern of SiO_2 dots was defined on the GaN film (Figure 1.9(a)). 1 µm long GaN nanowires were then formed by inductively coupled plasma reactive ion etch (ICP-RIE). After the etch, InGaN/GaN multi-quantum-wells were grown on the GaN nanowires by MOCVD, resulting in nanowires with a hexagon side length of ~360 nm and a lattices constant of ~800nm. Irregular multi-mode lasing was observed when the nanowire assembly was pumped by a 355 nm frequency-

tripled Nd:YAG laser with a 50 μm diameter spot (Figure 1.9(b)). A high lasing threshold of ~ 5 MW/cm^2 was measured, possibly due to the random cavity rather than a well-defined Fabry-Perot cavity or a photonic crystal cavity. The result of a FDTD simulation showed various resonant wavelengths at different locations of the cavity, indicating the random lasing behavior.

The idea of random lasing also offers the ability to improve the performance of semiconductor lasers. For example, growing AlGaN with a low dislocation density and low residual strain has been challenging. Consequently, the lasing wavelengths of electrically injected semiconductor lasers are limited to the UV AI band (~340-400 nm). Alternatively, nanowires provide more efficient strain relaxation and lower dislocation density than the planar structures. Based on the idea of the random lasing, Li et al. demonstrated the first electrically injected semiconductor laser in the entire UV-AII band using an AlGaN nanowire assembly grown on a Si (111) substrate by molecular beam epitaxy (MBE) (Figure 1.9(d))[58]. The nanowires have a double heterostructure with 150 nm p-type and n-type $Al_{0.56}GaN$ capping sections, a 50 nm $Al_{0.3}GaN$ active region, and a 25 nm p-GaN contact layer. Al-rich AlGaN shells were confirmed by energy-dispersive X-ray spectrometry (EDXS) line scan across the active region along the axial direction. It is claimed that the AlGaN shell reduces the surface recombination rate. In order to achieve a high Q-factor, a 2-D simulation was utilized to study the Q-factor as a function of the diameter and the filling factor. According to the simulation, a high possibility of forming a high-Q cavity can be achieved with an average diameter of ~70-75 nm and a filling factor of ~30%. The voids between the nanowires were filled by polyimide deposition followed by an etch back process. Ni/Au and Ti/Au metal contacts

were subsequently deposited on the p-GaN tips and the n-Si substrate as the p- and n-contacts. Lasing was demonstrated under continuous electrical injection at 7-100 K. Two lasing peaks were observed at 332.7 nm and 334.1 nm. The lasing threshold was ~12 A/cm^2 at 7 K, which is nearly three orders of magnitude lower than the previous GaN-based UV laser diodes. The low threshold was attributed to the high-Q cavity, the low dislocation density, and the reduced non-radiative surface recombination.

1.5 Controlling the properties of lasing mode

1.5.1 Single mode control

Since optically pumped single nanowire lasers became increasingly mature, more attention has been paid to single-mode nanowire lasers. Four techniques have been reported for single-mode lasing: the dimension control technique, the coupled cavity technique, the external distributed feedback (DFB) technique, and the lossy substrate technique. The most straight forward technique to attain single-mode lasing from III-nitride nanowire lasers is reducing the dimensions of the nanowire lasers. One convenient method to control the dimensions of III-nitride nanowire lasers is the top-down two-step etching technique invented by Wang and coworkers from Sandia National Laboratories[59]. Owing to the top-down process, the diameter of the GaN nanowires is well-defined by the size of the etch masks and wet etch time. The length of the GaN nanowires is controlled by the thickness of the planar GaN substrate and dry etch time.

Based on the top-down two-step etching process, Li et al. demonstrated single-mode GaN nanowire lasers in 2012[60]. The fabricated GaN nanowire lasers were quasi-cylindrical.

Two nanowires with similar diameters but different lengths were selected for the experiment (nanowire A: 135 nm diameter and 4.7 μm long; nanowire B: 145 nm diameter and 7.2 μm long). Due to the small diameters of the two nanowire lasers, higher order transverse modes were cut-off, leaving only the fundamental transverse mode. According to the paper, when the pump power density reached the lasing thresholds, single mode lasing was observed from nanowire A with a side-mode suppression ratio (SMSR) of 18 dB, whereas multi-mode lasing was observed from nanowire B with a SMSR of 14dB. A numerical simulation was utilized to calculate the longitudinal lasing modes and the intensities. The calculation result showed that multi-longitudinal modes were able to reach the lasing threshold for nanowire B. However, because of the larger longitudinal mode spacing and the finite gain bandwidth of GaN, only one longitudinal mode dominated for nanowire A.

Although the dimension control offers an effective and intrinsic mechanism for single-mode lasing, the fabrication process can be difficult due to the small dimension, especially for AlGaN-based short wavelength nanowire lasers that need an even smaller diameter to achieve single-mode lasing. Coupled cavities using two nanowires[61] or folded single nanowire with loop mirrors[62] offer alternatives to the dimension reduction method. A coupled cavity is composed of two or more sub-cavities. The energy of the electromagnetic wave can transfer between the sub-cavities by evanescent wave coupling or direct coupling. Since the resonant wavelengths differ between sub-cavities, only the overlapped resonant wavelengths of the sub-cavities obtain high Q-factors (Vernier effect). Therefore, the coupled cavity provides a mode selection mechanism using Vernier effect.

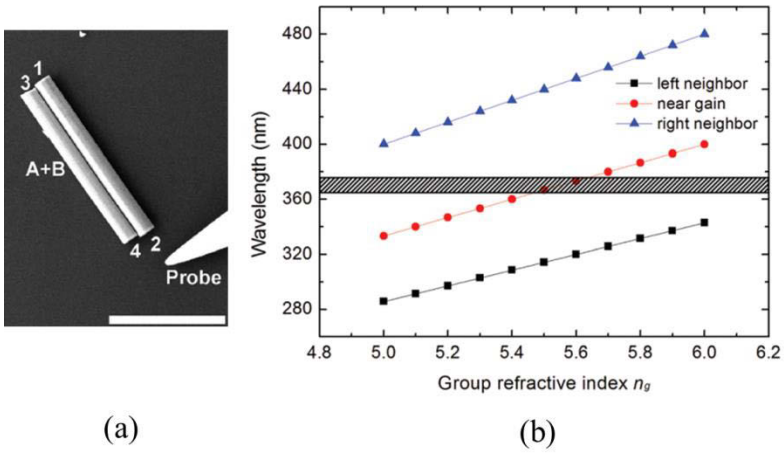

Figure 1.10 (a) The SEM image of the GaN nanowire pair. (b) The calculated overlapped wavelength of the transverse and longitudinal modes[63].

Xu et al. demonstrated single mode lasing from a GaN coupled nanowire pair[63]. In the paper, two GaN nanowire lasers (nanowire A: 680 nm in diameter and 7.6 μm in length, nanowire B: 720 nm in diameter and 8 μm in length) were optically pumped individually using a micro-photoluminescence (μ-PL) setup. Due to the large dimensions (diameters and lengths) and the short GaN band edge wavelength, both of the nanowire lasers support multi-transverse modes and multi-longitudinal modes. After the μ-PL measurement, the two nanowire lasers were placed side-by-side in contact by a nano-manipulator to form a coupled cavity (Figure 1.10(a)). Because of Vernier effect, single-mode lasing with a SMSR of 15.6 dB and a threshold of 874 kW/cm^2 was observed from the GaN nanowire pair laser. The sub-cavities of the previous coupled-cavity single mode CdSe nanowire lasers supports single transverse mode due to the long wavelength and the small diameters. However, the large diameters of the GaN nanowires allow for multiple transverse modes. To understand the mode selection mechanism of the coupled cavity for

transverse modes, the overlapped wavelengths of the GaN nanowire sub-cavities for both transverse and longitudinal modes were calculated in Figure 1.10(b). Due to the large separation of the overlapping wavelength for longitudinal modes, only two cavity modes locate in the gain spectrum of GaN (Figure 1.10(b)). Therefore, owing to the strong mode competition and the inhomogeneous gain between the modes, single transverse and longitudinal mode could be attained.

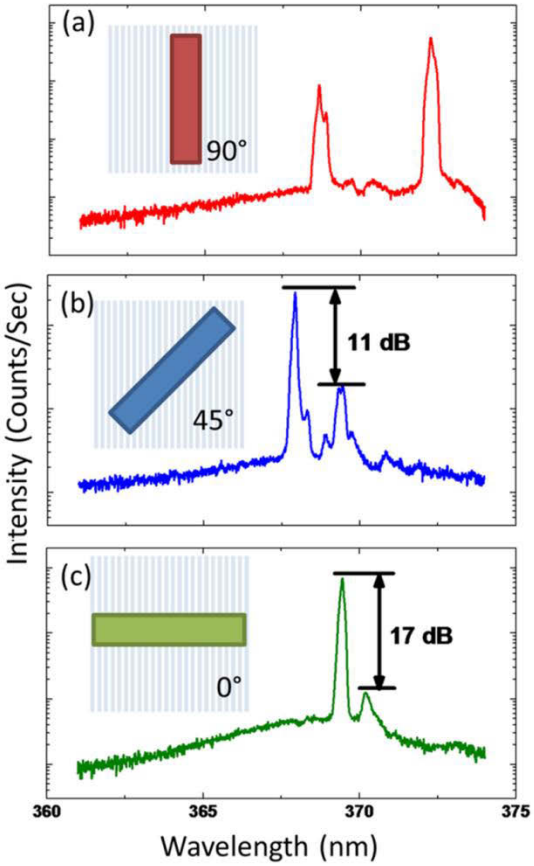

Figure 1.11 The spectra of lasing from the GaN nanowire laser on the DFB grating. The angles between the nanowire axis and the direction of the grating is (a) 90º, (b) 45º, and (c) 0º [64].

Although the coupled GaN nanowire-pair lowers the tolerance of fabricating single-mode GaN nanowire lasers, it requires a nano-manipulator to push two nanowires in contact. The manipulation could be significantly time-consuming and thus, limit the mass production of single mode nanowire-pair lasers. Instead of using a nanowire-pair, the stop band of an external DFB grating can also provide the mode selection mechanism by coupling the evanescent field of the lasing modes. Wright et al. transferred a GaN nanowire (~200 nm in diameter and 5 μm in length) onto a SiN_x DFB grating with a period of 90nm, a duty cycle of 50%, and a depth of 200 nm[64]. An eigenmode simulation followed by a transfer matrix method (TMM) was performed to calculate the stop band of the DFB waveguide composed of a GaN nanowire and a SiN grating. The simulation result showed a stop band with a suppression ratio of 15dB near the center of the gain bandwidth of GaN when the nanowire is aligned along the direction of the DFB grating. As the GaN nanowire deviates ±15º from the direction of the DFB grating, the stop band shifts beyond the long wavelength edge of the gain bandwidth. In the experiment, the angle between the GaN nanowire laser and the direction of the SiN_x DFB grating was then configured to be 0º, 45º, and 90º, using a nano-manipulator. Under optical pumping, multi-mode lasing was observed for the 90º configuration. As the angle decreased, the SMSR reduced from ~10dB to ~17dB, resulting a single mode lasing for the 0º configuration (Figure 1.11). In addition, despite the additional scattering loss possibly induced by the DFB grating, the lasing thresholds for the three configurations were not significantly different.

An even simpler method to obtain single-mode lasing is introducing a lossy substrate. When a GaN nanowire laser is placed on a lossy substrate, mode-dependent loss is

generated by the substrate, leading to single-mode lasing. Xu et al. observed single-mode lasing from a GaN nanowire laser on a gold substrate[65]. The GaN nanowire laser was first transferred onto a 300 nm thick SiN_x substrate. Due to the large dimension (~350 nm in diameter and 5.3 μm in length), the GaN nanowire laser exhibited multi-mode lasing under optical pumping. Following the first optical characterization, the GaN nanowire laser was then transferred onto a nearby photolithography-patterned gold region (200 nm in thickness and 120 μm in diameter). As a result, single mode lasing with a SMSR of 17.4 dB was observed from the GaN nanowire laser. Because of the additional propagation loss from the gold substrate, the lasing threshold increased by 13% from 241 kW/cm^2 to 276 kW/cm^2 after the nanowire is transferred onto the gold substrate. The mode-dependent propagation loss was calculated by an eigenmode solver, showing in Table 1.1. The calculated propagation loss for mode2 (HE_{11} mode) is significantly smaller than the ones for other transverse modes, resulting in a single HE_{11} mode lasing. Similar single-mode lasing was observed with other GaN nanowire lasers on a gold substrate with diameters ranging from ~250 nm to ~400 nm, confirming the repeatability of the lossy substrate method.

Table 1.1 The gold substrate induced propagation loss for the 10 lowest order transverse modes of a 300nm-diameter GaN nanowire.

	Mode 1	**Mode 2**	**Mode 3**	**Mode 4**	**Mode 5**
Loss (dB/cm)	8151	1730	4806	7109	16041
	Mode 6	**Mode 7**	**Mode 8**	**Mode 9**	**Mode 10**
Loss (dB/cm)	43858	7551	22205	29175	28706

1.5.2 Wavelength tuning

Since the lasing wavelength depends largely on the bandgap wavelength of the active region, the wavelength control of CdS_xSe_{1-x} nanowire lasers grown on a quartz substrate has been demonstrated by utilizing a spatial sulfur composition grading across the quartz substrate[66]. As a result, the lasing wavelengths of the CdS_xSe_{1-x} nanowires grown on the quartz substrate varied depending on the location of the nanowires. The sulfur composition grading was also demonstrated for single CdSSe nanowires grown by source-moving chemical vapor deposition method[67]. Consequently, by cutting the CdSSe nanowire into segments, various lasing wavelengths can be obtained from individual CdSSe nanowire segments. The wavelength control was also realized in CdS nanowires with a fixed bandgap[68]. The exciton−polaritons propagating along the nanowire lose their energy by phonon scattering, leading to an increasing lasing wavelength. Because the energy loss depends on the length of the nanowires, the lasing wavelength red shifts for long CdS nanowire lasers. The wavelength control was also attained using surface plasmon polariton enhanced Burstein−Moss effect, wherein the wavelength of photonic lasing modes of the CdS nanowire blue shifted when the spacing between the nanowire and the gold substrate was reduced[69].

Albeit the above techniques offer wavelength control, they are unable to tune the lasing wavelength. Based on the principle of nanowire photonic crystal lasers discussed in this chapter, Ishizawa et al. from Sophia University showed on-chip wavelength tuning using the Γ-point band edge of the second photonic band of hexagonal-lattice InGaN/GaN

MQW nanowire photonic crystal lasers[56]. An on-chip wavelength tuning range of 82.6 nm was achieved by varying the lattice constant and the diameter of the nanowires.

The drawback of Ishizawa's work is that the nanowires only have one gain section, and thus, limited gain bandwidth for the wide wavelength tuning. Therefore, the photonic crystal laser requires two samples with different In compositions to realize the wide tuning range. Wright et al. fabricated InGaN/GaN MQW nanowire photonic crystal lasers with dual gain sections[70]. Gain section 1 contains InGaN multi-quantum-wells with an emission centered at 430 nm. Gain section 2 is a 150 nm thick $In_{0.02}GaN$ under layer with an emission centered at 385 nm. The dual gain sections give rise to a wide gain bandwidth, and thus, a 60 nm wide tuning range from 380 nm to 440 nm.

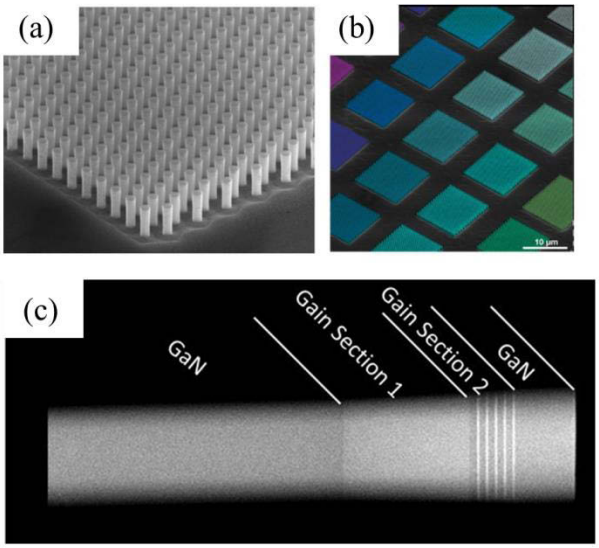

Figure 1.12 The SEM images of (a) single InGaN/GaN multi-quantum-well nanowire photonic crystal pixel and (b) multiple pixels. (c) The TEM image of a single InGaN/GaN multi-quantum-well nanowire[70].

Dynamic and continuous wavelength tuning from single GaN nanowire lasers was realized by Liu et al[71]. A regular top-down GaN nanowire laser was placed into a diamond anvil cell filled with silicone oil. As the spacing of the diamond anvil cell was reduced, the silicone oil created a high hydrostatic pressure, resulting in a hydrostatic-pressure-dependent bandgap shifting of GaN nanowires given in the following equation:

$$E_g = 3.408 + 6.09 \times 10^{-2} P - 2.36 \times 10^{-3} P^2 \quad (eV) \tag{1.6}$$

Where P is the applied hydrostatic pressure in GPa. Because of the bandgap shifting, the lasing wavelength from the same GaN nanowire laser was continuously and dynamically tuned from 367 nm to 337 nm with a resolution of <0.5 nm.

1.5.3 Polarization control

Following the research in reference[65], Xu et al. further studied the polarization of the least lossy HE_{11} mode for GaN nanowire lasers placed on a gold substrate. The simulation result showed that the least lossy (0.36 dB/μm) HE_{11} mode is polarized parallel to the gold substrate surface. The low propagation loss can be explained by a weak coupling between this TE-like HE_{11} mode and the surface plasmon. On the other hand, the other degenerate HE_{11} mode polarized perpendicular to the gold substrate surface has higher loss (2.11 dB/ μm), due to the strong coupling between this TM-like HE_{11} mode and the surface plasmon. As a result, linear polarizations parallel to the gold substrate surface was experimentally observed for five GaN nanowire lasers lying on a gold substrate, with an average extinction ratio of 20:1. In comparison, elliptical polarizations with random polarization angles were observed from another five GaN

nanowire lasers hanging off the edge of the substrate. The results proved that the polarization of GaN nanowire lasers can be controlled by using a lossy gold substrate.

1.6 Organization of the dissertation

In first half of this dissertation, the top-down two-step etch process was applied for controlling the cross-section of III-nitride nanowires. As shown in this work, control of the cross-section offers a method to intrinsically control the lasing properties of nanowire lasers, without external requirements or elements, including beam shape and polarization. In order to pursue electrically driven single III-nitride nanowire lasers, the top-down two-step etch process, in combination with regrowth, is utilized for fabricating non-polar InGaN/GaN multi-quantum-well core-shell nanowire lasers, discussed in the second half of this dissertation.

Chapter 1 introduces the advantages of III-nitride semiconductors and nanowire lasers, summarizes the type of III-nitride nanowire lasers, and reviews previously reported techniques for controlling the lasing properties.

Chaper 2 details the methodologies of the fabrication, the optical characterization, and the numerical simulation of III-nitride nanowire lasers.

In Chapter 3, annular-shaped emission is demonstrated from GaN nanotube lasers fabricated by the top-down two-step etch process. A finite-difference time-domain (FDTD) simulation was applied to calculate the far-field from multiple transverse modes.

Chapter 4 presents linearly polarized emission from rectangular cross-sectioned GaN nanowire lasers. The rectangular cross-section gives rise to the contrast of the index of

refraction when the shorter y-dimension is ~120 nm. As a result, y-polarized transverse modes achieved higher transverse confinement factors than the x-polarized modes, leading to dominant y-polarized lasing.

Chapter 5 demonstrates the first optically pumped non-polar InGaN/GaN multi-quantum –wells core-shell nanowire lasers at room temperature. Compared to the previously reported semi-polar core-shell nanowire lasers, a lower lasing threshold was measured from the non-polar core-shell nanowire lasers. The low lasing threshold was attributed to a higher modal gain of the non-polar core-shell nanowire lasers measured using the Hakki-Paoli method. Non-uniform modal gains from 7 core-shell nanowire lasers due to inhomogeneous regrowth is also confirmed by the Hakki-Paoli method.

Chapter 6 shows the research towards electrically driven core-shell nanowire lasers. A "ohmic-like" contact to n-GaN core of the core-shell nanowire lasers was achieved using Ti. However, the ohmic contact to p-GaN shell was not achieved, resulting in a low injection efficiency. Therefore, only a weak spontaneous emission was observed in the electroluminescence measurements.

Chapter 7 summarizes the research in this dissertation and discusses some future work.

Chapter 2

Fabrication, characterization, and numerical simulation techniques for III-nitride nanowire lasers

2.1 Top-down two-step etching process

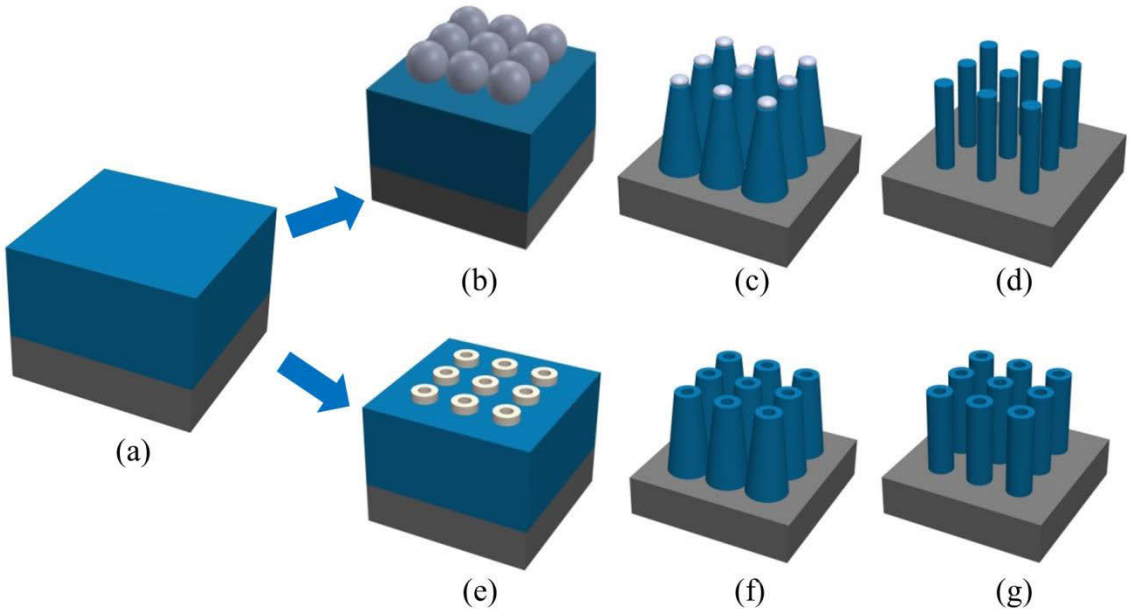

Figure 2.1 Sketches of the top-down two-step etch process. (a) Planar GaN or III-nitride epilayer grown on a c-plane sapphire substrate. Silica micro-spheres and Ti/Ni are deposited on the epitaxial film as etch masks by (b) a LB patterning and (d) an e-beam lithography. (c) and (f) The patterns of the etch masks are transferred into the epilayer by ICP etch. (d) and (g) III-nitride nanowires with straight and smooth sidewalls are created by the AZ400K wet etch.

The III-nitride nanowires in this dissertation are fabricated using a top-down two-step etching process developed by Wang and coworkers and shown in Figure 2.1 [59]. The process starts with a regular *c*-plane planar III-nitride homogeneous or hetero-structure epilayers grown on a *c*-plane sapphire substrate by metal organic chemical vapor deposition (MOCVD) (Figure 2.1(a)). The structure of the planar epitaxial film can be designed according to the application of the nanowire and transferred to the nanowires fabricated from the epitaxial film.

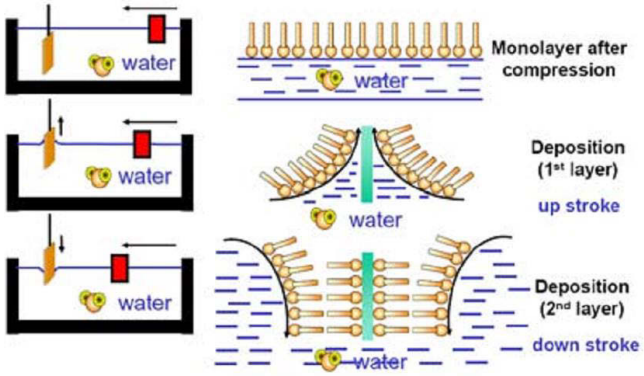

Figure 2.2 Scheme of Langmuir Blodgett patterning of monolayer and double layer colloidal particle on a substrate[72].

After the epilayer growth, a monolayer of silica microspheres is deposited on top of the III-nitride film as the etch mask by a Langmuir-Blodgett (LB) deposition technique shown in Figure 2.2 [72]–[74]. An LB film is formed at the water-air interface using amphiphilic molecules. Amphiphilic molecules are composed of a hydrophilic 'head' and a hydrophobic 'tail'. When the molecule concentration is far less than the critical micellar concentration, the molecules randomly align. However, for a small molecular area (high concentration), the molecules form a compact monolayer at the water-air interface, with

the hydrophobic ‘tail’ exposed to the air and the hydrophilic ‘head’ emerged in the water. Consequently, a monolayer of particles can be deposited on a substrate when the substrate moves across the water-air interface. Because the molecular area is a function of the surface pressure, the surface pressure is monitored during the deposition by a Wilhelmy plate or a Langmuir balance to maintain the molecular area.

Although the Langmuir Blodgett patterning is a lithography-free technique for large area patterning, it is difficult to deposit single crystalline monolayers over large regions on the substrate. In contrast to the LB patterning, electron-beam (e-beam) lithography offers the ability to control the shape, dimension, and the period of the mask pattern, with small feature sizes possible. For e-beam lithography, a positive e-beam resist (495 polymethyl methacrylate (PMMA) C6 from MicroChem) was spin-coated on top of the III-nitride planar epitaxial film. The normal spin speed is ~ 5000 rpm, resulting in a PMMA thickness of ~600 nm. The thickness of the PMMA can also be tuned by varying the spin speed or choosing PMMAs with different concentrations. The PMMA was then baked at ~170ºC for 5 minutes. E-beam lithography (a JEOL electron beam lithography system or a nanometer pattern generation system (NPGS)) was then applied to define patterns with various shapes. The patterns were transferred into openings in the PMMA layer through development in a 3:1 methyl isobutyl ketone (MIBK)/isopropanol alcohol(IPA) solution. Subsequently, Ti/Ni (typical thicknesses: 10 nm/ 200 nm) was deposited on the sample by e-beam metal evaporator to act as the dry etch mask (Figure 2.1(e)). The selectivity of the ICP etching between GaN and Ni is measured as ~30:1-40:1. Finally, the Ti/Ni on top of the PMMA film was lifted-off by soaking in an acetone solution, leaving only the Ti/Ni patterns defined by the e-beam lithography.

The pattern of the etch mask was then transferred into the III-nitride film by chlorine-based ICP dry etching (Etch step 1), forming III-nitride nanowires (Figure 2.1(c) and (f)). Due to the physical etching, the sidewalls of the nanowires are rough and tapered. A KOH-based crystallographic selective wet etching (Etch step 2) was performed by dipping the nanowire sample into an AZ400K photoresist developer at 65ºC. The AZ400K does not attack the Ga-polar *c*-plane, but has a relatively higher etch rate for the semi-polar planes and a lower etch rate for non-polar planes. As a result, the slow etched planes are evolved after the wet etch, forming nanowires with smooth and straight non-polar sidewalls (Figure 2.1(d) and(g)).

The top-down two-step etching process offers many advantages. First, the top-down two-step etching process simplifies the growth process, because of the mature planar growth technique. Second, the material properties of the nanowires fabricated by the top-down two-step etching process can be measured directly from the planar substrate. However, it is extremely difficult to measure the material properties of the bottom-up nanowires, due to their size, wire-to-wire variations, and the lack of planar reference samples. Additionally, the top-down two-step etching process provides a method to control the pattern of the nanowires, such as the shape and dimension of the nanowire cross-section, and the period and the lattice of nanowire photonic crystal lasers. This freedom opens a potential route to intrinsically control the lasing properties of III-nitride nanowire lasers, such as the beam shape, the polarization, and the confinement factor.

2.2 Micro-photoluminescence experimental setup

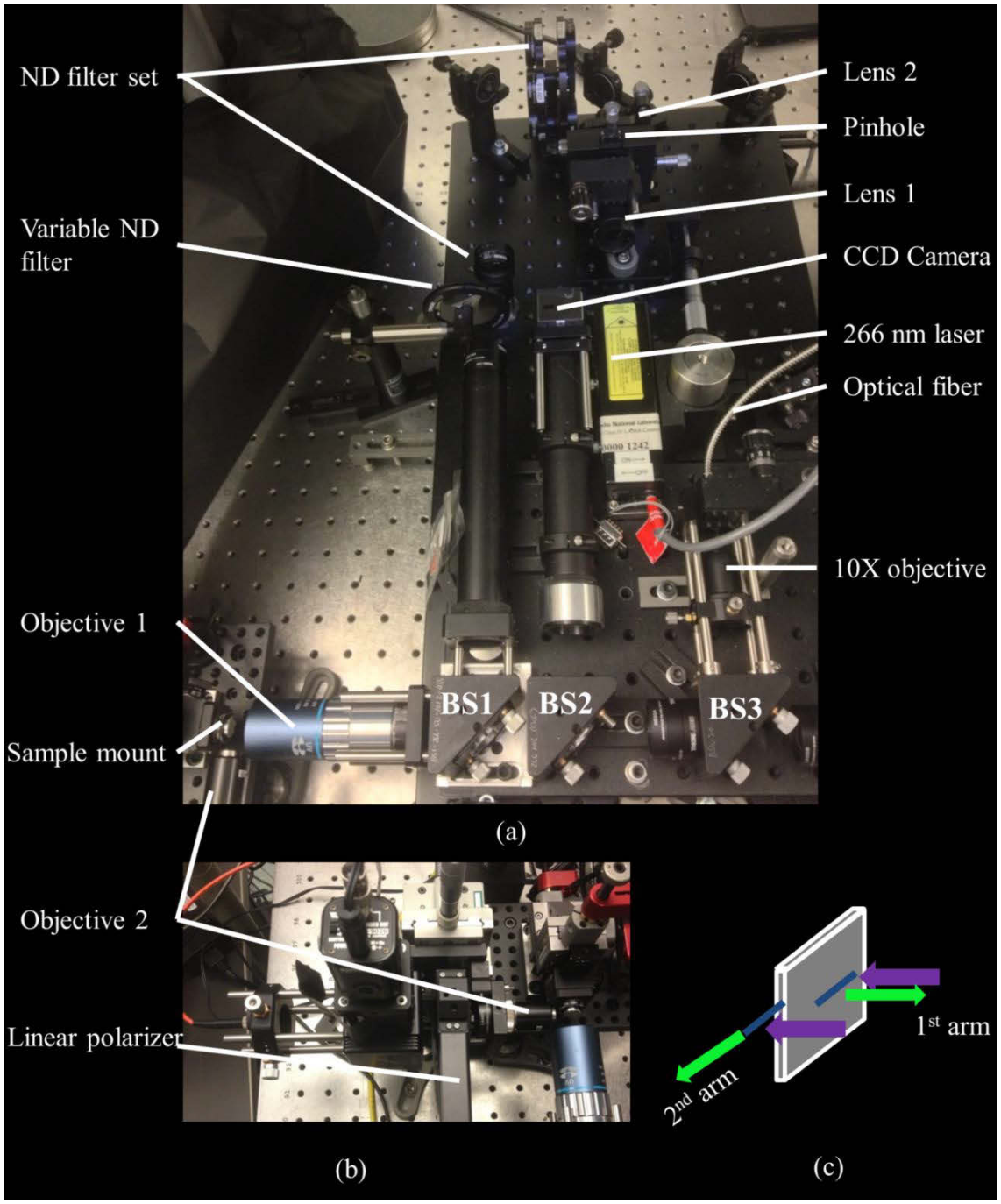

Figure 2.3 The (a) The first arm and (b) the second arm UV μ-PL experimental setup. (c)The scheme of the configurations for measuring the scattered and the end-facet emission of nanowire lasers. A nanowire lying on a substrate and a nanowire hanging off the edge of the substrate are optically pumped from the 1st arm (purple arrow). The scattered emission from the lying nanowire is collected by the 1st arm (green arrow). The end-facet emission from the "hanging" nanowire is collected by the 2nd arm (green arrow).

The III-nitride nanowire lasers are optically characterized using the 2-arm micro-photoluminescence (μ-PL) setup shown in Figure 2.3. A pulsed frequency-quadrupled Nd:YAG laser operating at 266 nm is used as the pump laser. The pump laser has a pulse width of 400 ps, a duty cycle of 0.0004%, and a repetition rate of 10 kHz, allowing for reduction of heating effects of the pumped nanowire lasers. The pump laser beam is focused onto a 25 μm pinhole by Lens 1 (f=75) to filter out the higher order transverse modes, leaving only the fundamental mode. After passing through the pinhole, the pump laser beam is collimated by Lens 2 (f=25) and then reflected by a high energy plate beam splitter (BS1). A 50X Mitutoyo plan UV infinity corrected objective (Objective 1) is placed behind BS1 to focus the collimated pump laser beam to a spot with a diameter as small as ~1 μm. A UV lens can also be placed before Objective 1 to defocus the spot for a uniform pumping. A nanowire sample is mounted on a motor-driven linear stage and located at the focal plane of Objective 1. Therefore, the emission from the nanowire sample can be collected effectively by Objective 1 and re-focused by a Thorlabs 10X UV objective onto a UV fiber. The UV fiber then transmits the emission to a holographic grating spectrometer (Princeton Instrument SP2300i) to capture the spectrum. A dichroic beam splitter (BS2) and Lens 2 was used to block the 266 nm pump laser and image the nanowire sample to a CCD camera located at the conjugate plane of the nanowire sample.

For the regular characterization, III-nitride nanowire lasers can be transferred lying onto a SiO2/Si or a sapphire substrate by a cotton swab. In this case, Objective 1 simply collects the lasing emission from the nanowire lasers scattered by the end-facets of the nanowire or the substrate (Figure 2.3(c)). However, the direct end-facet emission cannot be captured by this configuration, because of not only the orientation of the nanowire lasers

but also the polarization dependent transmission of the beam splitters. As a result, some lasing properties, such as the beam shape and the polarization of the emission, cannot be measured using this configuration. In order to capture the direct end-facet emission, the nanowire lasers are transferred hanging off the edge of a substrate, pointing to the second arm placed perpendicular to the first arm. Consequently, while the nanowire laser is pumped by the first arm from the side, the end-facet emission is captured by the 40X objective (Objective 2) in the second arm and transmitted to the spectrometer (Figure 2.3(c)). A linear polarizer was also mounted after Objective 2 to analyze the polarization of the end-facet emission.

In order to measure the lasing thresholds of the nanowire lasers, a neutral density (ND) filter set and a variable ND filter were located between Objective 1 and Lens 2 to continuously vary the pump power density. The power of the pump laser transmitted through BS1 was measured by a Thorlabs PM100 optical power meter and calibrated to the pump power on the nanowires according to the transmittance and reflectance of BS1. The details of the principle of the lasing threshold measurement are discussed in Chapter 3, Chapter 4, and Chapter 5.

2.3 Micro-electroluminescence experimental setup

The μ-PL setup was also utilized as a micro-electroluminescence (μ-EL) setup. In this case, the nanowire lasers were transferred onto a SiO_2/Si platform dedicated for the electrical injection. The p-GaN and n-GaN regions of nanowire lasers were electrically connected to the contact pads on the platform, which are electrically connected to the pins on a dip header by wire-bonding. The dip header was then plugged into a socket

mounted a 3-axis stage. A Keithley sourcemeter and a voltage pulse generator were employed to electrically inject the nanowire in a CW mode and a pulse mode, respectively. The emission from the nanowire was collected by the first arm of the μ-PL setup and analyzed in the same way described in section 2.3.

2.4 Simulation of III-nitride nanowire lasers

2.4.1 Finite difference eigenmode simulation

Lumerical Mode solutions [75] is a commercial 2-dimension finite difference eigenmode (FDE) solver designed to calculate the properties of the transverse modes of a waveguide, such as the mode profile, the propagation loss, and the dispersion. In this dissertation, Lumerical Mode solutions is employed to calculate properties of the transverse modes of the III-nitride nanowire lasers. The model of the FDE simulation is illustrated in Figure 2.4 as an example. A cylindrical GaN nanowire is placed at the center of the simulation. The index of refraction was measured by an ellipsometry from a GaN film grown on a sapphire substrate. A non-uniform mesh is defined using the finite difference algorism in the software to shorten the simulation time. A perfectly matched layer (PML) is used as the boundary condition to eliminate the interference of the boundary on the simulation. A PML is an efficient artificial absorber that does not reflect the electromagnetic wave that is incident on it. After setting the wavelength of the nanowire waveguide mode, the solver finds the modes profiles and the effective indices of the transverse modes by solving the Maxwell's equations at each mesh point.

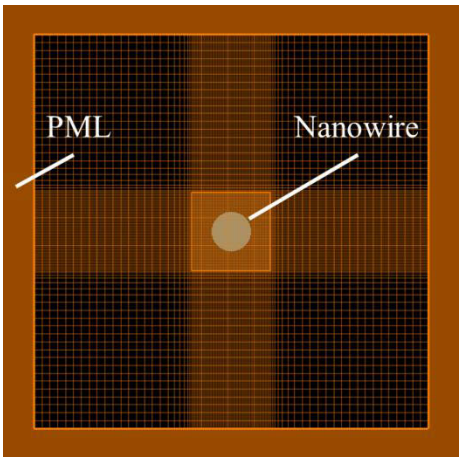

Figure 2.4 An example of the model of the FDE simulation.

2.4.2 Bidirectional eigenmode expansion simulation

A bidirectional eigenmode expansion (EME) simulation[75] is ideal for calculating the propagation loss of a tapered nanowire. In the EME simulation, a tapered nanowire is sliced into sections perpendicular to the nanowire axis with varying cross-sections. The EME solver then finds the mode profiles for each individual cross-sections. Next, the scattering matrices for each section is calculated by matching the tangential E and H fields at the section boundaries. The overall scattering matrix of the nanowire can then be calculated based on the scattering matrices for each section. Therefore, the field distribution and the propagation loss of the tapered nanowire can be calculated. The EME simulation significantly reduces the simulation time, compared to the FDTD simulation.

2.4.3 Finite-difference time-domain simulation

The FDE simulation has limitations. First, the FDE simulation only analyzes the properties of individual transverse modes. Therefore, it is impossible to calculate the

properties of a combination of transverse modes. Second, as a 2-D simulation, the FDE simulation is not able to calculate the cavity properties, such as the Q-factor and the resonant spectrum. In this dissertation, FDTD simulations[76] are utilized to simulate the far-field of a combination of multi-transverse modes from a III-nitride nanotube laser.

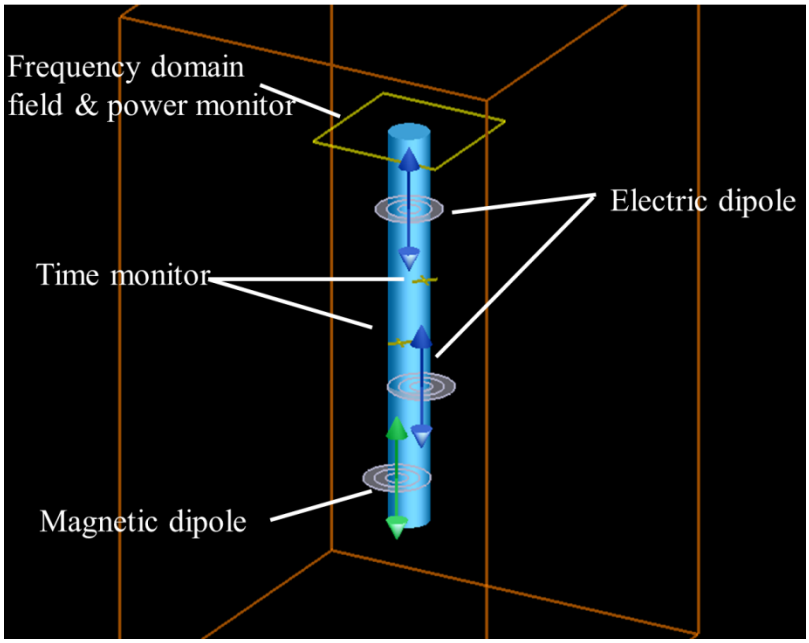

Figure 2.5 An example of the model for the FDTD simulation.

In an FDTD simulation, the time-dependent partial differential Maxwell's equation is discretized in the space and time partial derivatives. Next, the E-field distribution at one instant in time is solved. Based on the stored value of the H-field and the numerical curl of the local distribution of the E-field in space, the H-field time derivative, and thus, the H-field at the next instant in time can be calculated. Using the spatial H-field distribution, the E-field at the following instant in time can also be calculated. By using the leapfrog manner, the evolution of the electromagnetic field is solved. A model of a FDTD simulation is shown in Figure 2.5 as an example. Electric and magnetic dipoles are

randomly placed inside of the nanowire to excite all the cavity modes. Time monitors are also randomly placed inside of the nanowire to record the time-dependent intensity of the electromagnetic field. The data of the time-dependent intensity can be used to calculate the spectrum and the Q-factor of the cavity modes. Frequency domain field & power monitors can be placed at the planes of interest to record the electromagnetic field distribution.

2.5 Hakki-Paoli gain measurement

The most common methods for measuring the optical gain of semiconductor lasers are the segmented contact method[77] and the Hakki-Paoli method[78], [79]. The segmented contact method is not suitable for the gain measurement of top-down nanowire lasers because of their compact size. Alternatively, the Hakki-Paoli method is chosen to measure the modal gain of InGaN/GaN multi-quantum-well core-shell nanowire lasers.

Consider a field of a transverse mode F_1: the mode propagates along the nanowire with a propagation constant of $k - \frac{1}{2}\alpha$, where α is the net loss constant. A negative α represents a net gain of a nanowire laser. When the transverse mode is incident on the end-facets of a nanowire with reflectance of R_1 and R_2, respectively, part of the transverse mode is transmitted through the end-facets. The output optical field from an end-facet is the summation of the multiple passes. If the multiple passes interfere constructively, the output field can be calculated as:

$$F_{1T}^{+} = F_1 \sum_{n=0}^{\infty} (R_1 R_2)^{n/2} \exp(-n\alpha L) = F_1 / \left[1 - (R_1 R_2)^{1/2} \exp(-\alpha L)\right] \quad (2.1)$$

One the other hand, the destructive interfered output field is:

$$F_{1T}^{-} = F_1 / \left[1 + (R_1 R_2)^{1/2} \exp(-\alpha L)\right] \tag{2.2}$$

When the nanowire is optically pumped, the amplified spontaneous emission (ASE) fringes can be captured by a spectrometer. The intensity of the ASE peak, $P^{+} = (F_{1T}^{+})^2$, and the intensity of the adjacent valleys, $P^{-} = (F_{1T}^{-})^2$, can be measured. Using equation (2.1) and (2.2), the net loss constant α can be calculated as:

$$\alpha(\lambda) = \frac{1}{L} \ln \frac{\sqrt{P^{+}} + \sqrt{P^{-}}}{\sqrt{P^{+}} - \sqrt{P^{-}}} + \frac{1}{2L} \ln R_1 R_2 \tag{2.3}$$

Chapter 3

Annular-shaped emission from gallium nitride nanotube lasers

This chapter is part of a published paper entitled "Annular-Shaped Emission from Gallium Nitride Nanotube Lasers" in ACS Photonics, which is published online on July 13th, 2015[80].

3.1 Introduction

The annular-shaped emission from a nanowire laser could potentially benefit the applications such as atom trapping and stimulated emission depletion microscopy. In addition, inorganic nanotubes can be used as ultracompact channels for nanofluidic devices[81]. Research on nanofluidic systems have opened a new window for many applications, such as analytical separation and determination of biomolecules[82]. In this chapter, we demonstrate optically pumped lasing from hollow-cross-section, GaN nanotubes fabricated by a two-step top-down technique.

3.2 Fabrication of the GaN nanotube lasers

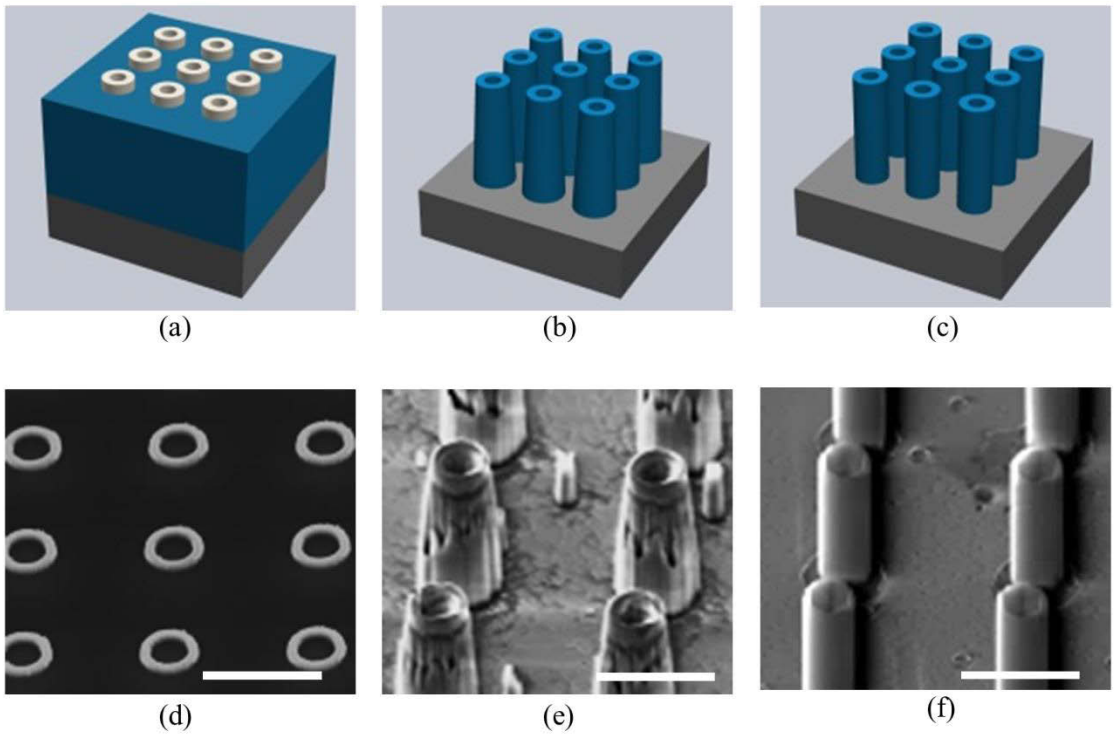

Figure 3.1 Sketches and corresponding SEM images of the fabrication process of GaN nanotube lasers. (a & d) The deposition of the etch mask composed of nickel rings on top of the GaN layer. (b & e) The ICP dry etch process. (c & f) The selective KOH-based wet etch process. Scale bars: 3μm.

The GaN nanotubes were fabricated by the top-down two-step etch process discussed in Chapter 2 (also shown in Figure 3.1). The thickness of the planar *c*-plane [0001] GaN film is 4.3μm. 350 nm-thick Ni rings were deposited on top of the GaN film as etch masks by electron-beam lithography and a metal deposition. The GaN nanotubes formed after the ICP etch are shown in Figure 3.1(e). In order to remove the dry etch damaged sidewall material and reduce the propagation loss of GaN nanotube lasers by creating smooth and straight sidewalls, the KOH-based wet etch process is subsequently applied, leading to c-axis oriented GaN nanotubes with smooth and straight sidewalls, as shown in

Figure 1(f). The outer diameters, shell thicknesses, and lengths of fabricated nanotubes are ~1.3μm, ~150nm and ~4.3μm, respectively. The circular outer cross-section and the hexagonal inner cross-section are due to the different etching mechanisms of a concave (inner cross-section) and a convex (outer cross-section) etching. In contrast to the previously reported GaN nanotubes synthesized using epitaxial casting and selective area growth [83], the tubes fabricated via this top-down method are open at both ends, facilitating potential nanofluidic applications.

3.3 Optical characterization and numerical simulation of the GaN naontube lasers

The GaN nanotube lasers are characterized experimentally using the 2-arm custom micro-photoluminescence (μ-PL) system explained in Chapter 2. In order to measure the pump-power-density-dependent emission, a variable neutral density (ND) filter is applied to vary the pump power density. The diameter of the pump laser spot is ~7 μm . A 2400 groove/mm holographic grating was chosen to achieve a high spectral resolution. For measurement of the polarization of the end-facet emission, GaN nanotubes were transferred to a cleaved edge of a silicon substrate. The end-facet emission was collected by the second arm of the μ-PL system.

Figure 3.2 shows the CCD images of a single GaN nanotube lying flat on a sapphire substrate being optically pumped below and above lasing threshold. When the pump power density is below the lasing threshold, nearly uniform emission across the entire GaN nanotube is observed, which indicates spontaneous emission from the GaN nanotube. The intensity of the emission at the center of the nanotube is slightly weaker than at both ends, because the spontaneous emission is partially coupled into the guided

modes of the nanotube waveguide. The absence of interference fringes also indicates incoherent emission. However, when the pump power density is above a certain threshold level, the intensities of the emission at both ends of the nanotube become much stronger than in the middle because the modes are strongly guided. This intensity distribution also implies that a Fabry-Perot type GaN nanotube lases rather than a whispering gallery mode[84]. The observed interference fringes imply a spatially coherent emission.

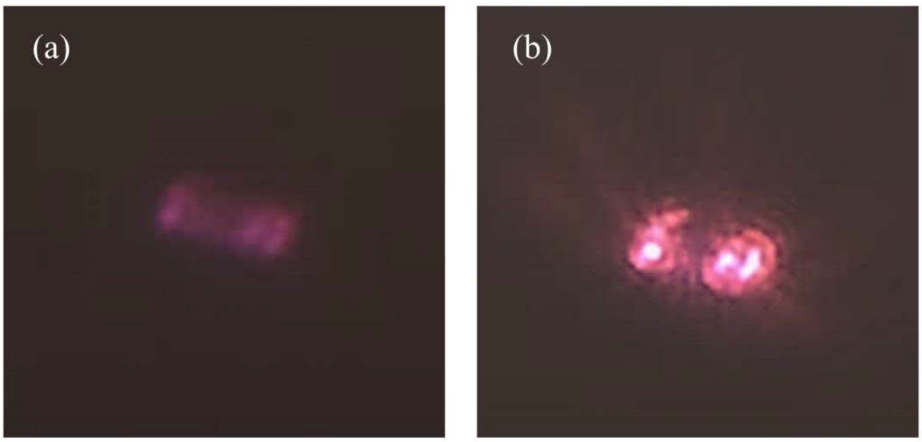

Figure 3.2 CCD images of a single GaN nanotube laser pumped (a) below and (b) above threshold. Nearly uniform emission across the entire GaN nanotube is observed, which indicates spontaneous emission from the GaN nanotube. Stronger intensities of the emission at both ends of the nanotube than in the middle is observed when the GaN nanotube is excited above threshold, indicating a highly guided Fabry-Perot mode. The interference fringes in (b) also verify the coherent emission from the GaN nanotube.

Corresponding spectra of a GaN nanotube laser lying on a SiN_x/Si substrate are plotted in Figure 3.3 (a). A broad band emission with a full width half maximum (FWHM) of ~7 nm centered at ~366nm is observed at a low pump power density (832 kW/cm^2),

corresponding to the spontaneous emission from the GaN nanotube. At a pump power density of 2754 kW/cm^2, the FWHM of the spectrum narrows dramatically to ~0.2 nm. Because the dimension of the GaN nanotube is much larger than half of the optical wavelength in the GaN, the nanotube laser shows multimode lasing behavior, leading to the relatively large lasing linewidth.

The peak intensity of the dominant lasing peak is plotted as a function of the pump power density (also known as the light-in-light-out (L-L) curves) in Figure 3.3(c). The spontaneous emission dominates at lower pump power densities; therefore the peak intensity increases linearly as the pump power density increases. However, when the pump power density excited approximately 1055 kW/cm^2, the slope of the L-L becomes much larger. This implies that stimulated emission dominates and the nanotube is excited above lasing threshold.

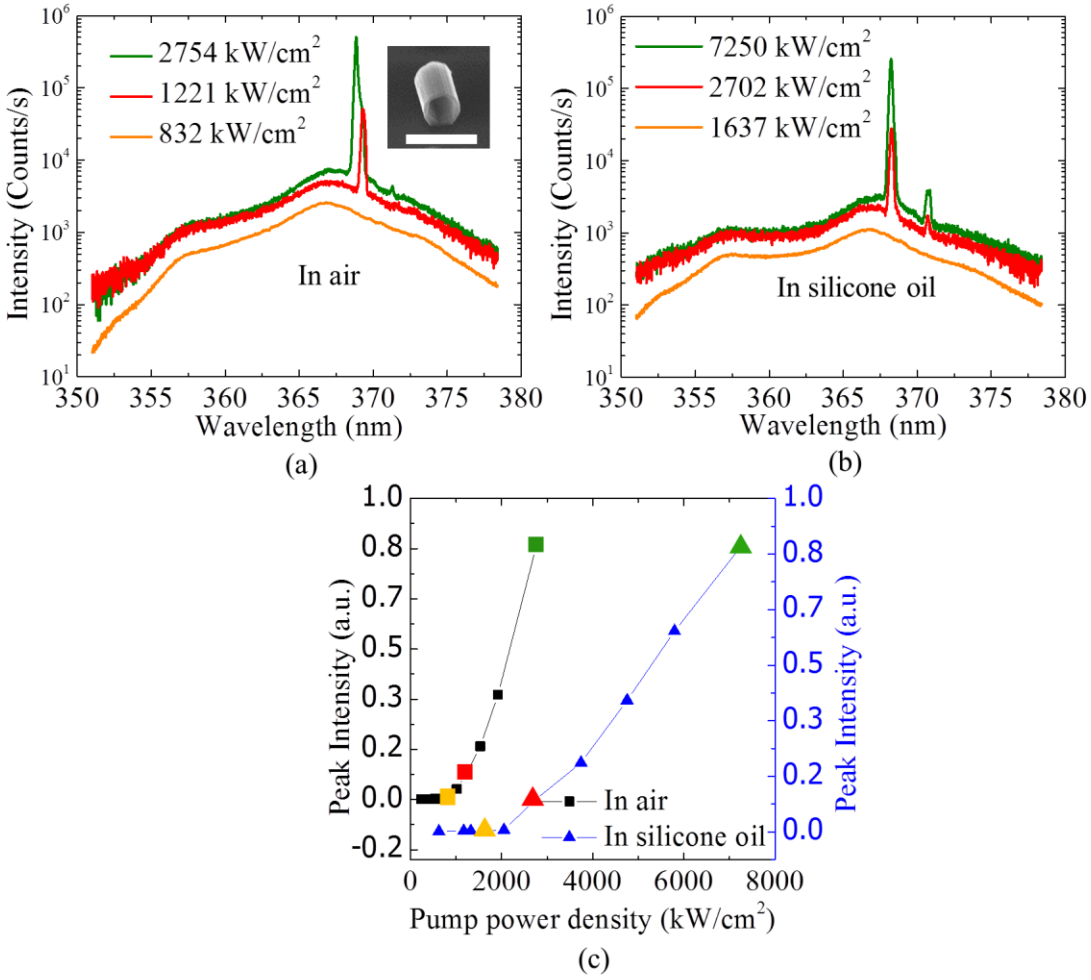

Figure 3.3 Spectra of the emission from a GaN nanotube laser (a) in air and (b) in silicone oil at different optical pump power density. (c) The peak intensity curve of the GaN nanotube laser versus pump power density (L-L curve). The colors of the boxes correspond to the colored spectra in (a) and (b). The L-L curve indicates lasing thresholds of 1055 kW/cm^2 in air and 2208kW/cm^2 in silicone oil. Inset: SEM image of the measured GaN nanotube laser. The scale bar represents 2μm.

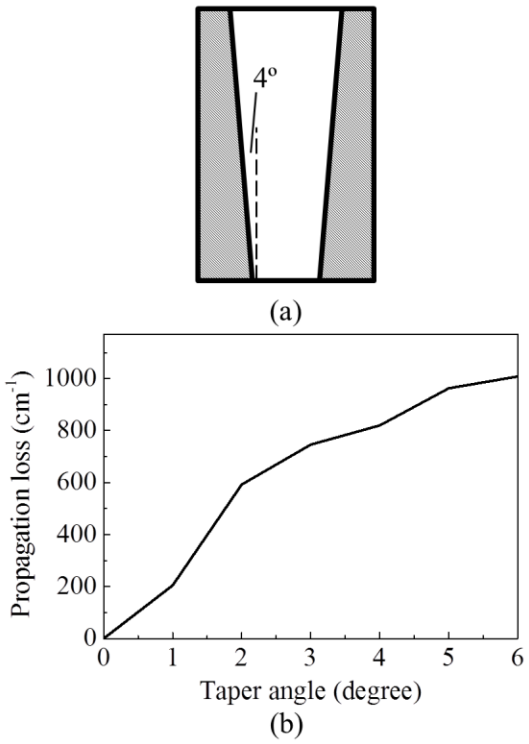

Figure 3.4 (a) Schematic diagram of the tapered inner sidewall of the GaN nanotube laser. The taper angle is measured by SEM. (b) Simulated propagation loss as a function of taper angle. A taper angle of 4 degree causes a propagation loss of 820 cm^{-1}.

In order to study the higher threshold of the GaN nanotube lasers compared to the previously reported GaN nanowire lasers, an eigenmode solver (Lumerical Inc)[75] is used to calculate the confinement factor and the propagation loss of the transverse modes. The results show that, the electro-magnetic fields of the transverse modes are well-confined in the shell region of a GaN nanotube laser. Only a small portion of the electro-magnetic fields locate in the hollow region. Therefore, the difference of the confinement factors of the transverse modes between a 1.3 μm-diameter GaN nanowire and the GaN nanotube is ~2-3%. However, we observed a 4-degree inward-tapered inner sidewalls from top to bottom of GaN nanotubes likely due to reduced dry and wet etch efficiency

inside of the tubes toward their bottoms. The simulation results show an increasing propagation loss caused by the tapered inner sidewall, due to the mismatch between the transverse modes supported by cross-sections with different dimensions. The propagation loss of the fundamental mode is plotted as a function of taper angle of the inner sidewall in Figure 3.4(b), showing that a 4 degree taper can cause an additional propagation loss of 820 cm^{-1}.

The same GaN nanotube laser was subsequently immersed in silicone oil (refractive index: ~1.5) and optically characterized for demonstrating the potential use for nanofluidic applications. The spectra and the L-L curve corresponding to the onset of lasing are observed from the GaN nanotube laser (Figure 3.3(b) and (c)) when the GaN nanotube laser is pumped above the lasing threshold (2208kW/cm^2), an approximate doubling from the threshold in air. The lasing threshold increase results from the higher ambient refractive index, which leads to a higher mirror loss and a lower confinement factor.

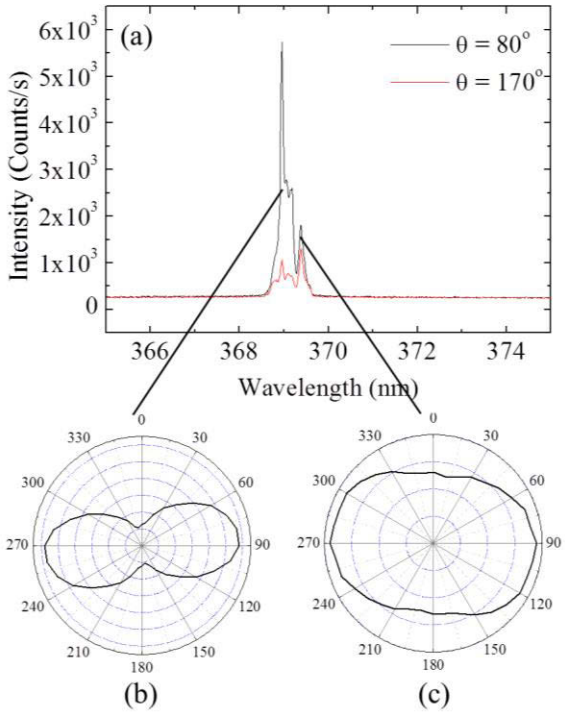

Figure 3.5 (a) Spectra of the end-facet emission from a "hanging" GaN nanotube at two polarization angles θ. (b) Peak intensity of the shorter wavelength peaks versus polarization angle. (c) Peak intensity of the longer wavelength peaks versus polarization angle. Two different cross polarization suppression ratios are observed corresponding to two lasing peak groups. The different cross polarization suppression ratios indicate that multi-transverse mode lasing occurs in the GaN nanotube laser.

In order to analyze the modal properties of multimode lasing of the nanotube lasers, the second collection arm of the μ-PL is used to measure the polarization of the end-facet emission from a "hanging" nanotube off the edge of a silicon substrate. Figure 3.5(a) shows the spectra of the GaN nanotube at two orthogonal polarization angles (80˚ and 170˚). The intensities of the lasing peaks are plotted versus polarization angle in Figure 3.5(b) and (c), respectively. Two different cross polarization suppression ratios are

observed corresponding to two lasing peak groups, 5.4:1 for the shorter wavelength group and 1.4:1 for the longer wavelength group. The different cross polarization suppression ratios indicate that multi-transverse mode lasing occurs in the GaN nanotube laser. Figure 3.6(a) shows the CCD image of end-facet emission from the GaN nanotube laser – notably, annular shape emission is observed, although the GaN nanotube laser shows multi-transverse mods lasing.

Transverse modes of the GaN nanotube laser were calculated by an eigenmode solver (Lumerical Inc). Due to its large diameter, over 100 non-degenerate transverse modes are supported by the GaN nanotube structure. A finite different time domain (FDTD) simulation (Lumerical Inc)[76] is utilized to calculate the far-field pattern resulting from the combination of all the transverse modes. The wavelength-dependent index of refraction for GaN used in the simulation was measured by spectral ellipsometry from a planar *c*-plane GaN reference epitaxial film. Two electric dipoles and two magnetic dipoles are randomly placed in the GaN nanotube to excite the optical modes supported by the GaN nanotube. In order to minimize the impact of the boundary to the simulation, a perfectly matched layer boundary condition is applied 5 wavelengths away from the GaN nanotube. The simulation result shows that far-field emission from the GaN nanotube is annular shaped, consistent with the experimental result, with a divergence angle of ~ 15° Figure 3.6(b).

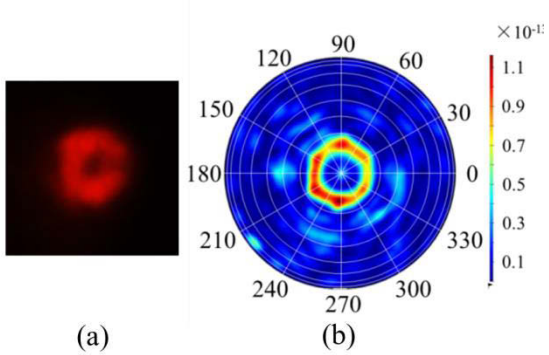

Figure 3.6 (a) CCD image of the end-facet emission of the GaN nanotube laser. (b) Simulation results of the far-field intensity of the GaN nanotube laser in spherical coordinate system.

3.4 Conclusion

In conclusion, GaN nanotubes with precisely controlled dimensions and hollow ends are fabricated by two-step top-down etch process. The nanotubes lase under optical pumping at room temperature with an observed annular end-facet emission pattern, opening the door for novel optical nano- and micro-fluidic applications. This donut-shaped emission offers the possibilities for applications benefitting from a hollow beam shape such as on-chip atom trapping[85] and stimulated emission depletion spectroscopy[86]. More generally, the results indicate that cross-sectional control of nanolasers can be used to tailor their optical properties.

Chapter 4

Intrinsic linearly polarized lasing of rectangular cross-sectioned GaN nanowire lasers

This chapter is part of a published paper entitled “Intrinsic polarization control in rectangular GaN nanowire lasers” in Nanoscale, which is published online on February 10th, 2016[87].

4.1 Introduction

In the previous paper[88], the lossy gold substrate results in higher propagation losses, and therefore, higher lasing thresholds. In addition, requiring the nanowire laser to be placed onto the gold substrate restricts nanowire lasers from more general applications that require free-standing nanowire lasers.

Linearly polarized spontaneous emission has been recently demonstrated from embedded InAs[89] or InGaAs[90] quantum dots in GaAs nanowires with elliptical cross-sections, with the polarization oriented along the elongated nanowire axis. Here, this concept is extended to demonstrate unique rectangular cross-sectioned GaN nanowires exhibiting intrinsic, linearly polarized lasing under optical pumping without requiring a lossy substrate or other environment.

4.2 Fabrication of the rectangular cross-sectioned GaN nanowire lasers

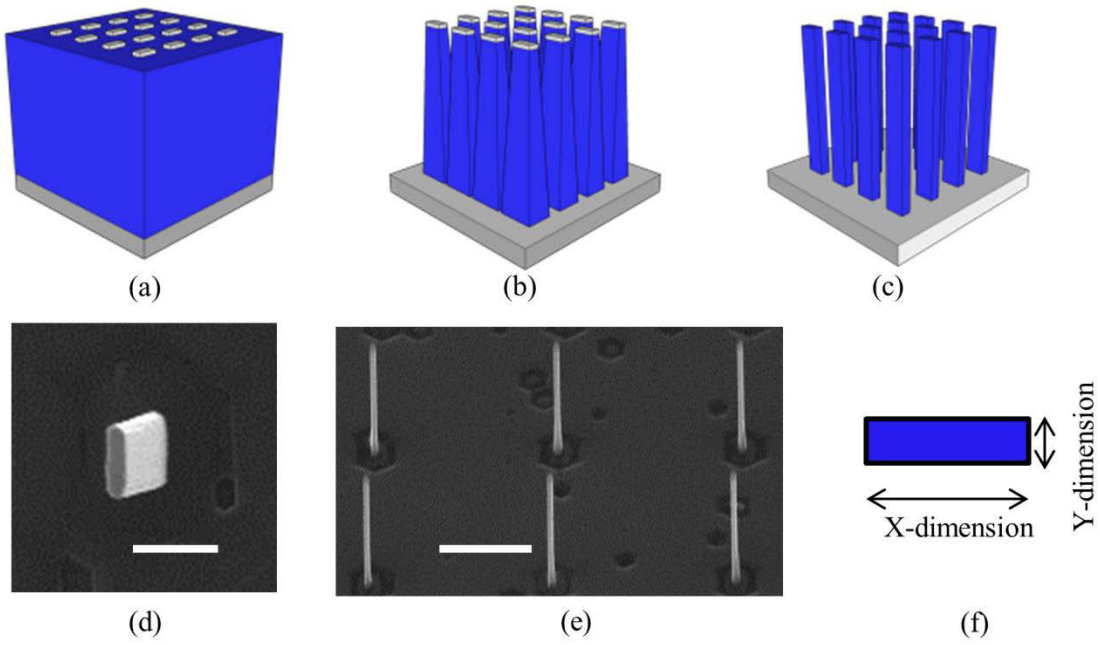

Figure 4.1 Sketches of the fabrication process and SEM images of rectangular cross-sectional GaN nanowire lasers. (a) Rectangular Ni patterns were deposited on top of a planar GaN film. (b) The rectangular patterns were transferred in the GaN film using ICP etching. (c) GaN nanowires with smooth and straight sidewalls are formed using KOH-based wet etch process. (d) SEM image of rectangular cross-sectional GaN nanowires from topview. Scale bar: 500nm. (e) SEM image of rectangular cross-sectional GaN nanowires from 45°. Scale bars: 2.5μm. (f) Diagram of the cross-section of the rectangular cross-sectional GaN nanowire laser.

The GaN rectangular nanowire lasers were fabricated by the top-down two-step dry plus wet etching process as detailed in Chapter 2. The unintentionally doped *c*-plane [0001] GaN substrate was 4 μm thick. An electron beam lithography and a lift-off were applied to define rectangular nickel dots as a dry etch mask. As seen in the SEM image (Figure 4.1(d) and 4.1(e)), the x-dimensions, y-dimensions, and the height of fabricated

rectangular cross-sectional GaN nanowire lasers (sample A) are ~450 nm, ~120 nm, and ~4 μm, respectively. In order to study how varying the y-dimension affects the polarization of the emission, another nanowire sample (sample B) was also fabricated The nanowires from Sample B have the same x-dimension and height, but larger y-dimensions (~300 nm) as the nanowires from Sample A.

4.3 Optical characterization of the rectangular cross-sectioned GaN nanowire lasers

The custom 2-arm μ-PL experimental setup as detailed in Chapter 2 was applied to characterize the optical properties of the rectangular cross-sectional GaN nanowire lasers. The diameter of the pump laser spot was 3.5 μm. The small pump spot allows individually pumping single nanowire, because the center-to-center distance of the as-fabricated GaN nanowires was designed to be 5 μm. In order to measure the polarization of the end-facet emission using the second arm, the rectangular cross-sectional GaN nanowire lasers were transferred hanging off the edge of a sapphire or a cleaved Si substrate using a cotton swab (Figure 4.3(a)).

The spectra of an as-fabricated rectangular cross-sectioned GaN nanowire laser (from Sample A) are plotted in Figure 3.2(a). At lower optical excitation level, a broad-band spectrum with a FWHM of 7.4 nm centered at 364.7 nm was observed, because the spontaneous emission with random photon state is stronger than the stimulated emission. When pump power density is above ~682 kW/cm^2, stimulated emission is dominant as sufficient round-trip gain was provided by the optical pumping to overcome the round-trip loss in the nanowire laser. The wavelength selection mechanism is then provided by the GaN nanowire as an optical cavity. Therefore, a narrow-band lasing peaks at 363 nm

with a FWHM of 0.16 nm was observed. Another broader peak was also observed at 365 nm with a FWHM of 0.39 nm possibly resulted from to amplified spontaneous emission[91]. The L-L curve is plotted in Figure 4.2(b). When the pump power density is below lasing threshold, spontaneous emission dominates. When the nanowire laser was pumped above lasing threshold, non-radiative recombination rate clamped due to the saturated carrier density, leading to much higher internal quantum efficiency. Thus, the change of the slope in the L-L curve from low pump power density to high pump power density implies the transition from spontaneous emission to lasing. The lasing threshold was estimated as ~440 kW/cm^2 by fitting the data.

The polarization of the end-facet lasing emission from a rectangular cross-sectional GaN nanowire laser (Sample A) hanging off an edge of a sapphire wafer was measured by using the second arm of the μ-PL system. The peak intensity of the lasing peak is plotted as a function of the polarization angle θ (Figure 4.3). The peak intensity reached a maxima at $\theta = 95^{\circ}$ and decreased to nearly 0 at $\theta = 5^{\circ}$, indicating an extinction ratio of approximately 14:1. The "eight" shape curve indicates that the linearly polarized emission from the GaN nanowire laser orients along the y-dimension (short dimension) of the rectangular cross-section. The polarizations of 3 other Sample A nanowires were characterized using the same method, confirming linear polarization along the y-dimension of the rectangular cross-sections, with extinction ratios of 44:1, 30:1, and 13:1, respectively. In contrast, it has been demonstrated previously that the emission from c-axis oriented cylindrical GaN nanowire lasers are elliptically polarized with random orientations of the the polarization with respect to the underlying substrate.

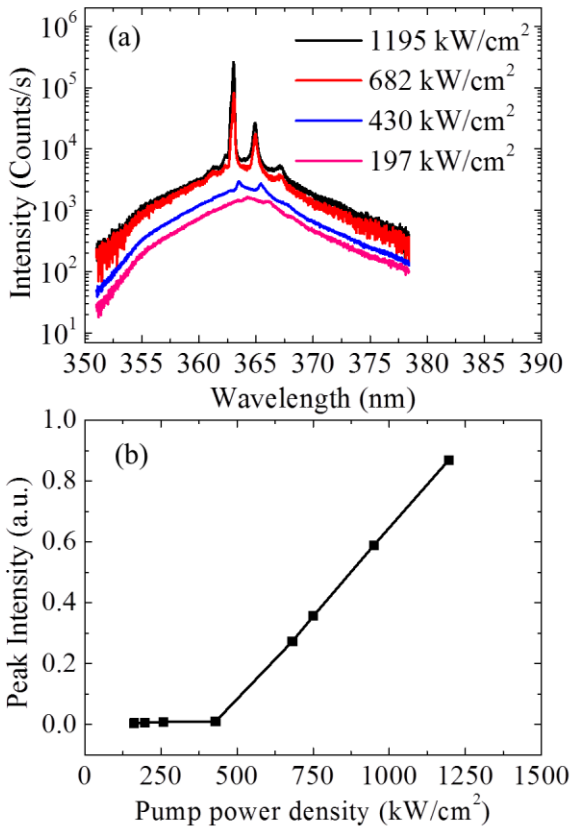

Figure 4.2 (a) Room temperature μ-PL spectra of the emission from an as-fabricated rectangular cross-sectional GaN nanowire laser at different optical pump power density. (b) The peak intensity curve of the GaN nanotube laser versus pump power density (L-L curve). The L-L curve indicates lasing thresholds of 444 kW/cm2.

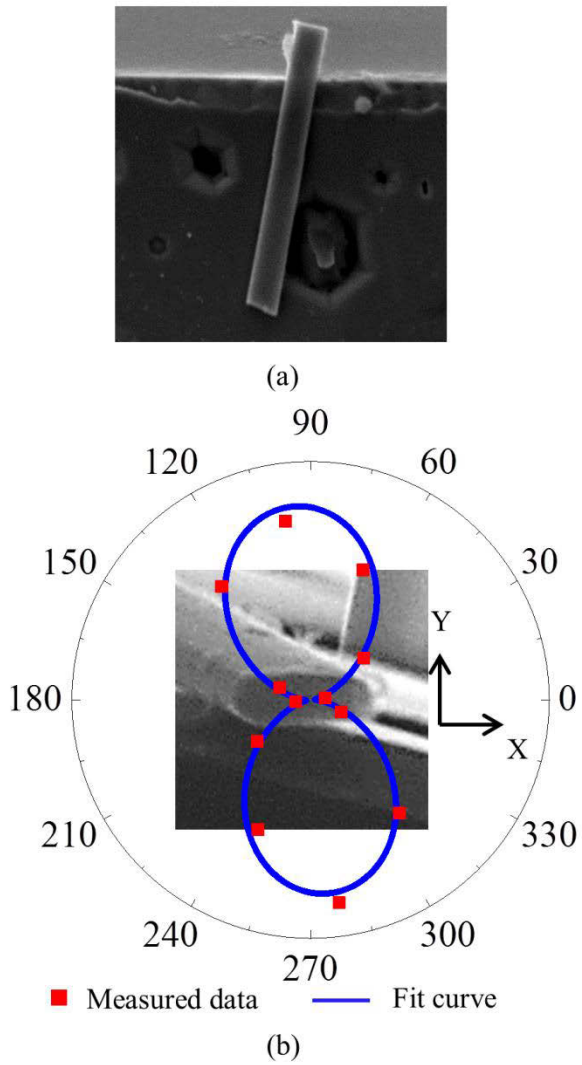

Figure 4.3 (a) SEM image of a rectangular GaN nanowire laser (Sample A) hanging off a edge of a sapphire substrate. (b) Peak intensity of the end-facet emission from the nanowire laser plotted as a function of polarization angle, demonstrating linearly polarized emission with an extinction ratio of 14:1. Inset: the SEM image of the GaN nanowire partially hanging off the edge of the substrate. The major axis of the linearly polarized emission is along the y-direction of the rectangular nanowire laser.

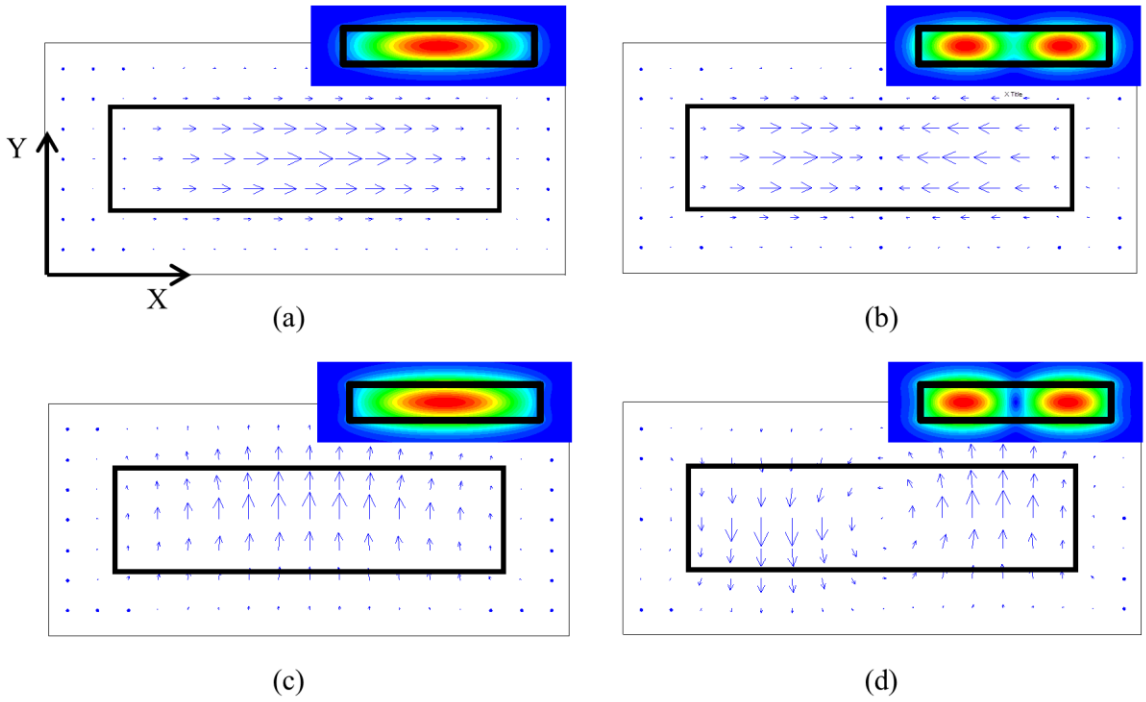

Figure 4.4 Electric fields of the first 4 transverse modes (a-d) supported by a GaN nanowire laser with rectangular cross-section. (a) and (b) correspond to the x-polarized modes. (c) and (d) correspond to the y-polarized modes. The vectors represent the directions and magnitudes of the electric fields. Insets: Intensities of electric fields for the corresponding modes. The black boxes represent the rectangular (120×450 nm) GaN nanowire cross-section. The electrical fields are linearly polarized with extinction ratios of > 32:1.

An eigenmode solver (MODE solution by Lumerical Inc.) was used to calculate the transverse modes of a rectangular cross-sectional waveguide for studying the mechanism of linear polarization. A rectangular cross-sectional waveguide was created at the center of the simulation model, according to the geometry of Sample A (an x-dimension of 450 nm and y-dimension of 120 nm). The refractive index of the GaN rectangular waveguide

was measured from a planar GaN epitaxial film by ellipsometry. The boundary was set as a perfectly matched layer to eliminate the influence from the boundary of the simulation. A 1 nm mesh size was used to provide sufficiency accuracy of the simulation. Unlike traditional cylindrical nanowires, the simulation shows that well confined transverse modes supported by the rectangular waveguide are linearly polarized (Figure 4.4).

Due to the dielectric boundary condition of the rectangular nanowire lasers, the electromagnetic fields outside of the nanowire lasers decay exponentially rather than abruptly. As a result, only a portion of the electromagnetic field of a transverse mode overlaps with the nanowire lasers and obtains the optical gain (known as the modal gain). Thus, the modal gain $\langle g \rangle$ of the transverse modes is given by:

$$\langle g \rangle = \Gamma_{xy} \Gamma_z g \tag{4.1}$$

Where g represents the material gain. Γ_{xy} and Γ_z are the transverse and longitudinal confinement factors, respectively. For a nanowire laser with uniform pumping and material quality, Γ_z and g can be assumed as constants. Therefore, the modal gain is proportional to the transverse confinement factor.

The transverse confinement factor for a rectangular cross-sectional nanowire is given by[92]:

$$\Gamma_{xy} = \frac{n}{\bar{n}} \frac{\int_{-2/2}^{w/2} \int_{-d/2}^{d/2} |U(x,y)|^2 dxdy}{\iint_{xy} |U(x,y)|^2 dxdy} \tag{4.1}$$

Where w, d, n are the x-dimension, y-dimension, and refractive index of the rectangular nanowire, respectively, and $\bar{n}$ is the effective refractive index of a transverse mode. The

second term represents the ratio of the electromagnetic field that overlaps with the nanowire to the total electromagnetic field.

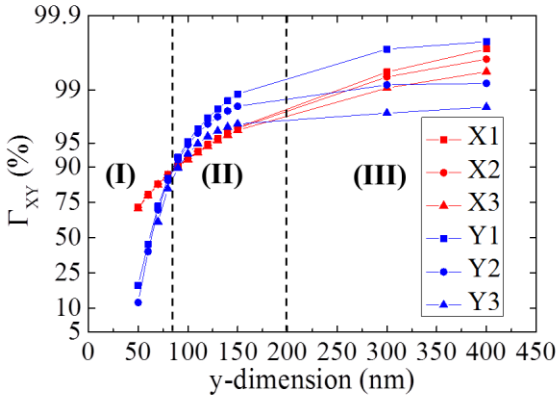

Figure 4.5 (a) Simulation results for the transverse confinement factors for the first 3 x-polarized modes (X1~X3) and the first 3 y-polarized modes (Y1~Y3) plotted in logit scale.

The simulation result of the transverse confinement factors corresponding to the lowest 3 order x-polarized and y-polarized modes is shown in Figure 4.5. Previous research has shown that the modes with a polarization along the y-direction could be cut-off by reducing the y-dimension, resulting in transverse modes with only x-polarization. In this case, the second term in equation (4.2) dominates, because the y-polarized modes spread out of the nanowire (region I in Figure 4.5). Due to the difficulty of fabrication, the y-dimension of our GaN nanowires are not small enough to cut-off the y-polarized modes. However, the simulation shows that the asymmetric cross-section results in significant difference in $\bar{n}$ for different transverse modes. Therefore, the ratio $\frac{n}{\bar{n}}$ varies largely for different transverse modes. Because the y-polarized modes have lower $\bar{n}$ than the x-polarized modes, a higher confinement factor for y-polarized modes can be achieved

(regin II in Figure 5.4). Thus, y-polarized modes would have higher optical gain than x-polarized modes. Although the mode confinement contrast is not as large as in Region I, it is still sufficient to provide the mode selection mechanism, due to the mode competition process in a laser.

The rectangular nanowires with less cross-sectional anisotropy (Sample B, x = 450 nm, y = 300 nm) were also optically pumped to verify the simulation result. Because the transverse confinement factors for x-polarized and y-polarized modes are similar, elliptically polarized lasing emissions were observed with extinction ratios of 2.8:1, 7.1:1, 3.1:1, 1.2:1 and 8.1:1 (Figure 4.6(b)). In addition, with a fixed pump condition, the intensities of lasing peaks were unstable and the dominant lasing peak shifted from one lasing peak to another, indicating a strong mode competition in the GaN nanowire laser. For the nanowire lasers with y-dimensions of <120 nm, the strong mode competition further amplified the difference in confinement factors, and therefore, the mode selection mechanism.

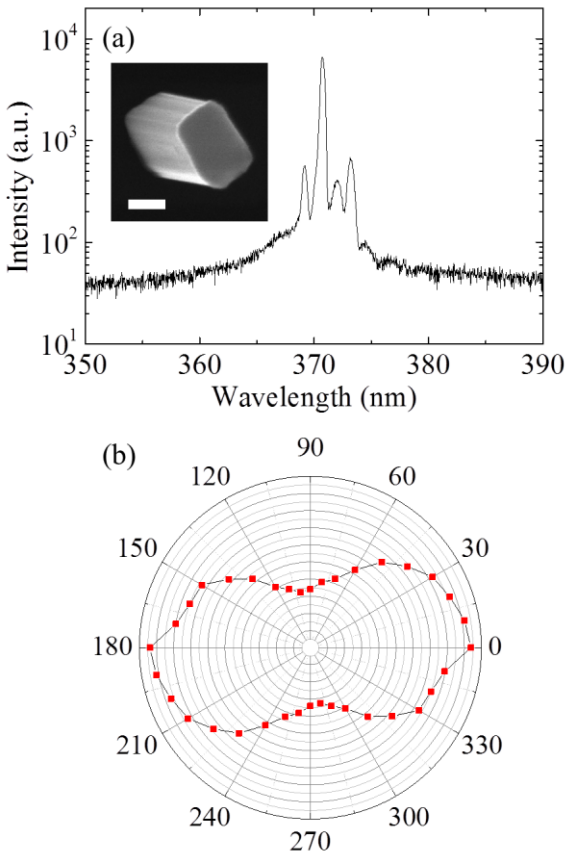

Figure 4.6 (a) Lasing spectrum of the emission from a Sample B GaN nanowire laser with a y-dimension of 300 nm (compared to y~120 nm for Sample A). Inset shows the SEM image of the Sample B GaN nanowire hanging off the cleaved edge of a silicon substrate. Scale bar: 200 nm (b) Peak intensity of the end-facet emission as a function of the polarization angle. The results show elliptically polarized lasing emission with an extinction ratio of 2.8:1.

4.4 Conclusion

In conclusion, by using the top-down two-step etching process, GaN rectangular cross-sectional nanowires with well controlled dimensions were fabricated. The asymmetric

cross-section breaks the degeneracy of confinement factors for x-polarized and y-polarized modes, resulting in higher confinement factor and higher gain for y-polarized mode. Consistently, linearly polarized lasing emission oriented along the y-direction from the rectangular cross-sectional GaN nanowire laser was observed experimentally with optical pumping. The cross-sectional control offers the ability to control the polarization from single GaN nanowire laser without additional requirement for external environment, which will greatly broaden their potential application space. For example, intrinsic, linearly polarized nanowire lasers can be transferred to photonic integrated circuit platforms to simplify the polarization-independent design of functional building blocks, such as directional couplers or ring resonators, which is not trivial and sometimes even impossible[93].

Chapter 5

Non-polar InGaN/GaN multi-quantum-wells core-shell nanowire lasers

5.1 Introduction

Although III-nitride nanowire lasers have been widely studied due to their compact size, flexibility, strain relaxation, and wide spectral coverage, most single III-nitride nanowire lasers are fabricated with homogeneous binary or ternary materials, due to the difficulty of growing high quality heterostructures on III-nitride nanowire lasers. Consequently, these III-nitride nanowire lasers only rely on the fundamental bandgap emission from the corresponding materials. More importantly, the absence of p-i-n structures results in a low injection efficiency of the electrically-driven III-nitride nanowire lasers, which is the basic requirement for practical devices.

In order to realize electrically-driven single nanowire lasers and continuous wavelength engineering, both axial and radial InGaN/GaN multi-quantum-wells (MQW) have been grown on GaN-based nanowires. Compared to the axial quantum wells, radial quantum wells offer larger volume of the active region. More importantly, radial quantum wells grown on the non-polar planes of GaN eliminate quantum-confined stark effect (QCSE), resulting in higher quantum efficiency and spectral stability. However, fabricating high quality III-nitride nanowire lasers with radial non-polar quantum wells still remains challenging. In this chapter, we have fabricated high quality non-polar InGaN/GaN

MQWs on core-shell nanowires using a combination of top-down etch technique and bottom-up regrowth technique and demonstrated lasing emission from single core-shell nanowire lasers.

5.2 Fabrication of the core-shell nanowire lasers

The fabrication of the core-shell nanowires is composed of a top-down two-step etch process and a bottom-up regrowth process (Figure 5.1). A 7 μm tall n-type GaN nanowire template was first fabricated using the top-down two-step etch process. After the etch process, the n-GaN nanowire template was returned to the MOCVD reactor to subsequently regrow 5 periods of InGaN/GaN MQWs, an AlGaN electron blocking layer, and a p-GaN/p+-GaN capping layer. Figure 5.1(f) and (g) show the SEM image and the high resolution scanning transmission electron microscopy (STEM) images of the core-shell nanowires. The nanowires appear a hexagonal cross-section with *m*-plane facets. 5 pairs of *m*-plane InGaN/GaN MQWs are observed on the STEM images. The thicknesses of the quantum wells and the quantum barriers are approximately 4.3 nm and 6.3 nm respectively. An In composition of ~8% is measured using energy-dispersive X-ray spectroscopy (EDS) mapping. The tips of the core-shell nanowires are covered by the capping layer, whereas the n-type GaN core can be exposed for electrical contact at the bottom after transferring onto a substrate.

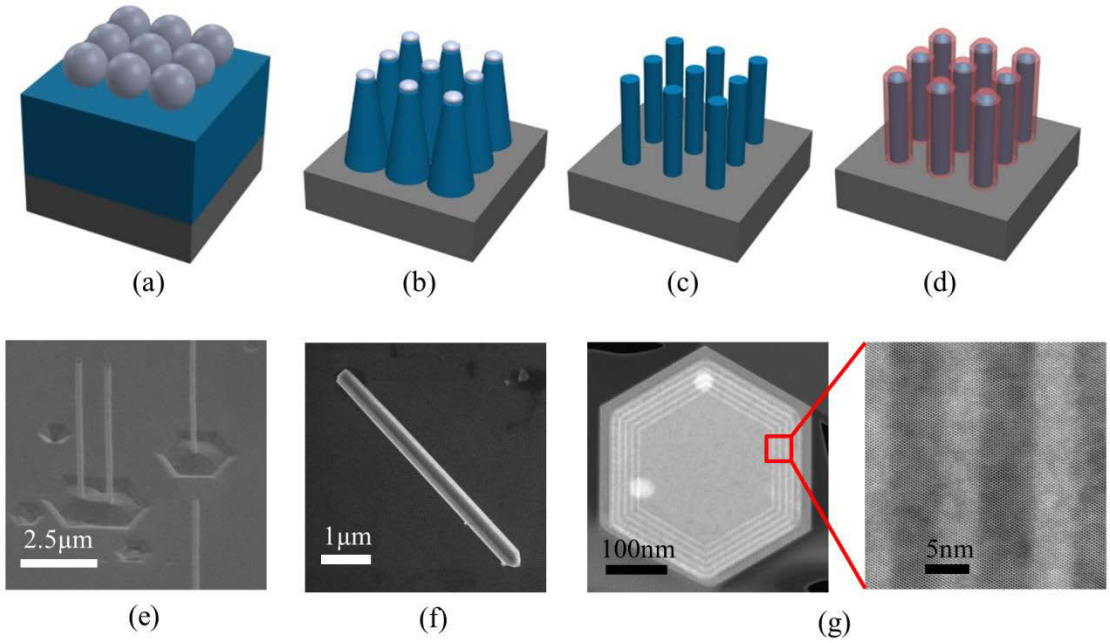

Figure 5.1 Schematic diagram of the InGaN/GaN core-shell nanowire laser fabrication process, SEM and TEM images of the InGaN/GaN core-shell nanowire laser. (a) Silica micro spheres deposited on the n-type GaN film. (b) n-type GaN nanowires with tapered and rough sidewalls after ICP dry etch. (c) Straight and smooth sidewalls of n-type GaN nanowires are created after AZ400K wet etch. (d) Shell layers (n-GaN buffer layer, InGaN/GaN MQW, AlGaN electron blocking layer, and p/p+ GaN capping layer) are grown on the n-type GaN nanowire template. (e) The SEM image of the n-type GaN nanowire core template. (f) The SEM image of a core-shell nanowire transferred onto a Si3N4/Si substrate. (g) High resolution STEM images of a core-shell nanowire.

5.3 Optical characterization and numerical simulation of the core-shell nanowires

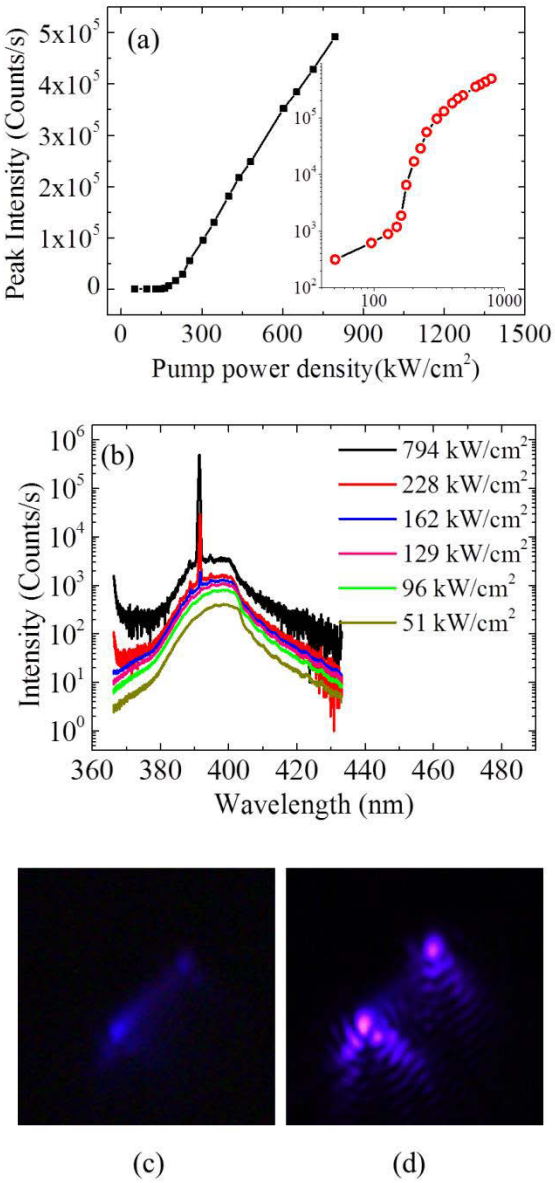

Figure 5.2 (a) The L-L curve and (b) the spectra of the emission from a core-shell nanowire laser optically pumped. A lasing threshold of 182 kW/cm^2 was calculated by fitting the peak intensities after the slope change with a linear function. Inset of (a): log-log plot of the L-L curve. No blue-shift of the peak wavelength was observed, indicating non-polar InGaN/GaN MQW. (c) and (d) CCD images of the emission from the core-shell nanowire laser pumped at 96 kW/cm^2 and 794 kW/cm^2, respectively.

The core-shell nanowires were transferred onto a SiN_x/Si substrate using a cotton swab for μ-PL characterization at room temperature. The 266 nm pump laser was focused to a spot with a diameter of ~28 μm to uniformly pump the nanowires.

The peak intensity of the emission from a core-shell nanowire laser is plotted as a function of the pump power densities (L-L curve) in Figure 2(a). When the nanowire laser is pumped below 162 kW/cm^2, the peak intensity increases linearly with a smaller slope as the pump power density increases. When the pump power density is greater than 203 kW/cm^2, the curve remains linear but with a much higher slope.

The output power P_0 of a semiconductor laser under optical pumping is given by[92]:

$$P_0 = \eta_r \beta_{sp} \eta_i \frac{A_{wire}}{V_{active}} \left(\frac{\alpha_m}{\langle \alpha_i \rangle + \alpha_m}\right) \frac{h\nu}{h\nu_p} L. \qquad (L < L_{th}) \qquad (5.1)$$

$$P_0 = \eta_i \frac{A_{wire}}{V_{active}} \left(\frac{\alpha_m}{\langle \alpha_i \rangle + \alpha_m}\right) \frac{h\nu}{h\nu_p} (L - L_{th}). \qquad (L > L_{th}) \qquad (5.2)$$

Where η_i and η_r are the injection efficiency and the radiative efficiency; β_{sp} is the spontaneous emission factor, representing the percentage of the spontaneous emission coupled into the lasing mode; α_m and $\langle \alpha_i \rangle$ are the mirror loss and the modal internal loss; $h\nu$ and $h\nu_p$ are the photon energy of the emission and pumping laser; L and L_{th} are the pump power density and threshold pump power density. A_{wire} and V_{active} are the illuminated area and the volume of the active region of a nanowire.

Based on equation (5.1) and (5.2), the output powers of a core-shell nanowire laser well below and well above threshold are linear functions of the pump power density with two different slopes. When the core-shell nanowire laser is pumped below threshold, the

spontaneous emission dominates due to the insufficient modal gain, resulting in a generally lower radiative efficiency. In addition, only a small amount of the spontaneous emission is coupled to the lasing mode. Therefore the spontaneous emission factor is much less than 1. Consequently, the slope of the L-L curve below threshold is much smaller than above threshold.

The clear change of slope in the measured L-L curve of the core-shell nanowire laser is consistent with equation (5.1) and (5.2). By fitting the peak intensities after the slope change with a linear function, a lasing threshold of ~182 kW/cm^2 is calculated.

The L-L curve is also plotted in a log-log scale shown in the inset of Figure 2(a). The L-L curve is composed of two linear regions and a super-linear region in between, which represents the transition from below threshold to above threshold. The s-shaped L-L curve verifies the lasing emission from the core-shell nanowire laser, rather than an amplified spontaneous emission.

Figure 5.2(b) shows the spectra of the emission from a core-shell nanowire laser at various pump power densities, respectively. When the nanowire was optically excited at 96 kW/cm^2, a broad-band spectrum with a FWHM of ~14 nm centered at 397 nm was observed, corresponding to a spontaneous emission spectrum. The corresponding CCD image (Figure 5.2(c)) also shows a spatially uniform emission across the nanowire laser without interference fringes, indicating an incoherent unguided emission from the nanowire. When the nanowire was pumped at 794 kW/cm^2, A narrow-band lasing peaks with a FWHM of ~0.28 was measured. Bright emissions at both ends of the nanowire laser are also shown in the corresponding CCD image (Figure 5.2(d)), implying a

strongly guided mode. The interference fringes on the CCD image indicate that the emission is coherent.

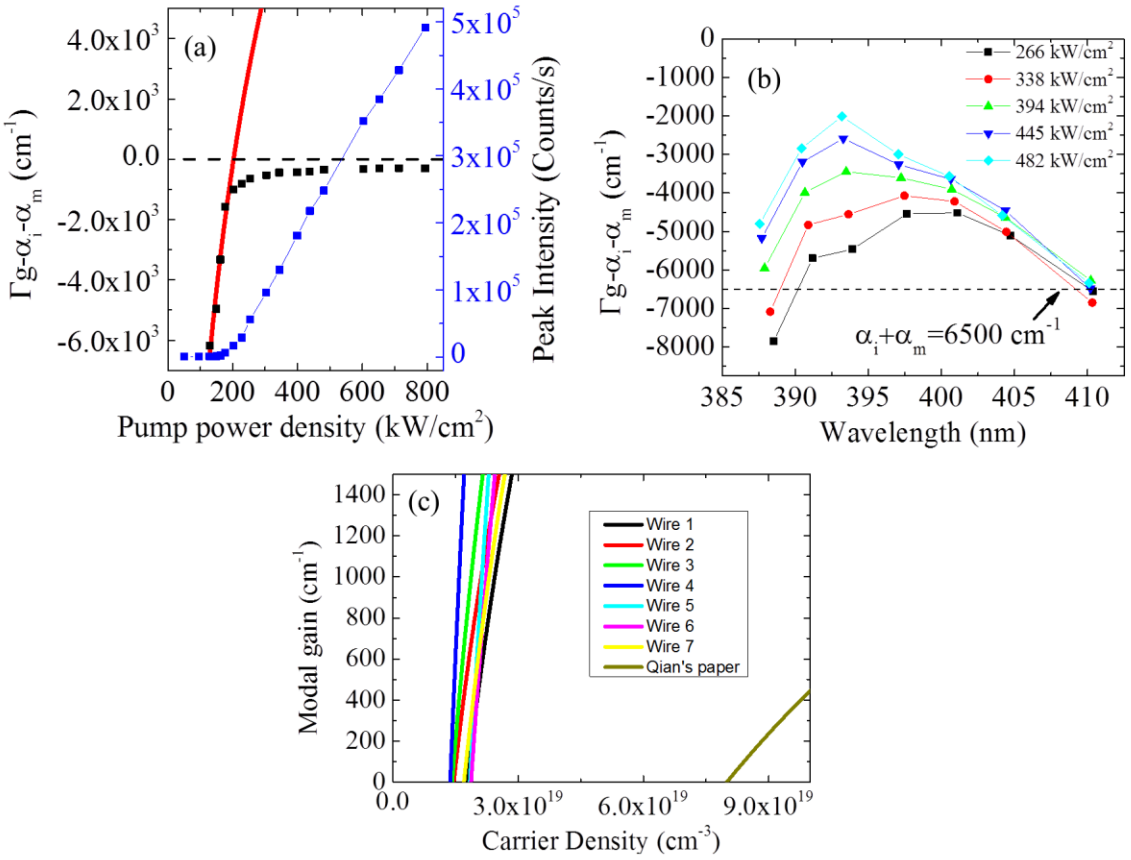

Figure 5.3 (a) Measured modal gain subtracted by modal loss (black) and output peak intensity (blue) plotted as a function of the pump power density. The modal gain is fitted according equation (3) below lasing threshold, shown as the red curve. The modal gain clamps at the lasing threshold indicated by the L-L curve, indicating the onset of lasing. (b) The gain spectra of a core-shell nanowire laser at 5 pump power densities. (c) The fitting modal gains vs. carrier density for the 7 non-polar InGaN/GaN MQW core-shell nanowire lasers. The orange curve is calculated using $\Gamma g_0 = 480\ cm^{-1}$ *and* $N_{tr} = 1.6 \times 10^{19} cm^{-3}$ *according to Fang Qian et al.'s paper.*

In order to evaluate the performance of the non-polar core-shell nanowire lasers, the lasing thresholds and modal gains of seven nanowire lasers were measured using the μ-PL setup. Despite the fact that the nanowire lasers have approximate 10 times shorter cavity lengths (~5.5 μm), significantly lower lasing thresholds of the non-polar core-shell nanowires (182 – 598 kW/cm^2) were still observed, compared to the higher lasing thresholds of the semi-polar core-shell nanowire lasers reported previously by Fang Qian et al[49]. The low lasing thresholds implies that better gain property was achieved using non-polar InGaN/GaN MQWs.

The modal gains and the modal losses of the lasing modes of the core-shell nanowire lasers are measured using a Hakki-Paoli method (Figure 5.3 (a)) to study the material property and further prove the onset of lasing. The modal gain can be written as a function of the carrier density:

$$\langle g \rangle = \Gamma g_0 \ln\left(\frac{N}{N_{tr}}\right) \tag{5.3}$$

When the nanowire is pumped below lasing threshold, spontaneous emission dominates. Therefore, the carrier density and the resulted modal gain increase as a function of the pump power density:

$$\frac{A_{wire}\eta_i}{V_{active}h\nu_p} L = AN + BN^2 + CN^3 \tag{4}$$

Where A, B and C are the Shockley-Read-Hall recombination coefficient, the radiative recombination coefficient, and the Auger recombination coefficient. L is the pump power density.

On the other hand, when the nanowire is pumped above lasing threshold, stimulated emission dominates. Due to the fast stimulated emission process, extra carriers are consumed immediately during stimulated recombination. Thus the carrier density clamps near the threshold value. As a result, the modal gain saturates quickly to the total loss after the pump power density exceeds the lasing threshold. The measured modal gain clamping shown in Figure 5.3(b) is consistent with the measured L-L curve, providing an addition proof of lasing from the nanowire lasers.

Figure 5.3(b) shows the gain spectra of a core-shell nanowire laser at five different pump power densities measured by the Hakki-Paoli method. Because of the larger separation of the quasi fermi energies, the wavelength of the peak gain blue shifted as increasing the pump power density. At shorter wavelengths, higher modal gain was observed for higher pump power densities. However, there is no significant increase of the modal gain at the longer wavelength (~410 nm), suggesting that the modal gain at ~410 nm is close to zero. Since the Hakki-Paoli method measures the difference between the modal gain and the modal loss, the modal loss, $\alpha_i + \alpha_m$, can be measured as approximately 6500 cm^{-1}.

Using the measured modal loss, the parameters Γg_0 and N_{tr} in equation (5.3) were calculated shown in Table 1 by fitting the modal gain vs. pump power density below lasing threshold using equation (5.3) and (5.4). Using the parameters, the modal gain curves of the non-polar and previously reported semi-polar core-shell nanowire lasers were plotted in Figure 3(c). The plot shows that the non-polar InGaN/GaN MQW core-shell nanowire lasers achieve higher differential gain $\frac{dg}{dN}$ and lower transparency carrier density than the semi-polar MQW core-shell nanowire laser.

Table 5.1 Parameters of the modal gain vs. carrier density formula.

Wire number	Γg_0 (cm^{-1})	N_{tr} $(10^{18}cm^{-3})$	Modal loss (cm^{-1})
1	3189	3.6	6500
2	2687	2.9	6200
3	3582	2.8	5300
4	6894	2.7	7000
5	6828	3.7	6600
6	5634	3.7	6200
7	3299	3.6	6600
Qian's paper	480	16	–

Various lasing thresholds of the non-polar core-shell nanowire lasers were also observed due to the inhomogeneous growth. Assuming the required modal gain is 6000 cm^{-1} ($g = 1200cm^{-1}$ for each quantum well), the required threshold carrier densities of the seven nanowire lasers are correlated to the measured threshold pump power density of the corresponding nanowire lasers in Figure 5.4(a). The plot shows that a lower required carrier density to achieve $g = 1200cm^{-1}$ corresponds to a lower lasing threshold. No correlation between the modal losses and the measured lasing thresholds of the core-shell nanowire lasers was observed, implying that the gain inhomogeneity is the dominant factor for the lasing threshold.

To further study the inhomogeneous modal gain property, the linewidths of the spontaneous emission spectra are fitted using a Lorentzian function and plotted in Figure

5.4(b). Nanowire lasers with wider spontaneous emission linewidths have more quantum states below the states corresponding to the lasing wavelength. Therefore, for a given carrier density, a smaller quasi fermi energy separation would be expected, because more carriers are needed to occupy the quantum states below the state of the lasing wavelength. Since a higher material gain corresponds to a larger quasi fermi energy separation, nanowires with wider spontaneous emission linewidths have higher material gain for a given carrier density. The percentage of the integrated spontaneous emission intensities in the lasing linewidths were measured, corresponding to the spontaneous emission factors β of the core-shell nanowire lasers. However, no clear correlation between the percentages and the lasing thresholds was observed, implying that β is not a dominant factor for the various lasing thresholds.

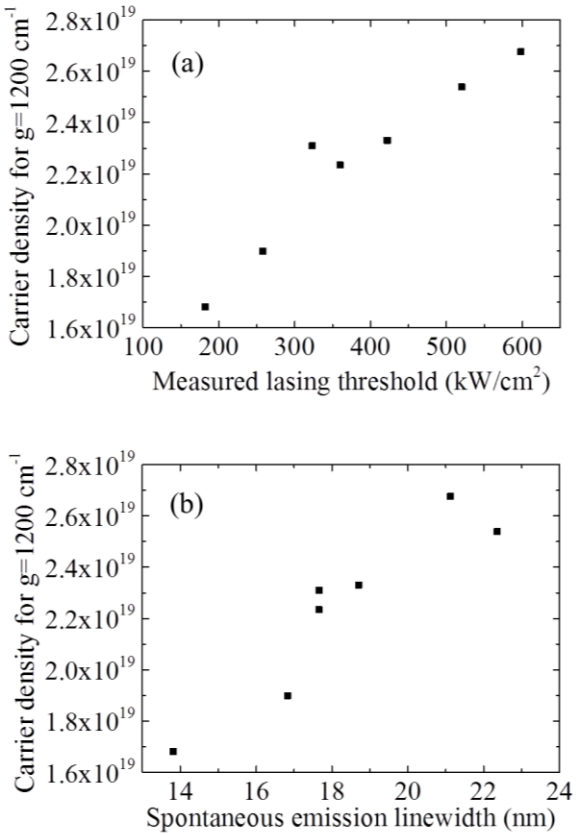

Figure 5.4 (a) Calculated required carrier densities ($g = 1200cm^{-1}$) of single quantum well for the core-shell nanowire lasers and the corresponding threshold pump power density. (b) Calculated required threshold carrier densities ($g = 1200cm^{-1}$) single quantum well for the core-shell nanowire lasers and the corresponding linewidths of the spontaneous spectra.

Table 5.2 Transverse confinement factors of transverse modes.

Mode	HE_{11}	TE_{01}	TM_{01}	HE_{21}	EH_{11}	HE_{31}
$\boldsymbol{\Gamma_{xy}}$	0.106	0.193	0.180	0.186	0.207	0.237

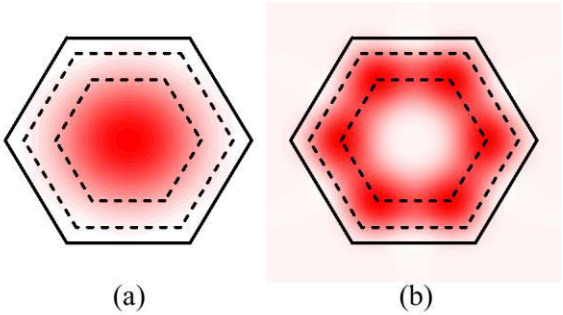

Figure 5.5 Mode profiles of (a) HE_{11} mode and (b) HE_{31} mode. The solid lines represent the boundary of the nanowire. The dashed lines represent the boundary of the active region. Due to the annular geometry of the active region, annular shaped transverse modes have higher transverse confinement factors than the solid transverse modes.

Another factor that could affect the modal gain is the transverse confinement factors of transverse modes. In order to study the transverse confinement factor, an eigenmode solver (Lumerical MODE solution) was utilized to calculate the transverse modes and the corresponding confinement factors. Owing to the annular shaped active region, transverse modes with nodes at the center would obtain higher transverse confinement factors. For example, Figure 5 shows that the mode profile of the HE_{31} mode overlaps the active region better than the HE_{11} mode does. Therefore, there is a significant variation of the transverse confinement factors (Table 2), which could play a major role in the modal gain. However, since the electric field parallel to the quantum wells obtains much higher gain than the one perpendicular to the quantum wells, the electric field profile should also be considered, which complexes the analysis of the transverse confinement factors. In addition, due to the difficulty of identifying the actual lasing mode, the transverse confinement factors were not correlated to the measured lasing thresholds in this work.

5.4 Conclusion

In conclusion, non-polar InGaN/GaN MQW core-shell nanowires were fabricated using a top-down two-step etch process and a bottom-up regrowth process. Lasing from single core-shell nanowire laser was demonstrated under optical pumping at room temperature. Due to the inhomogeneous regrowth process, non-uniform modal gains and spontaneous emission linewidths were observed using the Hakki-Paoli method and μ-PL. The inhomogeneous regrowth results in the variation of lasing thresholds for the nanowire lasers. Various transverse confinement factors for the transverse modes were also calculated, considered as another factor that affects the lasing threshold. In addition, the high g_0 and the low transparency carrier density N_{tr} result in a high modal gains and a low lasing threshold of 182 kW/cm^2. The low threshold single non-polar InGaN/GaN MQWs nanowire laser provides the possibility of electrically injected lasing from single nanowire laser. The Hakki-Paoli method also offers an efficient tool to analyze the performance of nanowire lasers.

Chapter 6

Study towards electrically injected InGaN/GaN core-shell nanowire lasers

6.1 Introduction

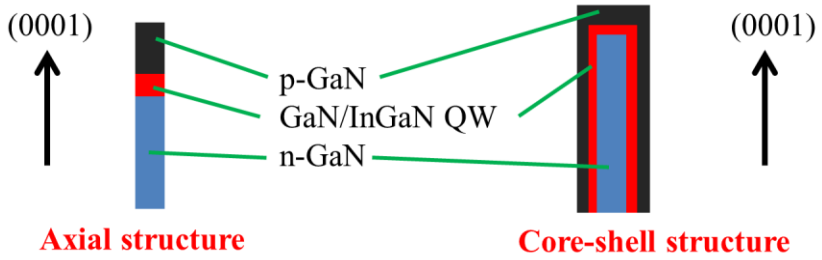

Figure 6.1 The sketch of an axial nanowire and a core-shell nanowire

Ever since optically pumped semiconductor nanowire lasers have been demonstrated, the inevitable goal has been realizing single nanowire electrically injected laser. In 2003, Duan et al. realized an electrically driven single CdS nanowire laser[94]. Although the CdS nanowire did not have a p-i-n structure and relied on a p+ Si substrate for the hole injection, it demonstrated the possibility of electrically injected monolithic single nanowire lasers. However, up to now, monolithic, electrically driven single III-nitride nanowire lasers have not been reported, due to various challenges including design, synthesis, and contact formation. First of all, because of the large work function of p-type GaN, making low resistance ohmic contact to p-GaN has been challenging. Secondly, the nanoscale contact area limits carrier injection. Lastly, because of the compact size of III-

nitride nanowires, the transverse modes can expand into the lossy contact metal, resulting in significantly high propagation loss.

III-nitride nanowires comprising a p-i-n heterostructure have two general configurations: the axial structure, and the core-shell, or radial, structure (Figure 6.1). For an axial nanowire, the quantum-wells are grown along the orientation of the nanowire. Thus, owing to the mature planar growth techniques, the axial nanowire architecture simplifies the top-down fabrication process and provides an easy way to characterize the material quality and characteristics through the corresponding planar reference sample. The exposed p-region and the n-region on opposite ends also simplify the fabrication of electrical contacts. However, due to the small volume of the active region (the InGaN quantum disks), a low longitudinal confinement factor and a high lasing threshold would be expected for an axial nanowire laser. On the other hand, a core-shell nanowire is composed of quantum-wells grown perpendicular to the axis of the nanowire, surrounding the n-type core layer over the entire length of the nanowire. For this configuration, the volume of the active region is much larger. Therefore, a high longitudinal confinement factor and a relatively low lasing threshold might be achieved. In addition, non-polar quantum-wells can be grown on the sidewalls of *c*-oriented core-shell nanowires, eliminating the QCSE. However, the shell regrowth process for the quantum-wells and the p-type capping layer on the n-type etched GaN nanowires requires optimization, which is complicated by difficulties in characterizing the nanowire properties. It is also more difficult to contact the enclosed n-type core. In this chapter, core-shell structures are chosen because the volume of the active region is considered as a more critical obstacle to realize electrically injected lasing.

6.2 Fabrication of the electrical contacts

The electrical contacts are patterned by e-beam lithography. A SiO_2/Si (SiO_2 thickness: 500 nm – 1 μm) platform designed for electrical injection was first patterned by photolithography. Limited by the resolution of the photolithography, the minimum widths of patterns on the platform were designed to be a few microns. Ti/Pt (10 nm/ 100 nm) was subsequently deposited on the SiO_2/Si substrate by e-beam deposition to form the contact leads and contact pads for electrical probing or the wire bonding. The non-polar InGaN/GaN multi-quantum-wells core-shell nanowires (discussed in Chapter 5) were then dry transferred onto the platform. Subsequently, the nanowires are mapped using an optical microscope or an SEM. According to the map, CAD files for the n-contact, the p-contact and the current spreading layer were generated by a Matlab code. Finally, the patterns were written using e-beam lithography as detailed in Chapter 2.

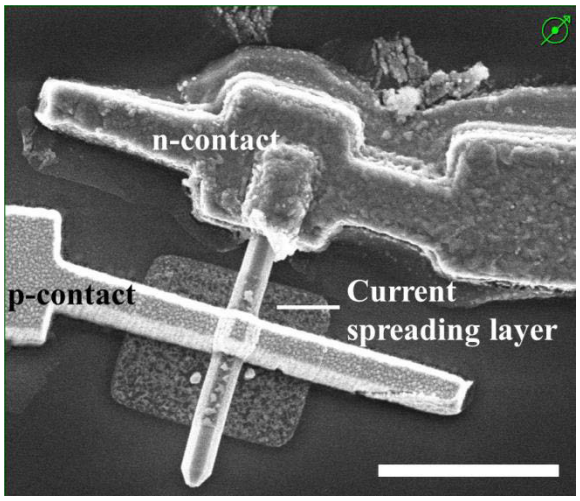

Figure 6.2 The SEM image of the contacts on a core-shell nanowire.

6.2.1 n-contact

Before the deposition of the n-contact, the sample is dipped into a 2% HF for 20 seconds to remove any native surface oxide on the nanowires. Next, a ~ 2 μm wide and ~700 nm thick Ti lead was deposited by e-beam deposition on the open end of the core-shell nanowires (Figure 6.2). The Ti layer contacts the n-type core through the open end-facet of the core-shell nanowire. Albeit the p-type shell is also contacted by the Ti, little current would be injected into the p-type shell because of the following reasons. First, the p-type GaN shell is much more resistive than the n-type core. Second, the Ti metal forms a Schottky barrier to the p-GaN due to the small work function of Ti, blocking the current flow to the p-GaN shell. After the Ti deposition, the Ti contact was annealed at 850ºC for 30 seconds in argon ambient by rapid thermal annealing (RTA). The Ti reacts with n-type GaN, forming TiN and creating nitrogen vacancies[95], [96]. The nitrogen vacancies are known as donors that create an n+ GaN layer and a tunneling junction at the GaN/Ti interface.

6.2.2 Current spreading layer and p-contact

Because of the short hole diffusion length in the p-GaN shell, a current spreading layer is needed for injecting holes uniformly. The current spreading layer is essentially an ohmic contact to the p-GaN shell with a high optical transmission at the 400 nm wavelength region[97]. The current spreading layer is deposited using the same procedure as the n-contact. 5 nm Ni/ 5nm Au was deposited and annealed in air at 550ºC for 30 seconds (Figure 6.2). After the RTA, the Ni layer is oxidized, forming NiO and Ni-Ga-O phases. At the meantime, Au diffuses into the Ni layer and contacts the p-GaN. Therefore, Au, NiO, and amorphous Ni-Ga-O phases are formed at the interface of p-GaN and the metal

contact. Although mechanism of Ni/Au ohmic contact to p-GaN is unclear, it is attributed to the low barrier height of the Au/ p-NiO/ p-GaN junction[98], [99].

Since the current spreading layer is an ohmic contact to the p-GaN, a Au lead was simply deposited on top of the current spreading layer as the p-contact (Figure 6.2).

6.3 Characterization of the contacts

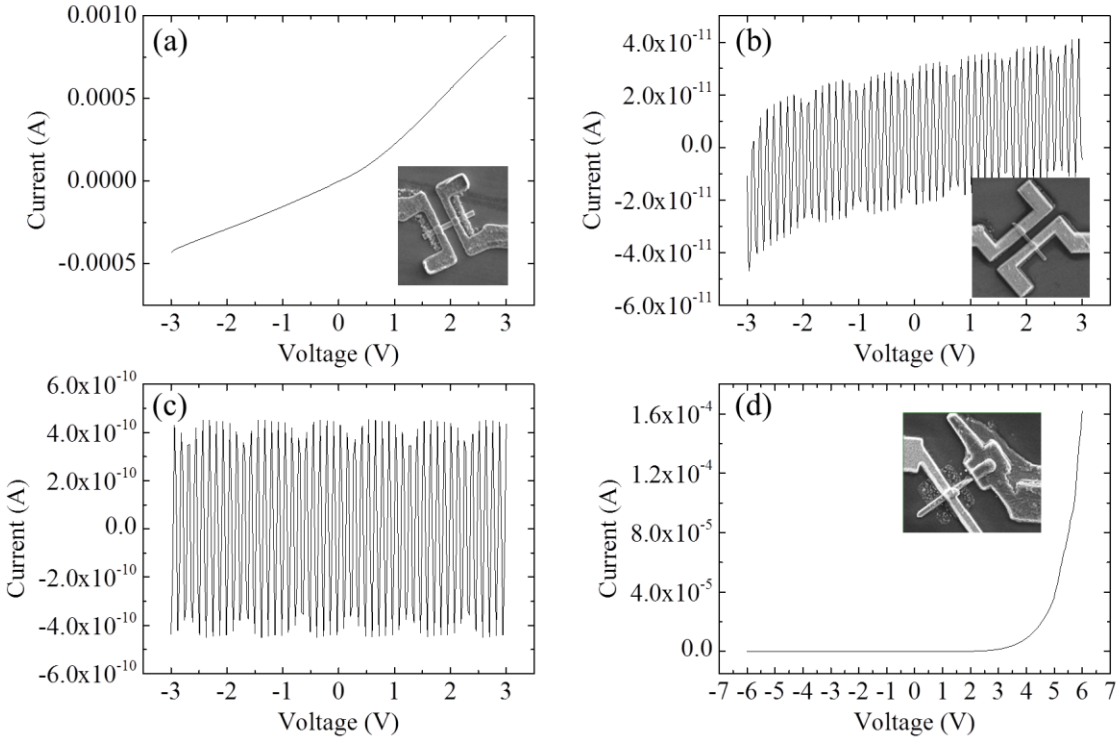

Figure 6.3 I-V curves of (a) Ti-contact on an n-GaN nanowire, (b) Ti-contact on a p-GaN nanowire, (c) Ni/Au-contact on the p-GaN shell of a core-shell nanowire, and (d) Ti-contact (right-hand side) and Ni/Au-contact (left-hand side) on a core-shell nanowire. The nanowire was damaged by the joule heating during the electroluminescence measurement.

Figure 6.3 (a) shows the I-V curve of a Ti-contact on an n-GaN nanowire. A current of ~0.43 – 0.87 mA was measured at a voltage drop of 3 V across the nanowire, corresponding to an overall resistance of ~ 3.4 – 7 kΩ. However, only 10 pA current was measured on a solid p-GaN nanowire with the Ti-contact, indicating a sufficient isolation between the Ti-contact and p-GaN shell layer (Figure 6.3(b)).

Figure 6.3(c) shows the I-V curve of the Ni/Au-contacts on the p-GaN shell of a core-shell nanowire. The extremely small current implies an ultra-high contact resistance, which limits the performance of the electrically driven core-shell nanowire LEDs or lasers. The I-V curve of a core-shell nanowire with a p-contact, a current spreading layer, and an n-contact is plotted in Figure 6.3(d). The rectifying of the I-V curve indicates the diode behavior. However, since the holes can hardly be injected into the nanowire (Figure 6.3(c)), the electrons and holes recombine at the p-contact rather than in the quantum-wells, resulting in a low injection efficiency.

6.4 Electrically driven single core-shell nanowire light emitting diodes

The CW and pulsed electroluminescence (EL) spectra was measured using the same μ-PL setup (Figure 6.4). Because the injected current is composed mainly of the electron current, only the contact area of the Ti-contact to the n-GaN core end-facet is considered as the injection area. Assuming a 300 nm diameter n-GaN core, the injection area can be calculated as $\pi \times (150\,nm)^2 = 7 \times 10^{-10} cm^2$. Therefore, the current densities range approximately from 1.4 kA/cm^2 (current = 1 μA) to 2.9 MA/cm^2 (current = 2mA). No significant blue-shift was observed up to a applied voltage of 6 V, implying the multi-quantum-wells were grown on the non-polar planes. However, only weak EL emission

was observed due to the inefficient hole-injection. Electrically injected lasing was also not observed before destruction of the devices via joule heating.

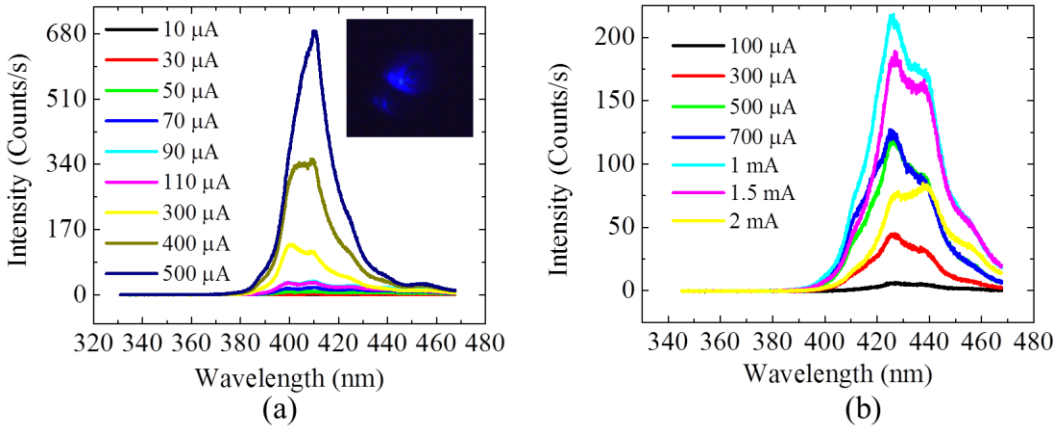

Figure 6.4 The EL spectra at various currents for (a) CW operation and (b) pulse operation (Pulse width: 300 μs, Duty cycle: 0.5%). Inset: The CCD image of the LED emission from another nanowire pumped with the same CW operation condition.

6.5 Conclusion

To summarize, an "ohmic-like" contact to n-GaN has been demonstrated using Ti annealed in argon at 850ºC for 30 seconds. The low injection efficiency from the Ti-contact to the p-GaN shell assures that the Ti covering the open end-facet of the core-shell nanowire only contacts the n-GaN core. However, due to the likely lack of ohmic contact to p-GaN shell, poor injection efficiency results in weak EL emission. Therefore, the electrically driven lasing was not realized.

Chapter 7

Conclusion and future work

Limited with the compact size and the symmetry of the cross-section of traditional nanowire lasers, control over the lasing properties for single nanowire lasers mainly relies on external environments. By using a top-down two-step etch process, III-nitride nanowires with controlled cross-sections can be fabricated. The cross-sectional control provides an inherent control over the lasing properties, such as the beam shape, the polarization, and potentially the confinement factor, without additional environment requirement, therefore, significantly broadens the application of III-nitride nanowire lasers.

Specifically, annular-shaped emission was demonstrated from GaN nanotube lasers fabricated by the top-down two-step etch process, showing potential for applications such as atom trapping or stimulated emission depletion microscopy. The different polarization states of the two lasing peak groups confirms a multi-transverse mode lasing. Consistently, annular-shaped far-field emission from multi-transverse modes of GaN nanotube lasers was also simulated by an FDTD simulation. The GaN nanotube laser was also able to function in silicone oil, suggesting potential applications in micro- and nano-fluidics.

In a separate study, by reducing the shorter y-dimension of rectangular cross-sectioned GaN nanowire lasers to ~120 nm ($\sim 0.89\frac{\lambda}{n}$), a contrast of the effective index of refraction was created. As a result, higher transverse confinement factors for the y-polarized modes

than the ones for the x-polarized modes were calculated by an eigenmode simulation, resulting in dominant y-polarized-mode lasing. Consistently, linear polarization was measured from the rectangular nanowire lasers along the shorter y-dimension. In comparison, elliptical polarization was observed from the sample B nanowire lasers (x=450 nm, y=300 nm) due to the larger y-dimension. This work shows that intrinsic polarization control is possible via cross-sectional shape control in nanowire lasers.

The top-down two-step technique also opens a route to fabricate high quality non-polar InGaN/GaN multi-quantum-well core-shell nanowire lasers. Under optical pumping at room temperature, the linewidth narrowing and the S-shaped L-L curve were measured, indicating the onset of lasing. Gain saturation was also measured by a Hakki-Paoli measurement. The Hakki-Paoli measurement shows a lower lasing threshold and a higher modal gain from the non-polar core-shell nanowire lasers than the previously reported semi-polar core-shell nanowire lasers. The non-uniform lasing thresholds from 7 non-polar core-shell nanowire lasers was attributed to the inhomogeneous regrowth process, based on the Hakki-Paoli measurement.

Although optically pumped non-polar InGaN/GaN multi-quantum-well core-shell nanowire lasers were demonstrated, electrically-driven lasing from the core-shell nanowire lasers was not achieved, because of the lack of the ohmic contact to the p-GaN shell. Instead, weak spontaneous emission was observed by the electroluminescence measurement.

The top-down two-step etch process provides a powerful tool for a wide range of research areas in the future. In the near future, the inevitable bottleneck of III-nitride nanowire

laser will still be electrical injection. In order to of achieve electrically-driven lasing, a good ohmic contact to a p-GaN nanowire would be the first, although not only, problem to solve. Besides a well-controlled p-doping level in a p-GaN nanowire, the surface fermi-energy pinning of p-GaN nanowires would be of great interest. Thanks to the well-controlled cross-section of the III-nitride nanowires by top-down two-step etch process, the relationship between the surface fermi-energy and the diameters of the p-GaN nanowires could be studied, which could potentially open a route to studying the contact mechanism in nanoscale devices.

Because of the small spacing between metal contacts and transverse modes of III-nitride nanowire lasers, significant propagation loss would be induced by metal contacts. Nanowire lasers with larger diameters could potentially lower the overlap between transverse modes and metal contacts. However, larger diameters also give rise to issues such as poor hole injection and multi-mode lasing. Contacts could also be more difficult to fabricate with large diameter nanowires. Cross-sectional control from the top-down two-step etch process enables the experimental study of the optimization of III-nitride nanowire lasers with metal contacts.

Looking ahead, the top-down two-step etch process could also be utilized to fabricate novel III-nitride nanolasers, such as nanostripe lasers and photonic crystal ring lasers. Nanostripe laser can be grown monolithically on a sapphire substrate and be integrated directly in the nanoscale integrated photonic circuits. Photonic crystal ring lasers could overcome the inevitable surface roughness resulting from ICP dry etch and crystallographic wet etch, leading to high Q-factor, low threshold ring lasers. More

importantly, photonic crystal ring lasers provide in-plane emission, which is difficult to achieve using traditional photonic crystal lasers.

Reference

[1] H. P. Maruska and J. J. Tietjen, "The preparation and properties of vapor-deposited single-crystal-line GaN," *Appl. Phys. Lett.*, vol. 15, no. 10, pp. 327–329, 1969.

[2] I. Akasaki, "Nitride semiconductors—impact on the future world," *J. Cryst. Growth*, vol. 237–239, pp. 905–911, Apr. 2002.

[3] H. Strite, S., Morkoç, "GaN, AlN, and InN: A review," *J. Vac. Sci. Technol. B*, vol. 10, no. 4, pp. 1237–1266, 1992.

[4] A. G. Bhuiyan, A. Hashimoto, and A. Yamamoto, "Indium nitride (InN): A review on growth, characterization, and properties," *J. Appl. Phys.*, vol. 94, no. 5, pp. 2779–2808, 2003.

[5] S. Nakamura and M. R. Krames, "History of gallium-nitride-based light-emitting diodes for illumination," *Proc. IEEE*, vol. 101, no. 10, pp. 2211–2220, 2013.

[6] S. Nakamura and S. F. Chichibu, *Introduction to Nitride Semiconductor Blue Lasers and Light Emitting Diodes*, 1st ed. CRC Press, 2000.

[7] A. Bykhovski, B. Gelmont, and M. Shur, "The influence of the strain-induced electric field on the charge distribution in GaN-AlN-GaN structure," *J. Appl. Phys.*, vol. 74, no. 11, pp. 6734–6739, 1993.

[8] F. Bernardini, V. Fiorentini, and D. Vanderbilt, "Spontaneous polarization and

piezoelectric constants of III-V nitrides," *Phys. Rev. B*, vol. 56, no. 16, pp. 24–27, 1997.

[9] H. Masui, S. Nakamura, S. P. Denbaars, U. K. Mishra, and A. H. Movements, "Nonpolar and Semipolar III-Nitride Light-Emitting Diodes : Achievements and Challenges," *IEEE Trans. Electron Devices*, vol. 57, no. 1, pp. 88–100, 2010.

[10] T. Takeuchi, S. Sota, M. Katsuragawa, M. Komori, H. Takeuchi, H. Amano, and I. Akasaki, "Quantum-Confined Stark Effect due to Piezoelectric Fields in GaInN Strained Quantum Wells," *Jpn. J. Appl. Phys.*, vol. 36, pp. L382–L385, 1997.

[11] D. F. Feezell, J. S. Speck, S. P. Denbaars, and S. Nakamura, "Semipolar 2021 InGaN / GaN Light-Emitting Diodes for High-Ef fi ciency Solid-State Lighting," *J. Disp. Technol.*, vol. 9, no. 4, pp. 190–198, 2013.

[12] C. J. M. Stark, T. Detchprohm, S. C. Lee, Y. B. Jiang, S. R. J. Brueck, and C. Wetzel, "Green cubic GaInN/GaN light-emitting diode on microstructured silicon (100)," *Appl. Phys. Lett.*, vol. 103, no. 232107, pp. 1–4, 2013.

[13] T. Lei, T. D. Moustakas, R. J. Graham, Y. He, and S. J. Berkowitz, "Epitaxial growth and characterization of zinc-blende gallium nitride on (001) silicon," *J. Appl. Phys.*, vol. 71, no. 10, pp. 4933–4943, 1992.

[14] S. Li, J. Schörmann, D. J. As, and K. Lischka, "Room temperature green light emission from nonpolar cubic InGaNGaN multi-quantum-wells," *Appl. Phys. Lett.*, vol. 90, no. 071903, pp. 1–4, 2007.

[15] Y. Taniyasu, K. Suzuki, D. H. Lim, A. W. Jia, M. Shimotomai, Y. Kato, M. Kobayashi, A. Yoshikawa, and K. Takahashi, "Cubic InGaN/GaN Double-Heterostructure Light Emitting Diodes Grown on GaAs (001) Substrates by MOVPE," *Phys. status solidi*, vol. 180, no. 241, pp. 241–246, 2000.

[16] S. V. Novikov, N. Zainal, A. V. Akimov, C. R. Staddon, A. J. Kent, and C. T. Foxon, "Molecular beam epitaxy as a method for the growth of free-standing bulk zinc-blende (cubic) GaN and AlGaN crystals," *J. Vac. Sci. Technol. B*, vol. 28, no. 3, pp. C3B1–C3B6, 2010.

[17] A. D. L. Bugallo, M. Tchernycheva, G. Jacopin, L. Rigutti, F. H. Julien, S.-T. Chou, Y.-T. Lin, P.-H. Tseng, and L.-W. Tu, "Visible-blind photodetector based on p-i-n junction GaN nanowire ensembles.," *Nanotechnology*, vol. 21, no. 315201, pp. 1–5, 2010.

[18] N. G. Toledo and U. K. Mishra, "InGaN solar cell requirements for high-efficiency integrated III-nitride / non- III-nitride tandem photovoltaic devices," *J.*, vol. 111, no. 114505, pp. 1–8, 2012.

[19] J. J. Wierer Jr, Q. Li, D. D. Koleske, S. R. Lee, and G. T. Wang, "III-nitride core–shell nanowire arrayed solar cells," *Nanotechnology*, vol. 23, no. 194007, pp. 1–6, 2012.

[20] S. Vilhunen, H. Sarkka, and M. Sillanpaa, "Ultraviolet light-emitting diodes in water disinfection," *Environ. Sci. Pollut. Res.*, vol. 16, pp. 439–442, 2009.

[21] M. A. Wurtele, T. Kolbe, M. Lipsz, A. Kulberg, M. Weyers, M. Kneissl, and M.

Jekel, “Application of GaN-based ultraviolet-C light emitting diodes - UV LEDs - for water disinfection,” *Water Res.*, vol. 45, pp. 1481–1489, 2011.

[22] S. Nakamura, “Background story of the invention of efficient blue InGaN light emitting diodes (Nobel Lecture),” *Rev. Mod. Phys.*, vol. 87, pp. 1139–1151, 2015.

[23] S. Chichibu, T. Azuhata, T. Sota, and S. Nakamura, “Spontaneous emission of localized excitons in InGaN single and multiquantum well structures,” *Appl. Phys. Lett.*, vol. 69, pp. 4188–4190, 1996.

[24] J. F. and H. W., “Modeling of Optical Gain in InGaN-AlGaN and Quantum-Well Lasers,” *IEEE J. Quantum Electron.*, vol. 32, no. 5, pp. 859–864, 1996.

[25] W. Huang and F. Jain, “Enhanced optical gain in InGaN–AlGaN quantum wire and quantum dot lasers due to excitonic transitions,” *J. Appl. Phys.*, vol. 87, no. 10, pp. 7354–7359, 2000.

[26] T. Tawara, H. Gotoh, T. Akasaka, N. Kobayashi, and T. Saitoh, “Cavity polaritons in InGaN microcavities at room temperature,” *Phys. Rev. Lett.*, vol. 92, no. 25, pp. 256402–1, 2004.

[27] K. Harafuji, T. Tsuchiya, and K. Kawamura, “Molecular dynamics simulation for evaluating melting point of wurtzite-type GaN crystal,” *J. Appl. Phys.*, vol. 96, no. 5, pp. 2501–2512, 2004.

[28] C. Mion, “Investigation of the Thermal Properties of Gallium Nitride using the Three Omega Technique,” North Carolina State University, 2005.

[29] S. Nakamura, M. Senoh, S. Nagahama, N. Iwasa, T. Yamada, T. Matsushita, H. Kiyoku, and Y. Sugimoto, "InGaN-based multi-quantum-well-structure laser diodes," *Jpn. J. Appl. Phys.*, vol. 35, no. 1B, pp. L74–L76, 1996.

[30] T. Kamikawa, Y. Kawaguchi, P. O. Vaccaro, S. Ito, and H. Kawanishi, "Highly reliable 500 mW laser diodes with epitaxially grown AlON coating for high-density optical storage," *Appl. Phys. Lett.*, vol. 95, no. 3, pp. 031106–1, 2009.

[31] S. Brüninghoff, C. Eichler, S. Tautz, A. Lell, M. Sabathil, S. Lutgen, and U. Strauß, "8W single-emitter ingan laser in pulsed operation," *Phys. Status Solidi Appl. Mater. Sci.*, vol. 206, no. 6, pp. 1149–1152, 2009.

[32] J. J. Wierer, J. Y. Tsao, and D. S. Sizov, "Comparison between blue lasers and light-emitting diodes for future solid-state lighting," *Laser Photonics Rev.*, vol. 7, no. 6, pp. 963–993, 2013.

[33] M. T. Hardy, D. F. Feezell, S. P. Denbaars, and S. Nakamura, "Group III-nitride lasers: A materials perspective," *Mater. Today*, vol. 14, no. 9, pp. 408–415, 2011.

[34] S. Lutgen, A. Avramescu, T. Lermer, D. Queren, J. Müller, G. Bruederl, and U. Strauss, "True green InGaN laser diodes," *Phys. Status Solidi Appl. Mater. Sci.*, vol. 207, no. 6, pp. 1318–1322, 2010.

[35] S. Gradečak, F. Qian, Y. Li, H. Park, and C. M. Lieber, "GaN nanowire lasers with low lasing thresholds," *Appl. Phys. Lett.*, vol. 87, no. 173111, pp. 1–4, 2005.

[36] F. Glas, "Critical dimensions for the plastic relaxation of strained axial

heterostructures in free-standing nanowires," *Phys. Rev. B - Condens. Matter Mater. Phys.*, vol. 74, no. 12, pp. 2–5, 2006.

[37] Y. Cui and C. M. Lieber, "Functional Nanoscale Electronic Devices Assembled Using Silicon Nanowire Building Blocks," *Science (80-.).*, vol. 291, no. 5505, pp. 851–853, 2001.

[38] S. Li and A. Waag, "GaN based nanorods for solid state lighting," *J. Appl. Phys.*, vol. 111, no. 7, pp. 1–23, 2012.

[39] A. K. Wanekaya, W. Chen, N. V. Myung, and A. Mulchandani, "Nanowire-based electrochemical biosensors," *Electroanalysis*, vol. 18, no. 6, pp. 533–550, 2006.

[40] S. Arafin, X. Liu, and Z. Mi, "Review of recent progress of III-nitride nanowire lasers," *J. Nanophotonics*, vol. 7, no. 1, p. 074599, Sep. 2013.

[41] Y. Ma, X. Guo, X. Wu, L. Dai, and L. Tong, "Semiconductor nanowire lasers," *Adv. Opt. Photonics*, vol. 5, no. 3, pp. 216–273, 2013.

[42] D. J. Sirbuly, M. Law, P. Pauzauskie, H. Yan, A. V Maslov, K. Knutsen, C. Ning, R. J. Saykally, and P. Yang, "Optical routing and sensing with nanowire assemblies," *Proc. Natl. Acad. Sci. U. S. A.*, vol. 102, no. 22, pp. 7800–7805, 2005.

[43] A. V. Maslov and C. Z. Ning, "Modal Gain in a Semiconductor Nanowire Laser With Anisotropic Bandstructure," *IEEE J. Quantum Electron.*, vol. 40, no. 10, pp. 1389–1397, 2004.

[44] A. V Maslov and C. Z. Ning, "Reflection of guided modes in a semiconductor

nanowire laser Reflection of guided modes in a semiconductor nanowire laser," *Appl. Phys. Lett.*, vol. 83, no. 6, pp. 1237–1239, 2003.

[45] A. Hurtado, H. Xu, J. B. Wright, S. Liu, Q. Li, G. T. Wang, T. S. Luk, J. J. Figiel, K. Cross, G. Balakrishnan, L. F. Lester, and I. Brener, "Polarization switching in GaN nanowire lasers," *Appl. Phys. Lett.*, vol. 103, no. 25, p. 251107, 2013.

[46] J. C. Johnson, H.-J. Choi, K. P. Knutsen, R. D. Schaller, P. Yang, and R. J. Saykally, "Single gallium nitride nanowire lasers.," *Nat. Mater.*, vol. 1, no. 2, pp. 106–10, Oct. 2002.

[47] H.-J. Choi, J. C. Johnson, R. He, S.-K. Lee, F. Kim, P. Pauzauskie, J. Goldberger, R. J. Saykally, and P. Yang, "Self-Organized GaN Quantum Wire UV Lasers," *J. Phys. Chem. B*, vol. 107, no. 34, pp. 8721–8725, 2003.

[48] M.-S. Hu, G.-M. Hsu, K.-H. Chen, C.-J. Yu, H.-C. Hsu, L.-C. Chen, J.-S. Hwang, L.-S. Hong, and Y.-F. Chen, "Infrared lasing in InN nanobelts," *Appl. Phys. Lett.*, vol. 90, no. 12, pp. 123109–1, 2007.

[49] F. Qian, Y. Li, S. G. Cak, H. Park, Y. Dong, Y. Ding, Z. L. Wang, and C. M. Lieber, "Multi-quantum-well nanowire heterostructures for wavelength-controlled lasers," *Nat. Mater.*, vol. 7, no. 9, pp. 701–706, 2008.

[50] J. E. Northrup and J. Neugebauer, "Strong affinity of hydrogen for the GaN(000-1) surface: Implications for molecular beam epitaxy and metalorganic chemical vapor deposition," *Appl. Phys. Lett.*, vol. 85, no. 16, pp. 3429–3431, 2004.

[51] R. F. Oulton, V. J. Sorger, D. a. Genov, D. F. P. Pile, and X. Zhang, "A hybrid plasmonic waveguide for subwavelength confinement and long-range propagation," *Nat. Photonics*, vol. 2, no. 8, pp. 496–500, Jul. 2008.

[52] A. Das, J. Heo, M. Jankowski, W. Guo, L. Zhang, H. Deng, and P. Bhattacharya, "Room temperature ultralow threshold GaN nanowire polariton laser," *Phys. Rev. Lett.*, vol. 107, no. 6, pp. 1–5, 2011.

[53] P. Pauzauskie, D. Sirbuly, and P. Yang, "Semiconductor Nanowire Ring Resonator Laser," *Phys. Rev. Lett.*, vol. 96, no. 14, pp. 143903–1, Apr. 2006.

[54] J. Heo, W. Guo, and P. Bhattacharya, "Monolithic single GaN nanowire laser with photonic crystal microcavity on silicon," *Appl. Phys. Lett.*, vol. 98, no. 2, pp. 1–3, 2013.

[55] T. Kouno, K. Kishino, K. Yamano, and A. Kikuchi, "Two-dimensional light confinement in periodic InGaN/GaN nanocolumn arrays and optically pumped blue stimulated emission.," *Opt. Express*, vol. 17, no. 22, pp. 20440–20447, 2009.

[56] S. Ishizawa, K. Kishino, R. Araki, A. Kikuchi, and S. Sugimoto, "Optically pumped green (530-560 nm) stimulated emissions from InGaN/GaN multiple-quantum-well triangular-lattice nanocolumn arrays," *Appl. Phys. Express*, vol. 4, no. 5, pp. 055001–1, 2011.

[57] S.-P. Chang, K.-P. Sou, C.-H. Chen, Y.-J. Cheng, J.-K. Huang, C.-H. Lin, H.-C. Kuo, C.-Y. Chang, and W.-F. Hsieh, "Lasing action in gallium nitride quasicrystal nanorod arrays," *Opt. Express*, vol. 20, no. 11, p. 12457, 2012.

[58] K. H. Li, X. Liu, Q. Wang, S. Zhao, and Z. Mi, "Ultralow-threshold electrically injected AlGaN nanowire ultraviolet lasers on Si operating at low temperature," *Nat. Nanotechnol.*, vol. 10, no. 2, pp. 140–4, 2015.

[59] Q. Li, K. R. Westlake, M. H. Crawford, S. R. Lee, D. D. Koleske, J. J. Figiel, K. C. Cross, S. Fathololoumi, Z. Mi, and G. T. Wang, "Optical performance of top-down fabricated InGaN/GaN nanorod light emitting diode arrays.," *Opt. Express*, vol. 19, no. 25, pp. 25528–25534, Dec. 2011.

[60] Q. Li, J. B. Wright, W. W. Chow, T. S. Luk, I. Brener, L. F. Lester, and G. T. Wang, "Single-mode GaN nanowire lasers," *Opt. Express*, vol. 20, no. 16, pp. 17873–17879, Jul. 2012.

[61] Y. Xiao, C. Meng, X. Wu, and L. Tong, "Single mode lasing in coupled nanowires," *Appl. Phys. Lett.*, vol. 99, no. 2, p. 023109, 2011.

[62] Y. Xiao, C. Meng, P. Wang, Y. Ye, H. Yu, S. Wang, F. Gu, L. Dai, and L. Tong, "Single-nanowire single-mode laser.," *Nano Lett.*, vol. 11, no. 3, pp. 1122–1126, Mar. 2011.

[63] H. Xu, J. B. Wright, T. Luk, J. J. Figiel, K. Cross, L. F. Lester, G. Balakrishnan, G. T. Wang, I. Brener, and Q. Li, "Single-mode lasing of GaN nanowire-pairs," *Appl. Phys. Lett.*, vol. 101, no. 11, pp. 113106–1, 2012.

[64] J. B. Wright, S. Campione, S. Liu, J. a. Martinez, H. Xu, T. S. Luk, Q. Li, G. T. Wang, B. S. Swartzentruber, L. F. Lester, and I. Brener, "Distributed feedback gallium nitride nanowire lasers," *Appl. Phys. Lett.*, vol. 104, no. 4, pp. 041107–1,

2014.

[65] H. Xu, J. B. Wright, A. Hurtado, Q. Li, T.-S. Luk, J. J. Figiel, K. Cross, G. Balakrishnan, L. F. Lester, I. Brener, and G. T. Wang, "Gold substrate-induced single-mode lasing of GaN nanowires," *Appl. Phys. Lett.*, vol. 101, no. 22, p. 221114, 2012.

[66] A. Pan, W. Zhou, E. S. P. Leong, R. Liu, A. H. Chin, B. Zou, and C. Z. Ning, "Continuous alloy-composition spatial grading and superbroad wavelength-tunable nanowire lasers on a single chip.," *Nano Lett.*, vol. 9, no. 2, pp. 784–788, Feb. 2009.

[67] Z. Yang, D. Wang, C. Meng, Z. Wu, Y. Wang, L. Dai, X. Liu, X. Liu, and Q. Yang, "Broadly Defining Lasing Wavelengths in Single Bandgap-Graded Semiconductor Nanowires," *Nano Lett.*, vol. 14, pp. 3153–3159, 2014.

[68] X. Liu, Q. Zhang, Q. Xiong, and T. C. Sum, "Tailoring the lasing modes in semiconductor nanowire cavities using intrinsic self-absorption.," *Nano Lett.*, vol. 13, no. 3, pp. 1080–1085, Mar. 2013.

[69] X. Liu, Q. Zhang, J. N. Yip, Q. Xiong, and T. C. Sum, "Wavelength tunable single nanowire lasers based on surface plasmon polariton enhanced Burstein-Moss effect," *Nano Lett.*, vol. 13, no. 11, pp. 5336–5343, 2013.

[70] J. B. Wright, S. Liu, G. T. Wang, Q. Li, A. Benz, D. D. Koleske, P. Lu, H. Xu, L. Lester, T. S. Luk, I. Brener, and G. Subramania, "Multi-Colour Nanowire Photonic Crystal," *Sci. Rep.*, vol. 3, no. 2982, pp. 1–5, 2013.

[71] S. Liu, C. Li, J. J. Figiel, S. R. J. Brueck, I. Brener, and G. T. Wang, "Continuous and dynamic spectral tuning of single nanowire lasers with subnanometer resolution using hydrostatic pressure.," *Nanoscale*, vol. 7, no. 21, pp. 9581–9588, May 2015.

[72] S. A. Hussain and D. Bhattacharjee, "Langmuir-Blodgett Films a unique tool for molecular electronics," *Mod. Phys. Lett. B*, vol. 23, no. 27, pp. 1–15, 2009.

[73] J. Zhang, Y. Li, X. Zhang, and B. Yang, "Colloidal self-assembly meets nanofabrication: From two-dimensional colloidal crystals to nanostructure arrays," *Adv. Mater.*, vol. 22, no. 38, pp. 4249–4269, 2010.

[74] S. Reculusa and S. Ravaine, "Synthesis of colloidal crystals of controllable thickness through the Langmuir-Blodgett technique," *Chem. Mater.*, vol. 15, no. 2, pp. 598–605, 2003.

[75] "Lumerical Solutions, Inc." [Online]. Available: http://www.lumerical.com/tcad-products/mode/.

[76] "Lumerical Solutions, Inc." [Online]. Available: http://www.lumerical.com/tcad-products/fdtd/.

[77] P. Blood, G. M. Lewis, P. M. Smowton, H. Summers, J. Thomson, and J. Lutti, "Characterization of Semiconductor Laser Gain Media by the Segmented Contact Method," *IEEE J. Sel. Top. Quantum Electron.*, vol. 9, no. 5, pp. 1275–1282, 2003.

[78] B. W. Hakki and T. L. Paoli, “cw degradation at 300°K of GaAs double-heterostructure junction lasers. II. Electronic gain,” *J. Appl. Phys.*, vol. 44, no. 9, p. 4113, 1973.

[79] B. W. Hakki and T. L. Paoli, “Gain spectra in GaAs double−heterostructure injection lasers,” *J. Appl. Phys.*, vol. 46, no. 3, p. 1299, 1975.

[80] C. Li, S. Liu, A. Hurtado, J. B. Wright, H. Xu, T. S. Luk, J. J. Figiel, I. Brener, S. R. J. Brueck, and G. T. Wang, “Annular-Shaped Emission from Gallium Nitride Nanotube Lasers,” *ACS Photonics*, vol. 2, no. 8, pp. 1025–1029, 2015.

[81] J. Goldberger, R. Fan, and P. Yang, “Inorganic Nanotubes : A Novel Platform for Nanofluidics Rational Synthesis of Inorganic Nanotubes,” *Acc. Chem. Res.*, vol. 39, no. 4, pp. 239–248, 2006.

[82] H. Cao, J. O. Tegenfeldt, R. H. Austin, and S. Y. Chou, “Gradient nanostructures for interfacing microfluidics and nanofluidics,” *Appl. Phys. Lett.*, vol. 81, no. 16, pp. 3058–3060, 2002.

[83] J. Goldberger, R. He, Y. Zhang, S. Lee, H. Yan, H.-J. Choi, and P. Yang, “Single-crystal gallium nitride nanotubes.,” *Nature*, vol. 422, no. 6932, pp. 599–602, Apr. 2003.

[84] T. Kouno, K. Kishino, T. Suzuki, and M. Sakai, “Lasing Actions in GaN Tiny Hexagonal Nanoring Resonators,” *IEEE Photonics J.*, vol. 2, no. 6, pp. 1027–1033, Dec. 2010.

[85] T. Kuga, Y. Torii, N. Shiokawa, T. Hirano, Y. Shimizu, and H. Sasada, "Novel Optical Trap of Atoms with a Doughnut Beam," *Phys. Rev. Lett.*, vol. 78, no. 25, pp. 4713–4716, Jun. 1997.

[86] S. W. Hell and J. Wichmann, "Breaking the diffraction resolution limit by stimulated emission: stimulated-emission-depletion fluorescence microscopy," *Opt. Lett.*, vol. 19, no. 11, p. 780, Jun. 1994.

[87] C. Li, S. Liu, T. S. Luk, J. J. Figiel, I. Brener, S. R. J. Brueck, and G. T. Wang, "Intrinsic polarization control in rectangular GaN nanowire lasers," *Nanoscale*, vol. 8, no. 10, pp. 5682–5687, 2016.

[88] H. Xu, A. Hurtado, J. B. Wright, C. Li, S. Liu, J. Figiel, T. Luk, S. R. J. Brueck, I. Brener, G. Balakrishnan, Q. Li, and G. T. Wang, "Polarization control in GaN nanowire lasers," *Opt. Express*, vol. 22, no. 16, pp. 19198–19203, 2014.

[89] M. Munsch, J. Claudon, J. Bleuse, N. S. Malik, E. Dupuy, J.-M. Gérard, Y. Chen, N. Gregersen, and J. Mørk, "Linearly Polarized, Single-Mode Spontaneous Emission in a Photonic Nanowire," *Phys. Rev. Lett.*, vol. 108, no. 7, p. 077405, Feb. 2012.

[90] A. P. Foster, J. P. Bradley, K. Gardner, A. B. Krysa, B. Royall, M. S. Skolnick, and L. R. Wilson, "Linearly Polarized Emission from an Embedded Quantum Dot Using Nanowire Morphology Control.," *Nano Lett.*, Feb. 2015.

[91] M. a. Zimmler, J. Bao, F. Capasso, S. Müller, and C. Ronning, "Laser action in nanowires: Observation of the transition from amplified spontaneous emission to

laser oscillation," *Appl. Phys. Lett.*, vol. 93, no. 5, p. 051101, 2008.

[92] L. A. Coldren and S. W. Corzine, *Diode Lasers and Photonic Integrated Circuits*, 2nd ed. Wiley, 2012.

[93] G. T. Reed, G. Z. Mashanovich, W. R. Headley, B. Timotijevic, F. Y. Gardes, S. P. Chan, P. Waugh, N. G. Emerson, C. E. Png, M. J. Paniccia, A. Liu, D. Hak, and V. M. N. Passaro, "Issues associated with polarization independence in silicon photonics," *IEEE J. Sel. Top. Quantum Electron.*, vol. 12, no. 6, pp. 1335–1343, 2006.

[94] X. Duan, Y. Huang, R. Agarwal, and C. M. Lieber, "Single-nanowire electrically driven lasers," *Nature*, vol. 421, no. 6920, pp. 241–245, 2003.

[95] Z. Fan, S. N. Mohammad, W. Kim, Ö. Aktas, A. E. Botchkarev, and H. Morkoç, "Very low resistance multilayer Ohmic contact to n-GaN," *Appl. Phys. Lett.*, vol. 68, no. 12, pp. 1672–1674, 1996.

[96] S. Ruvimov, Z. Liliental-Weber, J. Washburn, K. J. Duxstad, E. E. Hailer, Z.-F. Fan, S. N. Mohammad, W. Kim, a. E. Botchkarev, and H. Morkoq, "Microstructure of Ti/Al and Ti/Al/Ni/Au Ohmic Contacts For n-GaN," *Appl. Phys. Lett.*, vol. 69, no. 11, pp. 1556–1558, 1996.

[97] J. K. Sheu, Y. K. Su, G. C. Chi, P. L. Koh, M. J. Jou, C. M. Chang, C. C. Liu, and W. C. Hung, "High-transparency Ni/Au ohmic contact to p-type GaN," *Appl. Phys. Lett.*, vol. 74, no. 16, p. 2340, 1999.

[98] J.-K. Ho, C.-S. Jong, C. C. Chiu, C.-N. Huang, K.-K. Shih, L.-C. Chen, F.-R. Chen, and J.-J. Kai, "Low-resistance ohmic contacts to p-type GaN achieved by the oxidation of Ni/Au films," *J. Appl. Phys.*, vol. 86, no. 8, p. 4491, 1999.

[99] L.-C. Chen, F.-R. Chen, J.-J. Kai, L. Chang, J.-K. Ho, C.-S. Jong, C. C. Chiu, C.-N. Huang, C.-Y. Chen, and K.-K. Shih, "Microstructural investigation of oxidized Ni/Au ohmic contact to p-type GaN," *J. Appl. Phys.*, vol. 86, no. 7, p. 3826, 1999.